

© 2014, Frank Tramper
ISBN 978-94-6108-820-8

contact email: framper@gmail.com

The properties of low-metallicity massive stars

ACADEMISCH PROEFSCHRIFT

ter verkrijging van de graad van doctor
aan de Universiteit van Amsterdam
op gezag van de Rector Magnificus
prof. dr. D. C. van den Boom
ten overstaan van een door het college voor promoties
ingestelde commissie,
in het openbaar te verdedigen in de Agnietenkapel
op vrijdag 28 november 2014, te 12.00 uur

door

Frank Tramper

geboren te Wageningen

Promotiecommissie

Promotores: prof. dr. A. de Koter
 prof. dr. L. Kaper
Co-promotor: dr. H. Sana

Overige leden: prof. dr. H.F. Henrichs
 prof. dr. C. Dominik
 prof. dr. R.A.M.J. Wijers
 dr. F. Martins
 prof. dr. N. Langer
 dr. J.S. Vink

Faculteit der Natuurwetenschappen, Wiskunde en Informatica

The research reported in this thesis was carried out at the Anton Pannekoek Institute
for Astronomy, University of Amsterdam, The Netherlands.

1	Introduction	1
1.1	The evolution of massive stars	2
1.2	Local Group dwarf galaxies: stepping stones towards very low metallicities	7
1.3	The final stages of evolution: the enigmatic oxygen Wolf-Rayet stars	8
1.4	From stellar light to fundamental parameters	10
2	The mass loss of low-metallicity massive stars	13
2.1	Introduction	14
2.2	Observations and data reduction	15
2.3	Modeling	18
2.4	Results and discussion	20
2.5	Conclusions and implications	23
3	The properties of low-metallicity O-type stars	25
3.1	Introduction	27
3.2	Observations and data reduction	30
3.3	Analysis and results	34
3.4	The effective temperature scale	39
3.5	Mass-loss rates versus metallicity	42
3.6	Evolutionary state	44
3.7	Summary	46
4	The nature of WO stars: DR1 in IC 1613	47
4.1	Introduction	49
4.2	Literature overview	50
4.3	Observations and data reduction	51
4.4	Quantitative spectroscopic analysis	52
4.5	Discussion	63
4.6	Conclusions	71

5	The properties of the single WO stars	73
5.1	Introduction	74
5.2	Observations and data reduction	76
5.3	Spectroscopic analysis	82
5.4	The properties of the single WOs	86
5.5	Evolutionary state: remaining lifetime and final fate	90
5.6	Summary and conclusions	97
	Bibliography	98
A	Best-fit O star models	105
B	WO star modeling	111
B.1	Flux correction WO-LMC-2	111
B.2	Best-fit models	113
B.3	Overview of used model atoms	119
B.4	Equivalent width measurements	120
B.5	Helium-burning models	120
	Publications	123
	Acronyms	125
	Summary	127
	Nederlandse Samenvatting	131
	Acknowledgements	135

CHAPTER 1

Introduction

Massive stars, with initial masses above $\sim 8M_{\odot}$, are key players in the universe. Through their intense ionizing radiation, strong stellar winds, and energetic final explosions they are powerful cosmic engines (Bresolin et al. 2008). There are indications that in the primordial, metal-free environment of the young universe the formation of massive stars was favored (e.g., Larson 1998). It were these stars that provided the interstellar medium with the first elements other than the hydrogen, helium, and the trace amounts of lithium that were formed in the Big Bang. Furthermore, they likely played an important role in the reionization of the universe (Haiman & Loeb 1997) and the formation of galaxies (e.g., Aoki et al. 2014). Massive stars enrich the interstellar medium with most of the elements with atomic numbers higher than helium when they end their lives in supernova explosions. The death of the most massive among them are thought to produce some of the most spectacular events seen in the universe: hypernovae, pair-instability supernovae, and long-duration gamma-ray bursts (e.g., Yoon & Langer 2005; Woosley & Bloom 2006; Langer 2012).

To understand these various explosion types and the distribution of compact remnants (neutron stars and black holes) that are formed, the evolution of massive stars up to their eventual death in a supernova explosion needs to be understood. Key elements that affect the evolution of massive stars are their initial mass, angular momentum, and chemical composition (in particular their metallicity, the amount of elements other than hydrogen and helium), the amount of mass they lose throughout their lives, and mass exchange with a potential companion.

How these stars are formed, how massive a star can be, how much mass they lose during the various stages of their short lives, and what their properties are just prior to their supernovae are examples of key questions regarding massive stars. This thesis aims to contribute to the answers of at least some of these questions by studying stars in various stages of their lives and in various environments. Two tightly connected themes are recurring throughout the chapters: the dependence of stellar properties on

metallicity, and the strength of the stellar winds through which they expel material as a function of these properties.

With 8-10m class telescopes and state-of-the-art spectrographs it has now become possible to obtain high-quality spectra of massive stars in and even beyond the Local Group. The first part of this thesis utilizes this to target O-type stars in low-metallicity dwarf galaxies within the Local Group. The composition of these stars is closer to that of stars found in the early cosmos. The study of the properties of these massive stars is thus a step towards understanding the very early evolution of the universe. By comparing their stellar properties with those of massive stars in the Magellanic Clouds and in the Milky Way, the impact of metallicity on the physical properties and thus the evolution can be studied. The results of the first quantitative spectroscopic analysis at intermediate spectral resolution of stars in galaxies beyond the Magellanic Clouds are presented in Chapters 2 and 3.

In the second part of the thesis, the enigmatic oxygen sequence Wolf-Rayet (WO) stars are studied. These extremely rare stars are in a very late stage of evolution, and show the products of helium burning in their spectra. Although only nine members of the class are known, the WO stars are distributed over four different galaxies, each with a different metallicity. They therefore offer a unique opportunity to simultaneously study the properties of highly evolved massive stars as well as their metallicity dependence. In Chapters 4 and 5, the most detailed spectroscopic analysis of all single WO stars that were known by January 2014 is presented.

To illustrate how these topics fit in the bigger picture, the next section gives an overview of our current understanding of the evolution of massive stars. Sections 1.2 and 1.3 give background information about the two foci of this thesis. The last section briefly describes how the analyses in this thesis have been performed; from collecting the observations to obtaining the stellar parameters.

1.1 The evolution of massive stars

The evolutionary stage of most stars is reflected by their spectral type and luminosity class, and thus their position in the Hertzsprung-Russell diagram (HRD): dwarfs usually represent main-sequence stars, and giants and supergiants have exhausted the hydrogen in their cores and are in a more advanced evolutionary stage. However, this is no longer necessarily the case in the upper regions of the HRD. The stellar winds of these luminous stars affect the observational diagnostics that determine the luminosity class. As a result, stars that have a luminosity class that is usually attributed to an evolved phase may in fact still be core-hydrogen burning. This is for instance the case for the majority of blue supergiants (BSG). Some very massive stars may even be born as supergiants or Wolf-Rayet stars (e.g., Groh et al. 2014; Martins

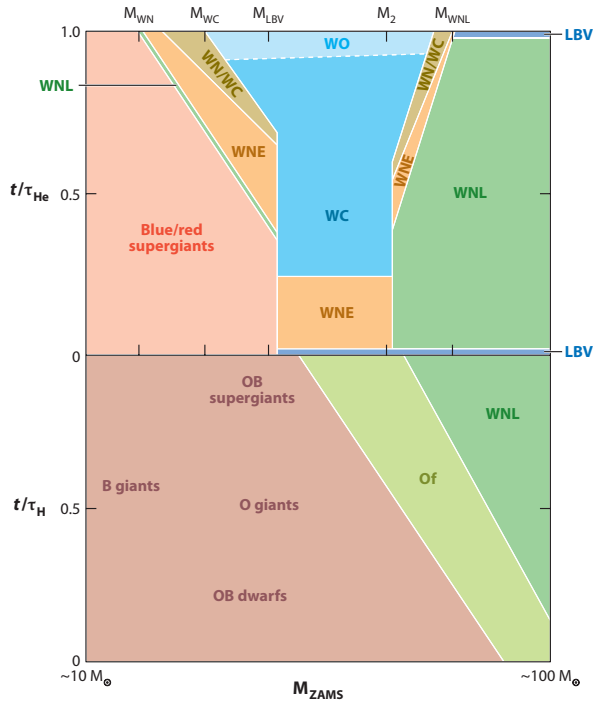


Figure 1.1: Schematic representation of the evolution of massive stars at solar metallicity. The lower panel indicates the main-sequence phase, which lasts about 90% of the lifetime of the star. The upper panel is the core-helium burning phase, which almost completely accounts for the remaining $\sim 10\%$ of the lifetime. Within each region the change in time is linear in the vertical direction. A star of a certain initial mass evolves vertically. The various evolutionary phases it may undergo are indicated in the figure, and are explained in the text. As shown in Chapter 5, we find the WO stars to be in a post core-helium burning phase, and therefore should be located above the upper panel of this plot. Figure from Langer (2012).

et al. 2008). Throughout this thesis, the term ‘main sequence’ is used explicitly for core-hydrogen burning stars, and does not imply a dwarf classification.

Posing an evolutionary scenario that incorporates the variety of massive stars that is observed is a big challenge. Our current understanding, following Langer (2012) and Sander et al. (2012), is shortly described here. Figure 1.1 gives a schematic representation of the evolutionary stages of stars with masses in the range of $10 - 100 M_{\odot}$. The location of the various evolutionary stages in the HRD are indicated in Figure 1.2. For the ‘low mass’ massive stars, with masses $< 20 M_{\odot}$, the current picture is relatively straightforward. These stars will cross the Hertzsprung gap after they exhaust the hydrogen in their core and become red supergiants (RSG). Depending on their initial properties, they will either end their life in this stage as hydrogen-rich (type II)

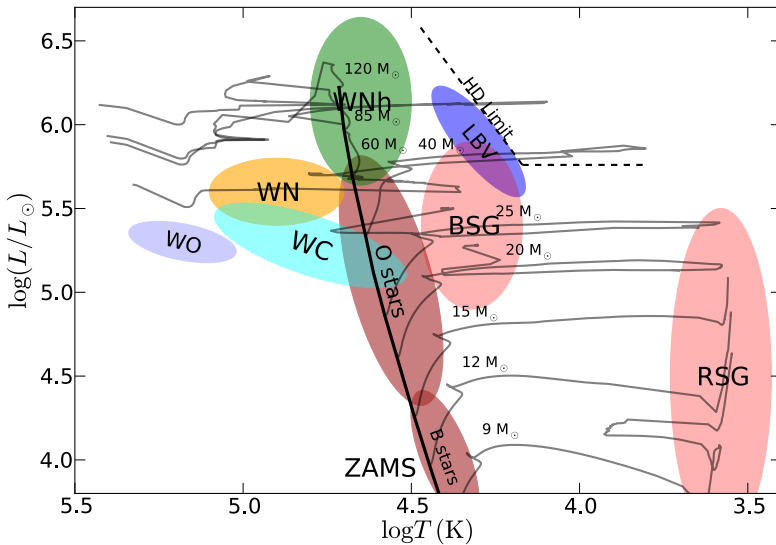


Figure 1.2: Distinct phases in massive star evolution in the Hertzsprung-Russell diagram. Overplotted are evolutionary tracks for solar metallicity from Ekström et al. (2012).

supernovae (SNe), or shed their outer layers and evolve bluewards, becoming blue supergiants before also exploding as type II supernovae.

At initial masses higher than $\sim 20 M_{\odot}$, the situation becomes more interesting. The stellar winds of stars with initial masses in the range $20 \sim 45 M_{\odot}$ will at some point after the RSG phase become so dense that the medium becomes optically thick and produces an emission-line or Wolf-Rayet (WR) spectrum. At first, such a star is a hydrogen-poor nitrogen-sequence Wolf-Rayet (WN or WNE) star. It may then evolve into a carbon-sequence Wolf-Rayet (WC) star if the wind is strong enough to expose the helium-burning core before explosion. These stars may produce hydrogen-free (type Ib/c) supernovae.

Stars with initial masses higher than $\sim 45 M_{\odot}$ cannot become red supergiants, as they are so luminous that, when they expand, they will reach the Eddington limit before reaching the cool side of the HRD. Observationally this corresponds to the area in the HRD above the Humphreys-Davidson limit (HD limit Humphreys & Davidson 1994). Instead of becoming a RSG, these stars likely go through a luminous blue variable (LBV) phase before becoming a WN or WC star, potentially even reaching the very rare WO phase. Depending on the amount of mass they lose, they explode as hydrogen-free (type Ib) or helium-poor (type Ic) supernovae.

The most massive stars ($\gtrsim 60 M_{\odot}$) have very strong winds, and start their life as an Of, Of/WNh, or WNh star. The suffix h in the notation WNh implies that hydrogen emission lines are present in the Wolf-Rayet spectrum. Such objects are thought to

be main-sequence stars (see Figure 1.2), unlike the other types of Wolf-Rayet stars that are in a post main-sequence phase (de Koter et al. 1997). These stars likely evolve so fast that they will explode in their WNH phase, thus producing a hydrogen-rich (type II) supernova. WNH stars are the only type of Wolf-Rayet stars that may have been observed to be associated with their expected supernova type, although only indirectly from flash spectroscopy very shortly after the supernova explosion (Gal-Yam et al. 2014).

Although the picture described above may give the impression that the evolution of massive stars is mostly understood, it is hampered by many uncertainties. Examples of uncertainties are the treatment of core overshooting, the mass-loss rates in the various phases of evolution, the initial spin rates of the stars and the treatment of rotational mixing, and magnetic fields. Lastly, most of the massive stars are part of a binary system, and will at some point in their evolution interact with a companion (Sana et al. 2012). This can greatly alter the evolutionary path of the stars, either because they receive new material and are rejuvenated, or because they strip their envelopes and reveal hot, enriched layers. A significant number of massive stars are even predicted to merge (de Mink et al. 2014). This complicates the comparison of the properties of SNe with predictions from single-star evolutionary tracks.

Apart from mass transfer in binary interactions, the evolution of massive stars is for a great deal determined by the amount of mass that is lost during the various stages of its life through their winds and potential mass ejections. For the hot phases, the mass is lost through line-driven winds, while at the RSG phase dust-driven winds dominate. The mechanism driving the large mass-loss episodes in LBVs is still poorly understood. As stellar winds are one of the main topics of this thesis, they are described in more detail below.

1.1.1 Stellar winds

The stars that are studied in this thesis all exhibit line-driven winds. In this mechanism, the mass loss is driven by the transfer of momentum from the radiation field to the atmospheric gas through line interactions. The theory that describes these interactions was developed in the 1970's to explain the mass loss that was observed from O and B supergiants in Orion (Morton 1966). Lucy & Solomon (1967, 1970) discuss that radiation pressure on ultraviolet resonance lines of ionized species like Si IV, C IV and N V could drive material from the stellar surface to infinity, but not in quantities large enough to significantly influence the evolution of the stars. Castor et al. (1975) showed that the radiative force on material in the envelope of O stars is actually dominated by the large number of lines from subordinate ions of elements such as iron at the flux maximum of these stars in the ultraviolet. Their predictions yielded mass-loss rates ~ 100 times higher than can be reached from the radiation



Figure 1.3: Long exposure picture of part of the Southern Hemisphere sky seen from Cerro Paranal in Chile. Clearly visible are the Milky Way disk in the center and the Magellanic Clouds on the left. The dome of Unit Telescope 1 is visible on the right. Picture courtesy of ESO/Yuri Beletsky.

pressure on resonance lines alone. Various improvements to the theory have been made in the 1980's and 1990's (e.g., Kudritzki et al. 1987), including effects such as line-blanketing and the metallicity dependence of the stellar winds.

More recently, Vink et al. (2000) provided a prescription of the mass-loss rates from O and B stars as a function of stellar parameters. These prescriptions are based on Monte-Carlo simulations to also evaluate the effect of multiple photon scatterings. As the stellar winds are mainly driven through electron transitions in ions from iron-like elements, it is a logical consequence that the strength of the winds scales with metallicity. This effect is quantified in the mass-loss prescriptions of Vink et al. (2001). Currently, the Vink et al. (2000, 2001) prescriptions are most commonly used to describe the mass-loss rate of O and B-type stars in massive star evolutionary models (e.g., Brott et al. 2011; Ekström et al. 2012).

The metallicity dependence of stellar winds has been empirically tested for O stars in the Milky Way and Magellanic Clouds (Mokiem et al. 2007), covering a metallicity range from solar down to 20% solar. The mass-loss rate (\dot{M}) of the stars in these galaxies showed a metallicity (Z) dependence of $\dot{M} \propto Z^{0.78 \pm 0.17}$, in excellent agreement with the predicted relation $\dot{M} \propto Z^{0.69 \pm 0.10}$ from Vink et al. (2001). In chapters 2 and 3 we present the first tests of radiation-driven wind theory from stars in some of the more remote, metal-poor Local Group dwarf galaxies.

1.2 Local Group dwarf galaxies: stepping stones towards very low metallicities

The mean metal content of the universe is slowly increasing over time as a result of the enrichment of the interstellar medium through the stellar winds and supernovae of massive stars. Currently, the mean metallicity in the universe is $\log(Z/Z_{\odot}) = -0.65$ at a redshift of $z = 0.1$. It decreases by 0.22 dex per unit redshift up to at least a redshift of $z \sim 5$ (Rafelski et al. 2012). At each redshift, the metal content shows a dispersion of about 0.5 dex in metallicity. This scatter is in part a result of the dependence of the metal content of a galaxy on its stellar mass (e.g., Lequeux et al. 1979; Tremonti et al. 2004), with higher mass galaxies having a higher metallicity.

This implies that the metal content of our Milky Way galaxy is by no means typical of what is found in the universe. More characteristic of the current average metallicity are the Magellanic Clouds, which have metallicities of $Z_{\text{LMC}} = 0.5 Z_{\odot}$ and $Z_{\text{SMC}} = 0.2 Z_{\odot}$. Clearly visible by the naked eye from the Southern hemisphere (Figure 1.3), both Magellanic Clouds host a sizable population of massive stars. As described above, the observed dispersion in metallicity implies that the Magellanic Clouds are representative of *massive* galaxies at earlier epochs. If massive galaxies have metallicities that are about one standard deviation above the mean, the LMC has a metallicity that is typical for a massive galaxy at a redshift of $z \sim 0.68$ or a cosmic age of 7.5 Gyr. The metallicity of the SMC corresponds to typical massive galaxies at $z = 1.59$ or 4.1 Gyr. Besides the Magellanic Clouds, the Local Group hosts several other dwarf galaxies, some of which have a metallicity lower than that of the SMC.

Because single stars can not be resolved at distances much beyond the Local Group (e.g., Hartoog et al. 2012), it is impossible to study massive stars at the high redshifts corresponding to a very low mean metallicity. However, the low-metallicity Local Group dwarf galaxies offer the opportunity to still investigate the properties of massive stars throughout cosmic history. In the LMC and SMC, the massive star population can be resolved using relatively small telescopes. Going beyond the Magellanic Clouds, 8m class telescopes combined with suitable instruments are needed to study the stars. In this thesis, we study objects in three of these galaxies: IC 1613, WLM, and NGC3109, located at distances of 10-20 times that of the SMC using the X-Shooter instrument on ESO's *Very Large Telescope* (Section 1.4.1).

These three dwarf irregular galaxies have a measured nebular oxygen abundance that is only about 5-10% of the solar abundance. The measured oxygen abundance in young stars is slightly higher, and corresponds to a metallicity of about 14% of solar. Following the reasoning given above, this is typical of a massive galaxy at a redshift of $z = 3.2$, or an age of the universe of 2 Gyr. However, there are indications that the stars in these galaxies have a sub-solar α -to-iron ratio (e.g., Garcia et al.

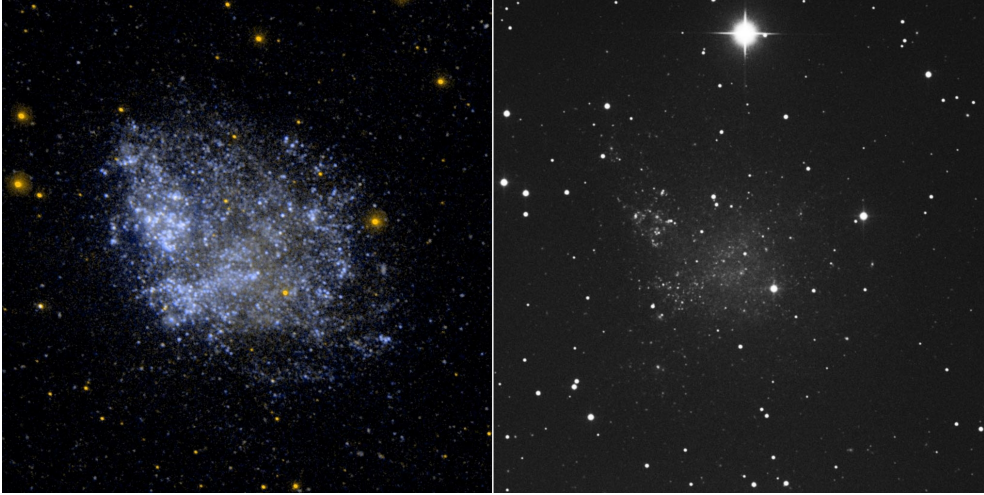


Figure 1.4: Image of the dwarf irregular galaxy IC 1613 in ultraviolet (left) and visible (right) light. The two main star formation regions can clearly be distinguished in the UV image. Image credit: NASA/JPL-Caltech/SSC.

2014), so that the iron abundance relative to oxygen could be higher. Taking this into account, these galaxies represent metallicities similar to (or still slightly below) that of the SMC.

Chapters 2 and 3 present the first detailed quantitative spectroscopic analysis of O stars in IC 1613, WLM, and NGC 3109. The first chapter focusses only on the stellar winds of the target stars, while in Chapter 3 the physical and evolutionary properties are discussed. Surprisingly, the metallicity dependence of the stellar winds that is described in the previous section seems to break down in these galaxies. Instead of wind strengths predicted for an SMC metallicity or lower, the O stars exhibit winds reminiscent of an LMC metallicity.

The closest of the three galaxies is IC 1613, which is about ten times more distant than the SMC. IC 1613 is currently vigorously forming stars (see figure 1.4), in two clearly distinguishable star forming regions. Apart from the O stars, this galaxy also hosts a very rare WO star, which is the topic of chapter 4.

1.3 The final stages of evolution: the enigmatic oxygen Wolf-Rayet stars

Of the three types of non-core hydrogen burning Wolf-Rayet stars (WN, WC and WO), those of the oxygen sequence (WO) are by far the rarest. Like all WRs, their spectra are characterized by strong, broad emission lines formed in their dense stellar

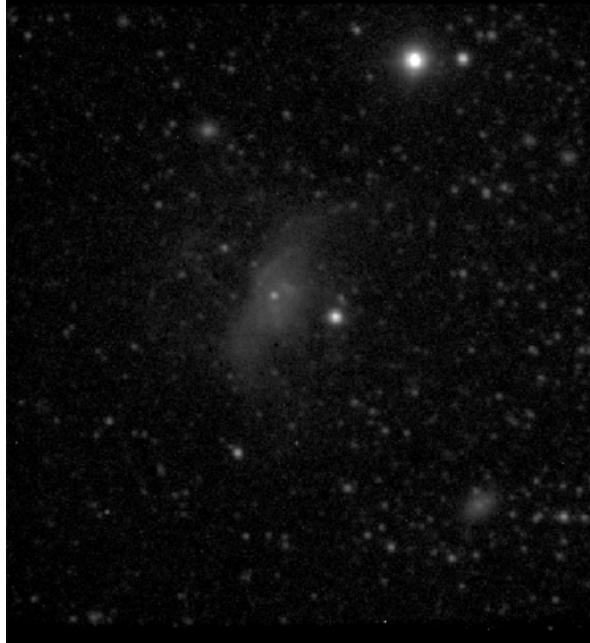


Figure 1.5: X-Shooter acquisition image of the WO star DR1 in IC 1613. DR1 is the faint star located in the asymmetric nebula, and is its ionizing source. The angular size of the image is $30 \times 30''$.

wind. What makes them unique among the WR stars is the strong emission of $O\text{ VI}$ $3811\text{-}34\text{ \AA}$, which is usually attributed to a high oxygen abundance (e.g., Barlow & Hummer 1982). An alternative explanation for this emission is a very high stellar temperature, in which case a very high oxygen abundance is not necessarily implied (Hillier & Miller 1999).

As the WO stars show the products of core-helium burning in their spectrum, they must be highly evolved stars. This makes them extremely interesting targets to improve our understanding of the final stages of the life of massive stars. They also provide direct observational constraints on the physical processes during and perhaps after core-helium burning. Finally, their properties determine the type and chemical yields of their supernova explosion at the end of their lives.

In Chapters 4 and 5 all the known single WO stars are analyzed, except for the recently discovered WO2 star in the LMC (Massey et al. 2014). In Chapter 4, the most distant WO star is analyzed: DR1 in the dwarf galaxy IC 1613 (Figure 1.5). This chapter also provides the method for the spectroscopic and atmospheric analysis of this type of stars. In Chapter 5 the full sample of WO stars is analyzed. The most exciting result is the firm determination that these stars are in a post core-helium burning state. Moreover, their remaining lifetime is estimated and found to be extremely



Figure 1.6: The X-Shooter instrument at the Cassegrain focus of UT2. Image credit: ESO.

short: they will explode in only a few thousand years.

1.4 From stellar light to fundamental parameters

All the stars in this thesis are analyzed through quantitative spectroscopy. The observations, data reduction, and analysis are described in detail in each of the chapters. This section gives a short overview of how to get from the stellar light we see to the fundamental stellar properties that we want to know. The information about these properties is encrypted in their spectra, and the first step is thus to obtain these spectra. The stellar properties can then be derived by a detailed modeling of the spectral features using stellar atmosphere codes.

1.4.1 Observations: The X-Shooter spectrograph on the Very Large Telescope

All spectroscopic data that is used in this thesis have been obtained with the X-Shooter instrument on ESO's Very Large Telescope (VLT, Figure 1.6). Located at Cerro Paranal in the Chilean Atacama desert, the observing conditions are among the best in the world. The VLT consist of four telescopes with 8.2m primary mirrors, the Unit Telescopes (UTs). The design of the UTs allows the light to be channeled into one of three separate science instruments, one at the Cassegrain focus and two at the Nasmyth foci. The UTs are supplemented by four movable 1.4m Auxiliary

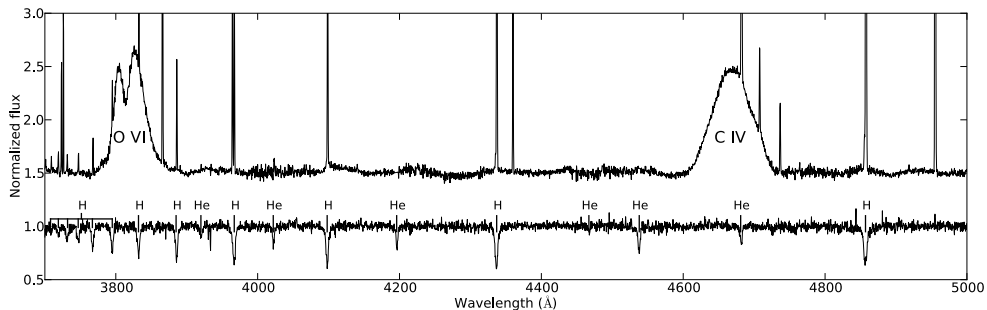


Figure 1.7: Part of the X-Shooter spectrum of two stars in IC 1613. The bottom spectrum belongs to an early O-type star and shows absorption lines of hydrogen and helium. The top spectrum belongs to the WO star DR1 and shows strong and broad emission of highly ionized oxygen and carbon. The flux of the WO star has been reduced by a factor of five. The narrow emission lines in the WO spectrum originate from the surrounding nebula (see Figure 1.5).

Telescopes (ATs) which are used for the VLT interferometer (VLTi), with or without one of UTs.

X-Shooter (Vernet et al. 2011) is a second generation VLT instrument which was installed on UT2 in 2009 and was moved to UT3 in 2013. It is mounted at the Cassegrain focus. The design of X-Shooter is unique; it separates the light into three different wavelength ranges with an efficiency of $\geq 90\%$ into three distinct spectrographs. This design, combined with the collecting power of an 8.2m telescope, allows to take the spectrum from the atmospheric cut-off at 300 nm up to the K-band (2.5 micron) in a single exposure, at intermediate spectral resolution. The combination of high throughput and intermediate resolution makes X-Shooter suitable for many applications, and it is currently one of the most popular instruments in the world.

1.4.2 Quantitative spectroscopy

Quantitative spectroscopy is the process of determining the physical properties of a star by computing synthetic spectra using models that describe the atmospheres of these stars. To model the observed spectra, two very different methods are used in this thesis. The spectrum of O stars is formed in the photosphere of the stars and is dominated by hydrogen and helium absorption lines (see Figure 1.7). These spectra are analyzed using an automated fitting method. The spectra of WO stars are formed in their optically thick stellar wind, and show strong emission from recombination lines of helium, carbon and oxygen. To model these spectra, a tailored analysis is needed. Both these methods are shortly described here.

O stars: automated fitting

The O-star spectra are modeled using the `FASTWIND` code (Puls et al. 2005). As the name suggests, this code can calculate a model of a stellar atmosphere in a relatively short amount of time (approximately 15 minutes). The code iteratively solves the transfer and statistical equilibrium equations starting from a grey atmosphere, and as such only requires the stellar parameters as input. These characteristics allow a large amount of models to be calculated, and thus facilitates a thorough exploration of the multi-dimensional parameter space. In this thesis, parameter space is explored using a genetic algorithm (GA), employing a method that was developed in Amsterdam by Mokiem et al. (2005), and to which several improvements have been made (see Chapter 3).

In short, the GA calculates several ‘generations’ of models, each generation consisting of a number of ‘individuals’. The first generation of models consists of random combinations of parameters. The goodness-of-fit is calculated for each of the models, and the parameters of the best 50 models are used as parents for the next generation, i.e. combinations of their parameters are used. This is repeated until a local minimum in the goodness-of-fit is reached (typically within 15 generations). For the remainder of the generations random mutations to the parameters are applied to fully explore parameter space and make sure the final result is the global best fit. As the goodness-of-fit is known for all the calculated models, formal error bars can be defined.

A typical fitting run for a star calculates 300 generations of 79 models, and takes about four days to compute on a cluster of 80 processors.

WO stars: detailed modeling

For the WO star modeling, the `CMFGEN` code (Hillier & Miller 1998) is used. Models for the optically thick winds of the WO stars cannot be computed from an initial grey solution. Instead, they start out with an existing atmosphere model from which a new model is calculated for only slightly different parameters. As line-blanketing is self-consistently taken into account, and all transfer equations are solved in the co-moving frame, each of these models can take up to a week to compute. This computing time prevents the automated fitting method described above, and instead the parameter space needs to be explored by making educated guesses for the change in parameters. Therefore, no formal error bars can be calculated, although the uncertainties in the parameters can to some extent be quantified by the amount of change that is needed to significantly change the output spectrum.

—

On the mass-loss rate of massive stars in the low-metallicity galaxies IC 1613, WLM, and NGC 3109

F. Tramper, H. Sana, A. de Koter & L. Kaper

The Astrophysical Journal Letters, 2011, 741, L8

Abstract

We present a spectroscopic analysis of VLT/X-Shooter observations of six O-type stars in the low-metallicity ($Z \sim 1/7 Z_{\odot}$) galaxies IC 1613, WLM and NGC 3109. The stellar and wind parameters of these sources allow us, for the first time, to probe the mass-loss versus metallicity dependence of stellar winds below that of the Small Magellanic Cloud (at $Z \sim 1/5 Z_{\odot}$) by means of a modified wind momentum versus luminosity diagram. The wind strengths that we obtain for the objects in WLM and NGC 3109 are unexpectedly high and do not agree with theoretical predictions. The objects in IC 1613 tend towards a higher than expected mass loss rate, but remain consistent with predictions within their error bars. We discuss potential systematic uncertainties in the mass-loss determinations to explain our results. However, if further scrutinization of these findings point towards an intrinsic cause for this unexpected sub-SMC mass-loss behavior, implications would include a higher than anticipated number of Wolf-Rayet stars and Ib/Ic supernovae in low-metallicity environments, but a reduced number of long-duration gamma-ray bursts produced through a single-star evolutionary channel.

2.1 Introduction

The evolution of massive stars is greatly affected by the amount of mass and angular momentum that is lost during their lifetime. Understanding the mechanisms responsible for these losses is a fundamental goal in stellar astrophysics. For instance, mass loss influences the characteristics of the supernova explosion with which a massive star ends its life, as well as the number of potential single-star progenitors of long-duration gamma-ray bursts (e.g. Yoon & Langer 2005; Woosley & Bloom 2006).

An important mass-loss mechanism, at least at Galactic and Magellanic Cloud metallicities, is the transfer of momentum from photons to the atmospheric gas through line interactions, initiating and driving an outflow (e.g., Castor et al. 1975; Kudritzki & Puls 2000; Vink et al. 2001). The strength of these radiation-driven winds therefore depends on the effective number of absorption lines, in particular near the photospheric flux maximum in the ultraviolet. It is dominated by the absorption of light through a copious amount of metallic ion lines that are present in this wavelength region. As a consequence, the mass-loss rate (\dot{M}) of stars hotter than 25 000 K is predicted to scale with metallicity (Z) as $\dot{M} \propto Z^{0.69 \pm 0.10}$ (Vink et al. 2001). Mokiem et al. (2007) showed that this prediction holds for early-type stars in the Galaxy ($Z = Z_{\odot}$), Large Magellanic Cloud (LMC; $Z = 0.5 Z_{\odot}$), and Small Magellanic Cloud (SMC; $Z = 0.2 Z_{\odot}$), yielding the empirical relation $\dot{M} \propto Z^{0.78 \pm 0.17}$. To date however, no observational constraints exist at sub-SMC metallicities.

For Galactic stars more luminous than $10^{5.8} L_{\odot}$ (i.e. above the Humphreys-Davidson limit), episodic mass loss is expected to occur during the Luminous Blue Variable and/or Wolf-Rayet phase (e.g., Humphreys & Davidson 1994; Smith et al. 2004). Also, dust/pulsation-driven mass loss takes place in the red supergiant phase of lower luminosity objects (e.g., Heger et al. 1997; Yoon & Cantiello 2010). However, if the *relative* contribution of line driving remains sizable at all Z , an important consequence of the theory of radiation-driven winds would be that low-metallicity massive stars lose less mass and angular momentum over their lifetime than their high-metallicity counterparts. At sub-SMC metallicities, single stars with a large initial rotational velocity may avoid envelope expansion and the associated efficient transfer of angular momentum from the core to the envelope, thus keeping a rapidly spinning core. This makes them potential progenitors of long-duration gamma-ray bursts (e.g. Woosley & Bloom 2006).

In order to observationally constrain stellar and wind parameters at sub-SMC metallicities, we have used the X-Shooter spectrograph mounted on ESO's *Very Large Telescope* (VLT) UT2 (Vernet et al. 2011) to secure intermediate-resolution spectra of some of the most massive stars in three nearby dwarf galaxies, IC 1613, WLM and NCG 3109, each having a metallicity of $Z \approx 1/7 Z_{\odot}$. The throughput of the instrument, combined with the collecting area of an 8.2m telescope, allows us,

Table 2.1: Properties of the observed stars

ID	R.A. (J2000)	Dec. (J2000)	V	M_V	Spectral Type	R.V. km s ⁻¹	12+log(O/H)
<i>IC 1613</i> ^a							
-A13	01 05 06.21	+02 10 44.8	19.02	-5.55	O3 V((f))	-240	8.0
-A15	01 05 08.74	+02 10 01.1	19.35	-5.11	O9.5 III	-240	—
-B11	01 04 43.82	+02 06 46.1	18.68	-5.84	O9.5 I	-240	—
-C9	01 04 38.63	+02 09 44.4	19.02	-5.44	O8 III((f))	-265	—
<i>WLM</i> ^b							
-A11	00 01 59.97	-15 28 19.2	18.40	-6.83	O9.7 Ia	-135	—
<i>NGC 3109</i> ^c							
-20	10 03 03.22	-26 09 21.4	19.33	-6.67	O8 I	407	7.8

Notes. V -band magnitudes from ^(a) Bresolin et al. (2007) ^(b) Bresolin et al. (2006) ^(c) Evans et al. (2007)

for the first time, to perform a detailed quantitative spectral analysis at a resolution $R \sim 6000$ - 9000 and test the theory of line driving in O-type stars at a sub-SMC metallicity (see also Herrero et al. 2011).

With the aid of previous, low-resolution studies (Bresolin et al. 2006, 2007; Evans et al. 2007), we selected the six visually brightest O-type stars in these galaxies (four in IC 1613, one in both WLM and NGC 3109). The low line-of-sight extinction towards these galaxies and their similar metallicity allow us, for this particular study, to treat these stars as a group.

In Section 2.2 the observations and data reduction are described. Section 2.3 discusses the method of analysis and Section 2.4 presents and discusses the results. Finally, we give our conclusions in Section 2.5.

2.2 Observations and data reduction

The spectrum of NGC 3109-20 has been obtained during a X-Shooter GTO run on 2010 April 23, with an exposure time of 5x900s. In a successive GTO run from 2010 September 12 to 16, the stars in IC 1613 and WLM were observed, with an exposure time of 6x900s for all stars. All observations were obtained in nodding mode with a nod throw of 5", using a slit width of 0.8" for the UVB arm (300-550 nm), 0.9" for the VIS arm (550-1020 nm), and 0.9" for the NIR arm (1 000-2 500 nm), yielding a spectral resolving power of $R=6\,200$, $8\,800$ and $5\,600$, respectively. Conditions were clear or photometric with an average seeing below 0.8" in the R band. The moon illumination fraction was below 0.2. Fundamental properties of the observed stars are listed in Table 2.1.

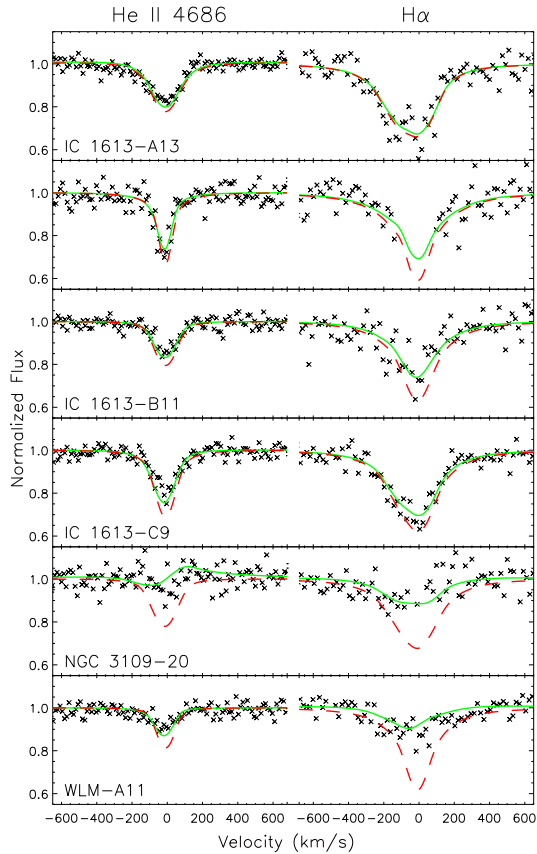


Figure 2.2: Line profiles of the mass-loss sensitive diagnostic lines He II 4686 and $H\alpha$. The best-fit line profiles are overplotted with solid lines. The dashed profiles indicate models with mass-loss rates predicted by radiation-driven wind theory.

the stars was determined by comparing with a spectral atlas of O-type stars (Sana et al., in preparation), and for all but one agree with the type listed in the literature. The only change is that the spectral type of IC1613-A13 is refined from O3-4 V((f)) (Bresolin et al. 2007) to O3 V((f)).

2.2.2 Oxygen abundance determination

In order to also provide an independent oxygen abundance measurement, a relative flux calibration was performed for the frames where nebular oxygen emission is present (IC 1613-A13 and NGC 3109-20), using spectra of photometric standard stars taken during each night of observations. To derive the oxygen abundance, we

use the strong line method (Pagel et al. 1979) with the updated calibration by Pilyugin & Thuan (2005), using the [O II] $\lambda\lambda$ 3727,3729, [O III] $\lambda\lambda$ 4959,5007 and H β nebular emission lines. The resulting abundances are given in Table 2.1, and although abundances derived with the strong line method can have uncertainties up to 0.8 dex (see e.g. Bresolin et al. 2009), our measures agree well with the literature values of $12 + \log(\text{O}/\text{H}) = 7.90 \pm 0.08$ (IC 1613; Bresolin et al. 2007), 7.80 ± 0.07 (WLM; Urbaneja et al. 2008) and 7.76 ± 0.07 (NGC 3109; Evans et al. 2007) derived from B- and A-type supergiants.

2.3 Modeling

The stellar properties and wind characteristics of the stars have been determined using an automated fitting method developed by Mokiem et al. (2005). This method combines the non-LTE stellar atmosphere model FASTWIND (Puls et al. 2005) with the generic fitting algorithm PIKAIA (Charbonneau 1995). It allows for a fast and homogeneous analysis of our sample of stars using a selection of hydrogen, He I, and He II lines.

The absolute visual magnitude (M_V) of the stars is needed as an input parameter. They have been determined using the V magnitudes from Table 2.1 and a distance and reddening of $d = 721$ kpc (Pietrzyński et al. 2006) and $E(B - V) = 0.025$ (Schlegel et al. 1998) for IC 1613, $d = 995$ kpc and $E(B - V) = 0.08$ for WLM (Urbaneja et al. 2008), and $d = 1300$ kpc (Soszyński et al. 2006) and $E(B - V) = 0.14$ (Davidge 1993) for NGC 3109. The resulting values of M_V agree well with the values for their spectral type (Martins et al. 2005). The radial velocity (RV) has been measured by fitting a Gaussian profile to the hydrogen lines, and the obtained values are in agreement with the radial velocities of the host galaxies.

The fitting algorithm covers a large parameter space, fitting line profiles of the same 11 spectral lines as described by Mokiem et al. (2005) to determine the effective temperature (T_{eff}), gravity (g), mass-loss rate (\dot{M}), surface helium abundance ($N_{\text{He}}/N_{\text{H}}$), depth-independent microturbulent velocity (v_{tur}), and projected rotational velocity ($v_{\text{rot}} \sin i$). The bolometric luminosity (L) is derived by applying the bolometric correction to the absolute visual magnitude used as input. This luminosity, together with the obtained temperature, is then used to determine the radius (R) of the star. The terminal wind velocity (v_{∞}) can not be constrained from the optical, but is related to the surface escape velocity v_{esc} : $v_{\infty} = 2.6 v_{\text{esc}}$ (at $Z = Z_{\odot}$; Lamers et al. 1995; Kudritzki & Puls 2000). The coefficient of the wind velocity structure β has been fixed to 0.8 for the dwarfs, 0.9 for the giants, and 0.95 for the supergiants, conform theoretical predictions (Muijres et al. 2012).

Table 2.2 presents the best-fit values and derived properties for the six stars. The

Table 2.2: Best-fit parameters and derived properties of the observed stars. Arrows indicate upper or lower limits.

ID	T_{eff} (kK)	$\log g$ (cm s^{-2})	$\log \dot{M}$ ($M_{\odot} \text{ yr}^{-1}$)	$N_{\text{He}}/N_{\text{H}}$	v_{tur} (km s^{-1})	$v_{\text{rot}} \sin i$ (km s^{-1})	v_{∞} (km s^{-1})	$\log L$ (L_{\odot})	R (R_{\odot})
<i>IC 1613</i>									
-A13	$47.6^{+4.73}_{-4.95}$	$3.73^{+0.13}_{-0.22}$	$-6.26^{+0.45}_{-0.50}$	$0.32^{+0.04}_{-0.17}$	4^{+25}_{\downarrow}	94^{+40}_{-28}	1869	5.78	11.4
-A15	$33.7^{+3.10}_{-2.65}$	$3.76^{\uparrow}_{-0.39}$	$-6.36^{\uparrow}_{-0.40}$	$0.16^{+0.14}_{-0.10}$	9^{+17}_{\downarrow}	34^{+42}_{-24}	1971	5.24	12.2
-B11	$31.3^{+2.00}_{-2.00}$	$3.41^{+0.24}_{-0.21}$	$-6.16^{+0.30}_{-1.30}$	$0.13^{+0.11}_{-0.07}$	12^{+13}_{\downarrow}	88^{+36}_{-28}	1601	5.45	18.1
-C9	$35.7^{+1.70}_{-1.85}$	$3.58^{+0.19}_{-0.24}$	$-6.26^{+0.25}_{-0.60}$	$0.12^{+0.10}_{-0.04}$	15^{+8}_{\downarrow}	72^{+28}_{-28}	1697	5.43	13.6
<i>WLM</i>									
-A11	$29.7^{+2.45}_{-2.75}$	$3.25^{+0.29}_{-0.19}$	$-5.56^{+0.20}_{-0.30}$	$0.11^{0.11}_{\downarrow}$	8^{+14}_{\downarrow}	70^{+40}_{-36}	1711	5.79	29.8
<i>NGC 3109</i>									
-20	$34.2^{+4.70}_{-3.05}$	$3.48^{+0.37}_{-0.40}$	$-5.41^{+0.25}_{-0.35}$	$0.11^{\uparrow}_{\downarrow}$	$16^{\uparrow}_{\downarrow}$	98^{+86}_{-72}	2049	5.88	24.7

values for T_{eff} are higher than those of their Galactic counterparts of the same spectral type (Martins et al. 2005), in agreement with their low metallicity (Mokiem et al. 2004). IC 1613-A13 shows an unusually high value for N_{He} . This is likely caused by the degeneracy between effective temperature and surface helium abundance at high temperatures (resulting from the loss of He I as a diagnostic). The large uncertainties in the determination of the micro-turbulent velocity show that this parameter cannot be well constrained with our data.

The errors on the parameters have been analyzed by calculating the probability ($P = 1 - \Gamma(\chi^2/2, \nu/2)$), where Γ is the incomplete gamma function and ν the degrees of freedom) for all calculated models. Because P is very sensitive to the value of the χ^2 , we normalize all χ^2 values such that the best χ_{red}^2 is equal to 1, i.e. we assume that deviations of the original best χ_{red}^2 from unity are induced by under- or overestimated errorbars on the normalized flux. This approach is similar in spirit to using relative weighting in the χ^2 merit function and to propagating the root-mean-square of the fit to scale the error bars (e.g., Press et al. 1986). The uncertainties are obtained by considering the range of models which satisfy $P > 5\%$. These errors do not take into account uncertainties in the luminosity. However, as the mass-loss rate approximately scales with luminosity as $\dot{M} \propto L^{5/4}$, typical uncertainties in L do not have a significant impact on our conclusions.

2.4 Results and discussion

The derived mass-loss rates are represented in the modified wind-momentum vs. luminosity diagram (WLD, Figure 2.3). The modified wind momentum is defined as $D_{\text{mom}} = \dot{M}v_{\infty}\sqrt{R/R_{\odot}}$. This quantity is ideally suited to study the $\dot{M}(Z)$ relation because it is almost independent of mass, and v_{∞} and R are usually relatively well constrained. As the H α recombination line is essentially sensitive to the invariant wind-strength parameter $Q = \dot{M}/(R^{3/2}v_{\infty})$ that is inferred from the spectral analysis, D (for given T_{eff}) scales with L , making it less sensitive to uncertainties in the luminosity. As v_{∞} is expected to scale with metallicity ($v_{\infty} \propto Z^{0.13}$; Leitherer et al. 1992), and the wind-strength parameter Q is invariant, the derived mass-loss rate is subject to a similar scaling. This scaling of \dot{M} and v_{∞} has been applied to the values given in Table 2.2.

Compared to theoretical expectations (Vink et al. 2001, $Z = 0.14Z_{\odot}$ dashed line in Figure 2.3), all stars except IC 1613-A13 tend toward a higher than predicted mass-loss rate for their metallicity. Compared to the empirical relations found by Mokiem et al. (2007), our values are reminiscent of the values measured for the LMC. For IC 1613-A15 we could only obtain an upper limit due to the nebular contamination, and IC 1613-B11 and C9 could have a low enough mass-loss rate within the errors.

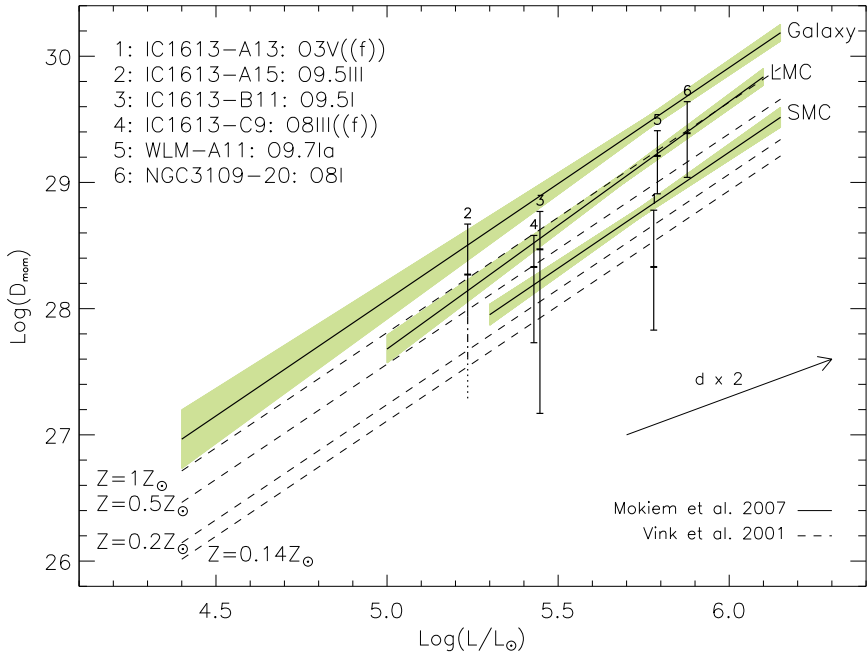


Figure 2.3: Modified wind-momentum vs. luminosity diagram with our results. The dashed lines indicate the theoretical predictions of Vink et al. (2001), and the empirical results from Mokiem et al. (2007) are represented by the shaded bars. The arrow illustrates the effect of an uncertainty in the distance on the location of points in the diagram.

WLM-A11 and NGC 3109-20 have a well defined mass-loss rate which is almost an order of magnitude too large for their metallicity.

2.4.1 Systematic uncertainties in the mass-loss determination

In addition to random uncertainties, several sources of systematic uncertainties may affect our mass-loss determinations, for instance due to assumptions we have made. Here we discuss potential non-intrinsic causes for the high mass-loss rates that we derive.

The adopted values of the flow acceleration parameter β could contribute to the high values of D_{mom} . To fit the line profile, the wind density vs. velocity profile must be the same, causing a higher value of β to give a lower mass-loss rate. If we underestimated β the mass-loss rate will therefore be too high. However, even for extreme values of β , the correction will be at most a factor of two. The assumption that $v_{\infty} = 2.6 v_{\text{esc}}$ introduces an uncertainty in D_{mom} , but as errors in the terminal flow velocities are not expected to exceed 20-40% (Groenewegen et al. 1989), this

effect is even smaller.

Another source of uncertainty is the luminosity determination, both through extinction and distance uncertainties. However, as said before, the WLD is not very sensitive to uncertainties in L , as an increase in L almost linearly increases the value of D_{mom} . This effect is illustrated by the arrow in Figure 2.3, indicating a change of a factor of two in distance. Furthermore, since the extinction towards all galaxies appears very low, and the absolute magnitude of the stars (Table 2.1) agrees well with the values for their spectral type (Martins et al. 2005), we do not expect a significant error in the luminosity.

An underestimated metallicity could also be part of an explanation for the difference in empirical and predicted mass-loss rates. However, the various studies mentioned in Table 2.1 all agree on an oxygen abundance of 10-15% solar. Our own determination of the oxygen abundance for IC 1613 and NGC 3109 also agrees with these values. Furthermore, earlier studies on the stellar populations of our target galaxies (Cole et al. 1999; Minniti & Zijlstra 1997; Minniti et al. 1999) derived iron abundances of again 10-15% solar.

Finally, multiplicity could play a role. Since the observed spectroscopic binary fraction in the Galaxy is approximately 50% (Mason et al. 2009; Sana & Evans 2011), it is possible that some of our sources are binaries. Binarity can influence the derived mass-loss rate by dilution or wind-wind collisions. In the case of a low-mass companion, the normalized spectrum will have shallower lines due to dilution effects. In close binaries with two massive stars, wind-wind collisions can cause emission in He 2 $\lambda 4686$ and H α if the wind-collision region is isothermal (see, for example, Sana et al. 2001). However, we could not find indications for massive companions in our data, which would cause higher luminosities, nor of radial velocities that differ from those of the parent galaxy.

Because of the large distance to the host galaxies, it is possible that our targets are unresolved multiples instead of single stars (e.g., Hartoog et al. 2012). With a seeing of 0.8", the smallest resolved area covers a distance ranging from 2.8 pc for IC 1613 to 5 pc for NGC 3109, and can therefore easily harbor a typical open cluster. However, the observed luminosities are typical of stars of the corresponding spectral type (Martins et al. 2005), and we therefore do not see any strong indications for multiplicity.

2.4.2 Possible intrinsic causes for the high mass-loss rates

There are several physical mechanisms that can increase the mass-loss rate or make it appear higher. A likely cause is the effect of wind clumping, which we do not take into account in our modeling. Clumping causes mass-loss indicators based on the average squared density $\langle \rho^2 \rangle$, such as H α , to have more emission than would

be the case in an unclumped wind. This causes the derived mass-loss rates to be overestimated by a factor of $1/\sqrt{f}$, with f the mean value of the volume-filling factor in the line-forming region (Puls et al. 2008).

However, by comparing our results to the relations found by Mokiem et al. (2007), where clumping is also unaccounted for (causing the empirical mass-loss rate to be higher than the theoretical prediction), the rates we find for $Z \sim 0.14 Z_{\odot}$ galaxies coincide with LMC values. So unless clumping behaves differently at sub-SMC metallicities, we would still expect the mass-loss rates to be located below the empirical SMC area in the WLD.

The slope and absolute scaling of the WLD is also anticipated to change at very low metallicities (Kudritzki 2002). The expected effect, however, works in the opposite direction, and the mass-loss rates should be even lower. Furthermore, the slope-change is predicted to occur at a much lower metallicity ($Z \approx 10^{-3} Z_{\odot}$).

Fast rotation can also cause increased and asymmetric mass-loss (e.g., Maeder & Meynet 2000). However, all of the projected rotational velocities we derive are low ($v \sin i < 100 \text{ km s}^{-1}$), and given that the probability that by chance all sources have their rotational axis pointed more or less in our direction is small, we do not expect this effect to play a major role in our sample.

There could be other processes affecting the mass-loss process, possibly related to pulsations and magnetic fields, which both have been detected in O-type stars (e.g. Henrichs 1999; Donati & Landstreet 2009). Pulsations are caused by the high sensitivity of opacity to temperature in the high-temperature low-density regions in O (super)giants, giving rise to κ -pulsations (e.g. Iglesias et al. 1992). This is induced by the sudden appearance of a large number of same-shell transition lines of iron, and is therefore dependent on the iron abundance. Thus it is expected that pulsations are less important at low metallicities (Baraffe et al. 2001).

The increased opacity described above can give rise to small convective regions in the stellar envelope (Cantiello et al. 2009). Cantiello & Braithwaite (2011) showed that these convective regions can produce magnetic hot spots through the dynamo effect, which can be strong enough to influence the wind and possibly play a role in the wind clumping. This effect is again metallicity dependent, and is expected to play a lesser role and eventually disappear with decreasing metallicity (Cantiello et al. 2009).

2.5 Conclusions and implications

In this chapter, we have pointed out a discrepancy between the observed and predicted mass-loss rates from massive stars in low-metallicity environments, and discussed possible explanations.

A potential violation of the expected metallicity scaling of the radiation-driven mass-loss rate at $Z \sim 1/7 Z_{\odot}$, resulting in higher than expected mass-loss rates, would have far-reaching implications. Firstly, one expects low- Z O-type stars to suffer more from spin-down through angular momentum loss in the stellar wind. Consequently, the rotational mixing efficiency may be reduced, leading, for instance, to a more modest nitrogen enrichment than currently thought (Brott et al. 2011).

Secondly, one anticipates the single O-star population in low metallicity environments to produce more observationally identifiable Wolf-Rayet stars, being the successors of O-type stars that had their outer envelope stripped by mass loss, and therefore increased number of Ib and, potentially, Ic supernovae. The single-star channel would, however, produce less progenitors of long-duration gamma-ray bursts, as the stars lose more angular momentum by their outflow.

Finally, if the larger than expected wind strength at $Z \sim 1/7Z_{\odot}$ persists to extremely low metallicities (though at present the driving mechanism is unknown), stellar winds will impact the evolution of massive Population III stars and the chemical enrichment of the intergalactic medium of the early Universe.

Acknowledgments

We thank the referee of the published paper, dr. Kudritzki, for his useful comments. We also thank dr. Martayan for his support during the observations, and O. Hartoog for the interesting discussions.

The properties of ten O-type stars in the low-metallicity galaxies IC 1613, WLM and NGC 3109

F. Tramper, H. Sana, A. de Koter, L. Kaper & O.H. Ramírez-Agudelo

Astronomy and Astrophysics, in press

Abstract

Massive stars likely played an important role in the reionization of the Universe, and the formation of the first black holes. They are potential progenitors of long-duration gamma-ray bursts, seen up to redshifts of about ten. Massive stars in low-metallicity environments in the local Universe are reminiscent of their high redshift counterparts, emphasizing the importance of the study of their properties and evolution. In the previous chapter, we reported on indications that the stellar winds of low-metallicity O stars may be stronger than predicted, which would challenge the current paradigm of massive star evolution. In this chapter, we aim to extend our initial sample of six O stars in low-metallicity environments by four. The total sample of ten stars consists of the optically brightest sources in IC1613, WLM, and NGC3109. We aim to derive their stellar and wind parameters, and compare these to radiation-driven wind theory and stellar evolution models. We have obtained intermediate-resolution VLT/X-Shooter spectra of our sample of stars. We derive the stellar parameters by fitting synthetic `FASTWIND` line profiles to the VLT/X-Shooter spectra using a genetic fitting algorithm. We compare our parameters to evolutionary tracks and obtain evolutionary masses and ages. We also investigate the effective temperature versus spectral type calibration for SMC and lower metallicities. Finally, we reassess the wind momentum versus luminosity diagram. The derived parameters of our target stars indicate stellar masses that reach values of up to $50 M_{\odot}$. The wind strengths of our stars are, on average, stronger than predicted from radiation-driven

wind theory and reminiscent of stars with an LMC metallicity. We discuss indications that the iron content of the host galaxies is higher than originally thought and is instead SMC-like. We find that the discrepancy with theory is lessened, but remains significant for this higher metallicity. This may imply that our current understanding of the wind properties of massive stars, both in the local universe as well as at cosmic distances, remains incomplete.

3.1 Introduction

It is expected that in the early, metal-poor Universe the formation of massive stars was favored. These stars may have played an important role in the reionization of the gas that was cooling as a result of the expansion of space (e.g., Haiman & Loeb 1997), and produced the first black holes (e.g., Madau & Rees 2001; Micic et al. 2011). The final collapse of single rapidly rotating massive stars in low-metallicity environments is a potential channel toward the production of hypernovae and long-duration gamma-ray bursts (e.g., Yoon & Langer 2005; Woosley & Bloom 2006).

The study of low-metallicity massive stars is thus crucial in our understanding of the early Universe. While the Magellanic Clouds provide access to massive stars in environments with metallicities down to 20% of solar, for lower metallicities we have to look to more pristine dwarf galaxies in the Local Group. With 8-10m class telescopes, the stellar populations in these galaxies can be resolved, but obtaining spectra of individual massive stars hosted by these systems remains challenging and expensive in terms of observing time. Consequently, this has so far mostly been done at low spectral resolution (at resolving power $R = \lambda/\Delta\lambda \sim 1\,000 - 2\,000$; e.g., Bresolin et al. 2006, 2007; Evans et al. 2007; Castro et al. 2008).

The advent of X-Shooter (Vernet et al. 2011) on ESO's Very Large Telescope (VLT) has opened up the opportunity to observe massive stars in galaxies as far as the edge of the Local Group at intermediate resolution ($R \sim 5\,000 - 11\,000$, Hartoog et al. 2012). Apart from the better resolved shapes of the spectral lines, a higher spectral resolution facilitates a better nebular subtraction. This allows for a more detailed quantitative spectroscopic analysis.

As the mass loss of massive stars through their stellar winds dominates their evolution, understanding the physical mechanism driving these winds is very important. The winds are thought to be driven by radiation pressure on metallic ion lines (e.g., Lucy & Solomon 1970; Castor et al. 1975; Kudritzki & Puls 2000). Consequently, the strength of the stellar winds is expected to scale with metallicity, with the prediction that $\dot{M} \propto Z^{0.69 \pm 0.10}$ (Vink et al. 2001). This metallicity scaling has been verified empirically by Mokiem et al. (2007), who find $\dot{M} \propto Z^{0.78 \pm 0.17}$ for O stars in the Galaxy and Magellanic Clouds.

To quantify the $\dot{M}(Z)$ relation in even lower metallicity environments, we presented the first intermediate-resolution quantitative spectroscopic analysis of O-type stars with a oxygen abundance that suggests a sub-SMC metallicity in Tramper et al. (2011, Chapter 2). We unexpectedly found stellar winds that are surprisingly strong, reminiscent of an LMC metallicity. This apparent discrepancy with radiation-driven wind theory is strongest for two stars, one in WLM and one in NGC 3109. Herrero et al. (2012) also report a stronger than predicted wind strength for an O-type star in IC 1613. However, observations of a larger sample of stars, as well as observa-

Table 3.1: Adopted properties of the host galaxies.

Galaxy	d (kpc)	$E(B - V)$	Z/Z_{\odot}^a	References
IC 1613	720	0.025	0.16	1, 2, 3
WLM	995	0.08	0.13	4
NGC 3109	1300	0.14	0.12	5, 6, 7

Notes. ^(a) Metallicity for IC 1613 and NGC 3109 are derived from B-supergiants and based on the oxygen abundance, adopting $12 + \log(\text{O}/\text{H})_{\odot} = 8.69$ (Asplund et al. 2009). WLM metallicity is based on abundances of iron-group elements obtained from B-supergiants.

References. (1) Pietrzyński et al. (2006); (2) Schlegel et al. (1998); (3) Bresolin et al. (2007); (4) Urbaneja et al. (2008); (5) Soszyński et al. (2006); (6) Davidge (1993); (7) Evans et al. (2007)

tions in the UV, are necessary to firmly constrain the wind properties of these stars and to prove or disprove that O stars at low metallicities have stronger winds than anticipated.

A first step towards this goal has been made by Garcia et al. (2014), who obtained HST-COS spectra of several O-type stars in IC 1613, and used these to derive terminal wind velocities. They show that the wind momentum for the star analysed by Herrero et al. (2012) can be reconciled with the theoretical predictions when their empirical value for the terminal velocity is adopted. They also find indications that the α -to-iron ratio in IC 1613 may be sub-solar, which could partly explain the observed strong winds. A full analysis of the UV spectrum to constrain the mass-loss properties of the stars in their sample is still to be done.

In this chapter, we extend our optical sample of O stars in low-metallicity galaxies by four. We constrain the physical properties of the full sample of ten O stars and reassess their winds strengths. Furthermore, we discuss the evolutionary state of the objects, that are among the visually brightest of their host galaxies. We use our results in combination with results from the literature to reassess the low-metallicity effective temperature versus spectral type scale.

The location of all stars in our sample within their host galaxies is indicated in Figures 3.1, 3.2 and 3.3. The host galaxies are of a late type (dwarf irregulars), and have likely been forming stars continuously during their life (Tolstoy et al. 2009). The distance and metallicity of the host galaxies that we adopt are given in Table 3.1 (but see Section 3.5 for a discussion on the metallicities).

In the next section we give an overview of the observations and the data reduction. In Section 3.3 we describe the analysis and present the results. We discuss the

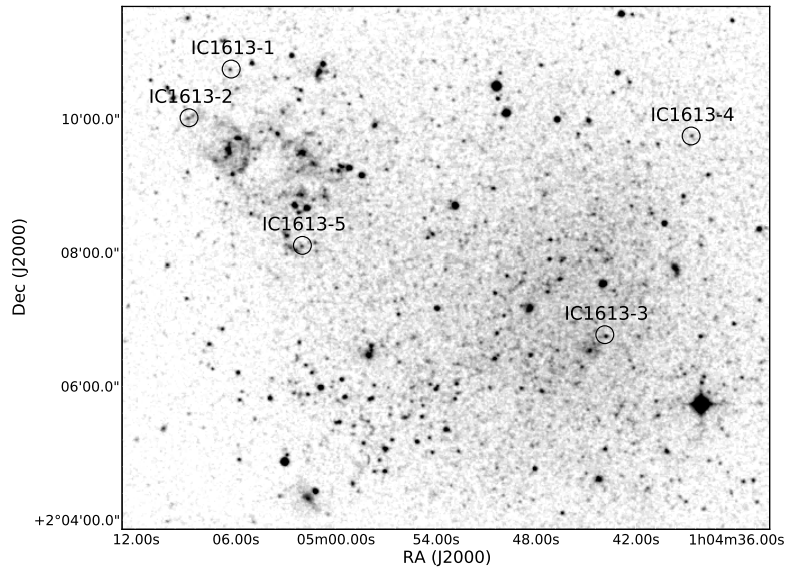


Figure 3.1: Location of the target stars in IC 1613. North is up and east to the left.

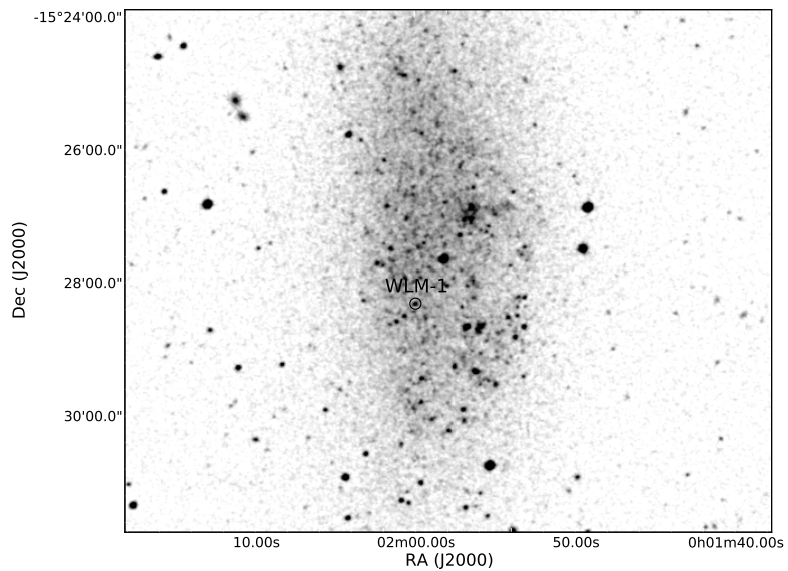


Figure 3.2: Location of the target star in WLM. North is up and east to the left.

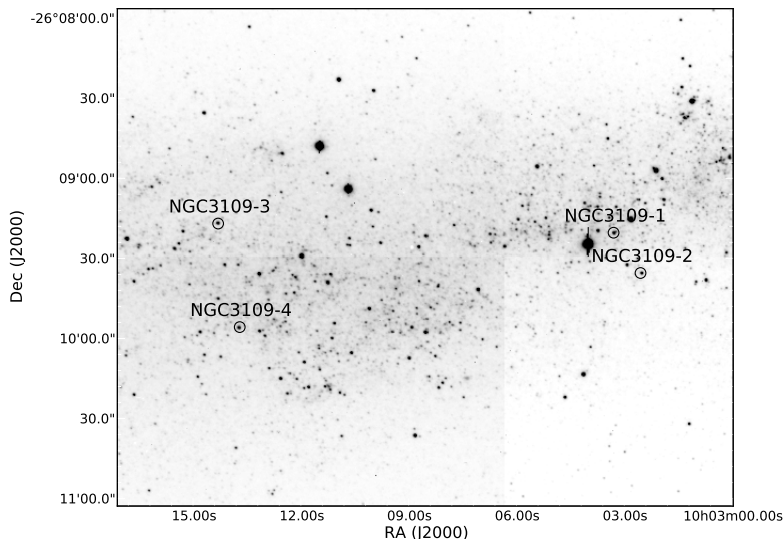


Figure 3.3: Location of the target stars in NGC 3109. North is up and east to the left.

low-metallicity effective temperature scale in Section 3.4, and the wind strengths in Section 3.5. Finally, we discuss the evolutionary properties of the sample and the recent star formation history of the host galaxies in Section 3.6. We summarize our findings in Section 3.7.

3.2 Observations and data reduction

All stars have been observed with X-Shooter (Vernet et al. 2011) at ESO’s Very Large Telescope as part of the NOVA program for guaranteed time observations. An overview of the observational properties of the stars is given in Table 3.2. Throughout this paper, we will use the identification given in this table.

The observations and data reduction of IC1613-1 to 3, WLM-1 and NGC3109-1 (program ID 085.D-0741) are described in Paper I. An overview of observations of the other stars (under program IDs 088.D-0181 and 090.D-0212) is given in Table 3.3. All stars were observed with a slit width of 0.8", 0.9" and 0.9" in the UVB, VIS and NIR arms, respectively. The corresponding resolving power R is 6 200 (UVB), 7 450 (VIS) and 5 300 (NIR). All observations were carried out while the moon was below the horizon or illuminated less than 30% (dark conditions).

The data reduction of the newly observed stars was performed with the X-Shooter pipeline v2.2.0. To obtain uncontaminated 1D spectra, the science reduction was done without sky subtraction for each individual exposure. The resulting 2D spectra

Table 3.2: Observational properties of the target stars.

ID ^a	ID	R.A.	Decl.	V ^b	Spectral Type	M _V	RV
<i>This work</i>	<i>Previous</i>	(J2000)	(J2000)				km s ⁻¹
IC1613-1 (I1) ^{1,3}	A13	01 05 06.21	+02 10 44.8	19.02	O3.5 V((f))	-5.55	-240
IC1613-2 (I2) ^{1,3}	A15	01 05 08.74	+02 10 01.1	19.35	O9.5 III	-5.11	-240
IC1613-3 (I3) ^{1,3}	B11	01 04 43.82	+02 06 46.1	18.68	O9.5 I	-5.84	-240
IC1613-4 (I4) ^{1,3}	C9	01 04 38.63	+02 09 44.4	19.02	O8 III((f))	-5.44	-265
IC1613-5 (I5) ^{2,3}	B7	01 05 01.95	+02 08 06.5	18.99	O9 I	-5.29	-214
WLM-1 (W1) ^{1,4}	A11	00 01 59.97	-15 28 19.2	18.40	O9.7 Ia	-6.83	-135
NGC3109-1 (N1) ^{1,5}	20	10 03 03.22	-26 09 21.4	19.33	O8 I	-6.67	407
NGC3109-2 (N2) ^{2,5}	33	10 03 02.45	-26 09 36.11	19.57	O9 If	-6.41	504
NGC3109-3 (N3) ^{2,5}	34	10 03 14.24	-26 09 16.96	19.61	O8 I(f)	-6.39	415
NGC3109-4 (N4) ^{2,5}	35	10 03 13.65	-26 09 55.76	19.70	O8 I(f)	-6.28	386

Notes. (a) In some figures we use the short notation between brackets. (b) V-magnitudes from (3),(4), and (5).

References. (1) Chapter 2; (2) This work; (3) Bresolin et al. (2007); (4) Bresolin et al. (2006); (5) Evans et al. (2007).

Table 3.3: Journal of observations.

ID	HJD	t_{exp} (s)	Average seeing	
	<i>At start of obs.</i>		UVB (")	VIS (")
IC1613-5	2 455 858.653	4x900	1.1	1.0
	2 455 858.705	2x900	1.1	0.9
NGC3109-2	2 456 337.531	4x900	2.2	1.2
	2 456 337.587	4x900	1.4	1.0
	2 456 338.583	4x900	1.4	1.0
	2 456 338.638	4x1200	1.0	0.8
NGC3109-3	2 456 337.643	4x1100	1.1	0.8
	2 456 337.732	4x1100	0.9	0.6
	2 456 338.736	4x900	0.8	0.6
	2 456 338.791	2x900	1.0	0.6
NGC3109-4	2 456 337.797	4x900	1.2	0.7
	2 456 337.853	2x1200	1.7	0.7
	2 456 338.823	4x1200	1.5	0.7

were folded in the wavelength direction and inspected for the presence of other objects in the slit. A clean part of the slit was then used for sky subtraction. The 1D spectra were extracted from the sky-subtracted 2D spectra. As the observed spectra suffer from nebular emission in the hydrogen and He I lines, the extracted spectra were carefully inspected for residuals of nebular lines. If needed, a more suitable part of the slit was used. Whenever residuals remained after this procedure, they were clipped from the spectrum before the analysis.

The 1D spectra of the individual exposures were combined by taking the median flux at each wavelength so cosmic ray hits are removed. Finally, the extracted 1D spectra were normalized by fitting a 4th degree polynomial to the continuum, and dividing the flux by this function. Figure 3.4 shows the resulting normalized spectra of all stars.

The spectra have a signal-to-noise ratio (S/N) between 25 and 45 per wavelength bin of 0.2 \AA in the UVB¹. As expected in O stars, all the spectra show strong hydrogen, He I and He II lines. Some spectra also show weak nitrogen lines.

¹Note that we are oversampling the spectral resolution. A S/N of 25 per wavelength bin of 0.2 \AA corresponds to a S/N of ≈ 50 per resolution element at 4500 \AA .

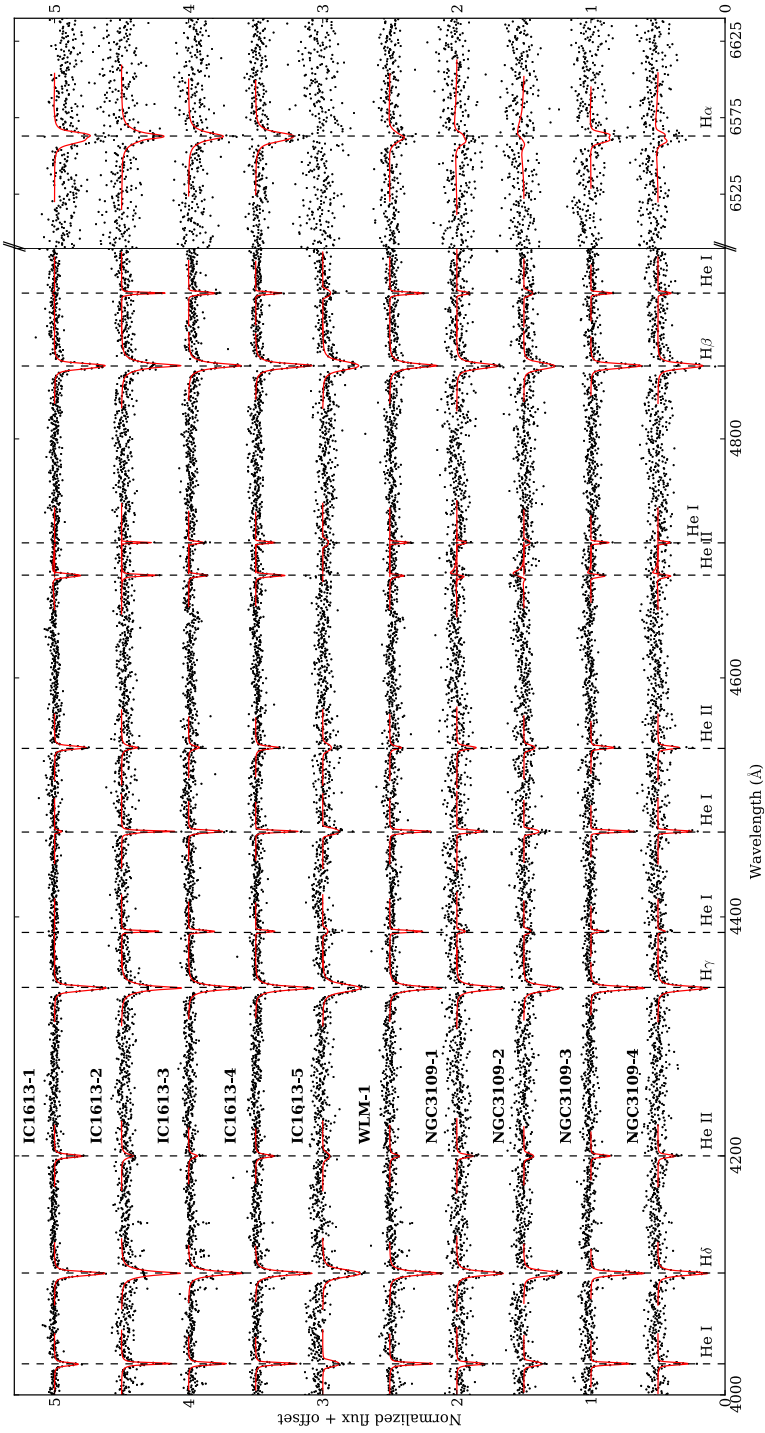


Figure 3.4: Observed spectra (black dots) and best-fit line profiles (red lines). Rest wavelengths of the fitted spectral lines are indicated by the vertical dashed lines. In this plot the wavelength has been corrected for the radial velocities listed in Table 3.2, and binned to 0.5 Å.

3.3 Analysis and results

To investigate the properties of the target stars, we first obtained the stellar and wind parameters by fitting synthetic spectra to the observed line profiles. The method is described in the following section, and the results are presented in Section 3.3.2. The stellar parameters were then used to obtain estimates of the evolutionary parameters (Section 3.3.3). We comment on the results of the individual targets in Section 3.3.4.

3.3.1 Fitting method

To determine the stellar and wind properties, we used an automated fitting method developed by Mokiem et al. (2005). This method fits spectra produced by the non-LTE model atmosphere code `FASTWIND` (Puls et al. 2005) to the observed spectrum using the genetic algorithm based fitting routine `PIKAIA` (Charbonneau 1995). This genetic algorithm (GA) method allows for a thorough exploration of parameter space in affordable CPU time on a supercomputer.

The absolute V -band magnitude (M_V) is needed as input for the GA in order to determine the luminosity (Table 3.2). M_V was calculated using the V magnitudes also given in Table 3.2 and distances and mean reddening listed in Table 3.1.

The radial velocity (RV) of each star is also listed in Table 3.2. These were measured by fitting Gaussians to the $H\gamma$ and $\text{He I } \lambda 4471$ lines and calculating the average velocity needed to match the observed wavelength shifts.

The parameters that are obtained from the atmosphere fitting are the effective temperature (T_{eff}), the surface gravity (g), the mass-loss rate (\dot{M}), the surface helium abundance (N_{He}), the atmospheric microturbulent velocity (v_{tur}) and the projected rotational velocity ($v_{\text{rot}} \sin i$). As in Chapter 2, the parameter describing the rate of acceleration of the outflow (β) can not be constrained from the data, and was fixed to the value predicted by theory ($\beta = 0.95$ for the supergiants presented in this work; Muijres et al. 2012).

The terminal wind velocity (v_{∞}) can not be constrained from the optical spectrum. Therefore, we used the empirical scaling with the escape velocity (v_{esc}) for Galactic stars ($v_{\infty} = 2.65 v_{\text{esc}}$; Kudritzki & Puls 2000), and scaled these using Leitherer et al. (1992, $v_{\infty} \propto Z^{0.13}$) to correct for the lower metallicity. In contrast to Chapter 2, this metallicity scaling has now been implemented into the GA, and was applied before running each individual `FASTWIND` model. Therefore, the mass-loss rate no longer has to be scaled down after the fitting, as was previously needed.

Several additional small changes were implemented in the GA:

- The best-fitting model is now selected based on the χ^2 , which is also used for the error calculation.

Table 3.4: Best-fitting stellar and wind parameters.

ID	T_{eff} (kK)	$\log g$ (cm s^{-2})	$\log \dot{M}$ ($M_{\odot} \text{ yr}^{-1}$)	$N_{\text{He}}/N_{\text{H}}$	v_{tur} (km s^{-1})	$v_{\text{rot}} \sin i$ (km s^{-1})
IC1613-1	$45.40^{+2.00}_{-2.25}$	$3.65^{+0.16}_{-0.10}$	$-5.85^{+0.10}_{-0.50}$	$0.25^{+0.10}_{-0.10}$	24^{+6}_{-15}	98^{+36}_{-44}
IC1613-2	$33.85^{+2.10}_{-2.75}$	$3.77^{+0.33}_{-0.33}$	$-6.35^{+0.35}_{-0.35}$	$0.14^{+0.15}_{-0.08}$	11^{+15}_{-18}	32^{+38}_{-22}
IC1613-3	$31.45^{+1.65}_{-2.45}$	$3.41^{+0.22}_{-0.19}$	$-6.25^{+0.35}_{-1.20}$	$0.15^{+0.09}_{-0.08}$	5^{+18}_{-17}	94^{+32}_{-24}
IC1613-4	$35.2^{+1.85}_{-1.40}$	$3.52^{+0.20}_{-0.11}$	$-6.25^{+0.15}_{-0.50}$	$0.12^{+0.10}_{-0.04}$	17^{+7}_{-9}	76^{+16}_{-26}
IC1613-5	$35.05^{+4.55}_{-4.8}$	$3.74^{+0.44}_{-0.44}$	–	$0.06^{+0.17}_{-0.22}$	27^{+9}_{-9}	270^{+112}_{-92}
WLM-1	$30.60^{+1.70}_{-3.60}$	$3.28^{+0.19}_{-0.31}$	$-5.50^{+0.10}_{-0.35}$	$0.22^{+0.10}_{-0.10}$	9^{+9}_{-9}	72^{+36}_{-22}
NGC3109-1	$35.15^{+3.20}_{-2.55}$	$3.53^{+0.30}_{-0.42}$	$-5.35^{+0.15}_{-0.35}$	$0.09^{+0.22}_{-0.04}$	17^{+50}_{-52}	110^{+50}_{-52}
NGC3109-2	$33.30^{+3.30}_{-2.25}$	$3.35^{+0.43}_{-0.19}$	$-5.45^{+0.30}_{-0.15}$	$0.09^{+0.18}_{-0.05}$	10^{+102}_{-104}	200^{+102}_{-104}
NGC3109-3	$33.05^{+1.45}_{-1.25}$	$3.16^{+0.19}_{-0.11}$	$-5.75^{+0.15}_{-0.25}$	$0.12^{+0.17}_{-0.03}$	23^{+3}_{-5}	82^{+30}_{-32}
NGC3109-4	$35.05^{+3.45}_{-4.45}$	$3.43^{+0.51}_{-0.31}$	$-5.55^{+0.25}_{-0.45}$	$0.08^{+0.15}_{-0.04}$	25^{+5}_{-7}	96^{+60}_{-70}

- He I $\lambda 4922$ is now also fitted in addition to the 11 lines that were used in Chapter 2.
- The minimum microturbulent velocity v_{tur} is set to 5 instead of 0, as FASTWIND models with $v_{\text{tur}} < 5$ may not be accurate.
- The error on the flux is now based on the signal-to-noise ratio (S/N) calculated near each of the fitted lines, instead of a single value for each X-Shooter arm.

To present a homogeneous analysis, we have re-analysed the stars of Chapter 2 with the updated fitting routine, and we present the new parameters here. In general, the new values are in excellent agreement with those presented in Chapter 2. The exception is IC1613-A1, where H α was not properly normalized in Chapter 2. For this star we re-normalized H α , resulting in a somewhat higher mass-loss rate.

Table 3.4 presents the best-fit parameters for each of the target stars. The synthetic spectra of the corresponding FASTWIND models are overplotted on the observed spectra in Figure 3.4 and shown in more detail in Appendix A.

3.3.2 Derived properties and error calculation

In addition to v_{∞} (discussed above), several important quantities can be derived from the best-fit parameters: the bolometric luminosity (L), the stellar radius (R), and the spectroscopic mass (M_{spec}). These are given in Table 3.5. This table also gives the modified wind momentum, which is defined as $D_{\text{mom}} = \dot{M} v_{\infty} \sqrt{R/R_{\odot}}$ and is

Table 3.5: Properties derived from best-fit parameters.

ID	v_∞ (km s ⁻¹)	$\log L$ (L_\odot)	R (R_\odot)	M_{spec} (M_\odot)	$\log D_{\text{mom}}$ (g cm s ⁻² $R_\odot^{1/2}$)
IC1613-1	1755 ⁺³²⁸ ₋₁₆₅	5.71 ^{+0.05} _{-0.06}	11.9 ^{+0.4} _{-0.3}	22.6 ^{+8.4} _{-3.6}	28.73 ^{+0.11} _{-0.53}
IC1613-2	2022 ⁺⁸⁷² ₋₅₉₃	5.21 ^{+0.06} _{-0.09}	11.9 ^{+0.8} _{-0.5}	30.2 ^{+29.0} _{-14.5}	28.29 ^{+0.46} _{-0.53}
IC1613-3	1625 ⁺⁴⁴⁰ ₋₂₉₆	5.42 ^{+0.06} _{-0.08}	17.6 ^{+1.2} _{-0.7}	28.9 ^{+16.4} _{-8.9}	28.38 ^{+0.42} _{-1.19}
IC1613-4	1558 ⁺³⁸⁷ ₋₁₈₄	5.32 ^{+0.06} _{-0.04}	12.5 ^{+0.4} _{-0.5}	18.9 ^{+10.1} _{-4.2}	28.29 ^{+0.19} _{-0.51}
IC1613-5	2010 ⁺²⁶⁷² ₋₇₄₂	5.32 ^{+0.13} _{-0.16}	12.6 ^{+1.5} _{-1.1}	31.6 ^{+129.8} _{-18.4}	–
WLM-1	1777 ⁺⁴³⁵ ₋₄₈₈	5.79 ^{+0.06} _{-0.13}	28.3 ^{+3.0} _{-1.2}	55.6 ^{+30.5} _{-24.3}	29.28 ^{+0.14} _{-0.45}
NGC3109-1	2166 ⁺⁸⁷⁶ ₋₁₃₇₄	5.87 ^{+0.10} _{-0.08}	23.7 ^{+1.4} _{-1.5}	69.1 ^{+65.3} _{-39.7}	29.47 ^{+0.28} _{-0.53}
NGC3109-2	1692 ⁺¹⁰⁵⁸ ₋₃₃₁	5.71 ^{+0.10} _{-0.13}	21.9 ^{+1.2} _{-1.5}	38.9 ^{+65.9} _{-13.7}	29.25 ^{+0.51} _{-0.24}
NGC3109-3	1357 ⁺³²⁸ ₋₁₅₆	5.69 ^{+0.05} _{-0.04}	21.8 ^{+0.7} _{-0.7}	25.0 ^{+13.3} _{-5.32}	28.85 ^{+0.24} _{-0.26}
NGC3109-4	1767 ⁺¹⁴¹² ₋₄₉₂	5.71 ^{+0.11} _{-0.14}	19.8 ^{+0.5} _{-1.3}	38.5 ^{+86.0} _{-17.2}	29.15 ^{+0.45} _{-0.56}

ideal to study the mass loss as it is almost independent of mass. Furthermore, D_{mom} scales with the luminosity through R , making it less sensitive to uncertainties in the luminosity determination.

To derive the error bars given in Tables 3.4 and 3.5, we first divide all χ^2 values with a factor such that the best model has a reduced χ^2 of unity. This ensures meaningful error bars that are not influenced by under or overestimated errors on the flux (see Chapter 2). We then calculate the probability $P = 1 - \Gamma(\chi^2/2, \nu/2)$, with Γ the incomplete gamma function and ν the degrees of freedom, for each model. P quantifies the probability that a χ^2 value differs from the best-fit χ^2 due to random fluctuations. Models that satisfy $P \geq 0.05$ are accepted as providing a suitable fit, and the range covered by the stellar parameters of these models (and the properties derived from them) is taken as the 95% confidence interval. This method also ensures that uncertainties in the parameters that arise due to clipped parts of the spectrum are reflected in the error bars.

3.3.3 Mass and age

To determine the evolutionary parameters of the stars, we use the BONNSAI² tool (Schneider et al. *in preparation*). BONNSAI uses Bayes' theorem to constrain key stellar parameters, such as initial mass and age, by comparing the observed stellar parameters to theoretical predictions from stellar evolution.

We obtained an estimate of the initial mass (M_{ini}), the current mass (M_{act}), the

²The BONNSAI web-service is available at <http://bonnsai.astro.uni-bonn.de>.

Table 3.6: Stellar parameters obtained from comparison with evolutionary tracks using BONNSAI

ID	M_{ini} (M_{\odot})	M_{act} (M_{\odot})	$v_{\text{rot,ini}}$ (km s^{-1})	$v_{\text{rot,act}}$ (km s^{-1})	τ (Myr)
IC1613-1	$49.0^{+3.5}_{-3.4}$	$47.6^{+3.6}_{-3.1}$	100^{+48}_{-40}	100^{+80}_{-54}	$2.32^{+0.31}_{-0.34}$
IC1613-2	$24.6^{+2.1}_{-1.9}$	$24.4^{+1.9}_{-1.8}$	70^{+41}_{-38}	70^{+41}_{-38}	$5.00^{+0.71}_{-0.62}$
IC1613-3	$29.4^{+2.4}_{-2.3}$	$28.8^{+2.2}_{-2.2}$	110^{+40}_{-36}	100^{+49}_{-27}	$4.74^{+0.45}_{-0.36}$
IC1613-4	$28.8^{+1.8}_{-1.4}$	$28.4^{+1.7}_{-1.3}$	80^{+37}_{-28}	80^{+37}_{-28}	$4.40^{+0.32}_{-0.36}$
WLM-1	$41.6^{+6.4}_{-5.3}$	$39.8^{+6.1}_{-4.7}$	90^{+48}_{-29}	90^{+45}_{-32}	$3.58^{+0.49}_{-0.33}$
NGC3109-1	$52.6^{+5.1}_{-4.3}$	$50.0^{+5.1}_{-3.6}$	110^{+59}_{-45}	110^{+59}_{-46}	$2.86^{+0.29}_{-0.22}$
NGC3109-2	$40.0^{+6.4}_{-5.4}$	$38.6^{+6.0}_{-5.0}$	130^{+111}_{-61}	130^{+113}_{-63}	$3.44^{+0.50}_{-0.41}$
NGC3109-3	$42.0^{+2.7}_{-2.3}$	$40.4^{+2.6}_{-2.0}$	90^{+48}_{-31}	90^{+48}_{-31}	$3.54^{+0.19}_{-0.17}$
NGC3109-4	$39.8^{+6.9}_{-5.9}$	$38.6^{+6.5}_{-5.4}$	100^{+62}_{-47}	100^{+63}_{-48}	$3.34^{+0.58}_{-0.47}$

initial and current rotation ($v_{\text{rot,ini}}$ and $v_{\text{rot,act}}$), and the age of the stars. We use the evolutionary tracks for SMC metallicity of Brott et al. (2011), as these are closest in metallicity. As we do not find a significant difference in the temperature of our stars compared to similar SMC stars (see Section 3.4), the use of the SMC tracks does not induce large systematic uncertainties in the evolutionary parameters. As priors to the BONNSAI method we choose a Salpeter (1955) initial mass function, and the Ramírez-Agudelo et al. (2013) 30 Doradus distribution for the initial rotational velocity.

As input observables we used the luminosity, effective temperature, surface gravity and projected rotational velocity. BONNSAI adapts these parameters based on the comparison with the evolutionary predictions. The posterior reproduced parameters are within errors of the input values. The estimated evolutionary parameters are given in Table 3.6. The stellar masses that are derived with the BONNSAI method are in good agreement with the mass estimates that would be derived using the conventional method, i.e. a visual comparison with evolutionary tracks in the Hertzsprung-Russell diagram (HRD, Figure 3.8).

3.3.4 Comments on individual stars

IC1613-1

This is the only dwarf star in the sample, which is reflected by its young derived age (Table 3.6). In Chapter 2, this was the only star with a wind momentum lower than the empirical SMC values from Mokiem et al. (2007). However, as already mentioned, $H\alpha$ was not properly normalized, which caused the mass-loss rate to be

slightly underestimated. In our new analysis of this star we renormalized $H\alpha$, and the updated modified wind momentum is now comparable to those found for SMC stars.

Garcia et al. (2014) obtained the UV spectrum of IC1613-1 using HST-COS, and used it to determine the terminal wind velocity. They find $v_\infty = 2200_{-100}^{+150}$ km s⁻¹, somewhat higher than the values of 1869 km s⁻¹ (Chapter 2) and 1755 km s⁻¹ (this chapter) that we obtain from the scaling with the escape velocity. Their value for the terminal wind velocity would result in a value of $\log(D_{\text{mom}})$ that is ≈ 0.1 dex higher than ours.

IC1613-1 has a low surface gravity for its luminosity class, and is enriched in helium.

IC1613-2

The nebular emission is variable along the X-shooter slit, which prevents a good nebular subtraction. As a consequence, a large part of the core of the Balmer lines had to be clipped from the spectrum before fitting. Without the core of $H\alpha$ we can only derive an upper limit for the mass-loss rate of this star.

IC1613-3 and IC1613-4

Both these stars are well fitted by the atmosphere models. For both stars $H\alpha$ is strongly in absorption and the mass-loss rate cannot be well constrained from this line. This results in fairly large error bars on their modified wind momenta.

IC1613-5

After our observations of this object, it was found to be an eclipsing binary (Bonanos 2013). Our spectra show strong variability in He II $\lambda 4686$ and $H\alpha$ between individual exposures, which may be due to colliding winds (Stevens et al. 1992). Although we provide parameters from fitting the other lines, it is likely that the spectrum is composite (depending on the mass ratio). The listed values are therefore only representative of the composite spectrum. This is a possible cause of the broad spectral lines of IC1613-5 (see Figure 3.4), although the rotational velocity of $v_{\text{rot}} \sin i = 270$ km s⁻¹ that is needed to fit these lines is not unphysically high (see Ramírez-Agudelo et al. 2013). The variability does prevent us to constrain the mass-loss rate and consequently the modified wind momentum of this star. We excluded this star from both the BONNSAI analysis and our discussion of the mass-loss rates (Section 3.5).

Table 3.7: Coefficients for the spectral type - T_{eff} calibrations.

Sample	Unweighted		Weighted	
	a	b	a	b
This work	47584.3	-1595.4	44907.9±4457.2	-1339.1±518.9
Low Z	53398.0	-2203.6	56636.1±766.9	-2677.4±106.1
Low Z (no O3)	48670.7	-1653.2	47283.6±3017.7	-1588.2±356.1
SMC	51929.7	-2138.8	50189.7±1329.2	-1957.2±167.4

Notes. Here, a and b are the coefficients in $T_{\text{eff}} = a + b \times X_{\text{SPT}}$, with X_{SPT} the O subtype.

WLM-1

This is the only star in our sample in WLM, and one of the stars from Chapter 2 which showed a large discrepancy with radiation-driven wind theory. The wind properties derived with the updated GA are very similar to those of Chapter 2. This star also has a high helium abundance.

NGC3109-1

This star shows a strong stellar wind, and is one of the stars in Chapter 2 that exhibits the largest discrepancy with radiation-driven wind theory. While $H\alpha$ is still slightly in absorption, $\text{He II } \lambda 4686$ is fully filled in.

NGC3109-2 and NGC3109-4

Both stars show signs of strong winds in their spectrum. In the fitting, the line center of $H\alpha$ in NGC3109-4 was clipped due to nebular contribution that could not be fully corrected for. $\text{He II } \lambda 4686$ is fully filled in in both stars. $H\alpha$ is fully filled in for NGC3109-2 and almost fully filled in for NGC3109-3. Unsurprisingly, the derived wind momenta for both stars are high.

NGC3109-3

$\text{He II } \lambda 4686$ is almost fully filled in, while $H\alpha$ is still mildly in absorption. This results in a modest wind strength.

3.4 The effective temperature scale

Garcia & Herrero (2013) presented the first effective temperature calibration for potentially sub-SMC metallicities (their Figure 7). In Figure 3.5 we use our results (Ta-

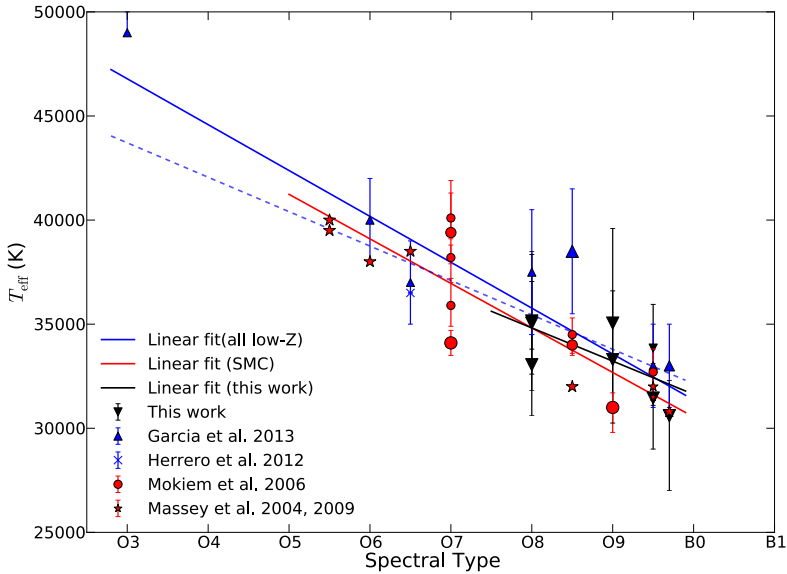


Figure 3.5: Spectral type versus effective temperature calibration for giants and supergiants in low-metallicity environments. Symbol size indicates the luminosity class, with the larger symbols for supergiants. Plotted are results from this work, the Herrero et al. (2012) and Garcia & Herrero (2013) results for IC1613, and the Mokiem et al. (2006) and Massey et al. (2004, 2009) results for the SMC. The solid black line indicates a linear fit to the stars from this paper, not including the error bars on T_{eff} . The red solid line is the unweighted linear fit to the SMC stars, and the blue solid line the fit to the stars in IC 1613, WLM and NGC 3109 (low-Z). The dashed blue line is an unweighted fit to all low-Z results but excluding the single O3 giant. It illustrates the sensitivity of the found relation to this point.

ble 3.4) to provide an updated version of this calibration. Similar to Garcia & Herrero (2013), we first determined the spectral type - T_{eff} relation using an unweighted least-squares linear fit to the temperatures of the giants and supergiants from our work. We did the same for the total sample of low-Z giants and supergiants (this work; Herrero et al. 2012; Garcia & Herrero 2013) and an SMC sample from Mokiem et al. (2006) and Massey et al. (2004, 2009). The coefficients of the derived linear relations are given in Table 3.7.

The updated T_{eff} scale for low metallicities is very similar to the relation found by Garcia & Herrero (2013), and is ≈ 1000 K hotter than the SMC relation. This is expected for a lower metallicity, as the stars are hotter due to a slightly smaller radius (the result of lower opacities in the stellar interior; see e.g., Mokiem et al. 2004). However, as Garcia & Herrero (2013) conclude, the significance of the observed difference between the temperature scales is unclear, given the error bars on the temperatures. Also, the low-Z relation is very sensitive to the position of the only O3 III star in IC 1613, in the region of parameter space where the SMC relation is

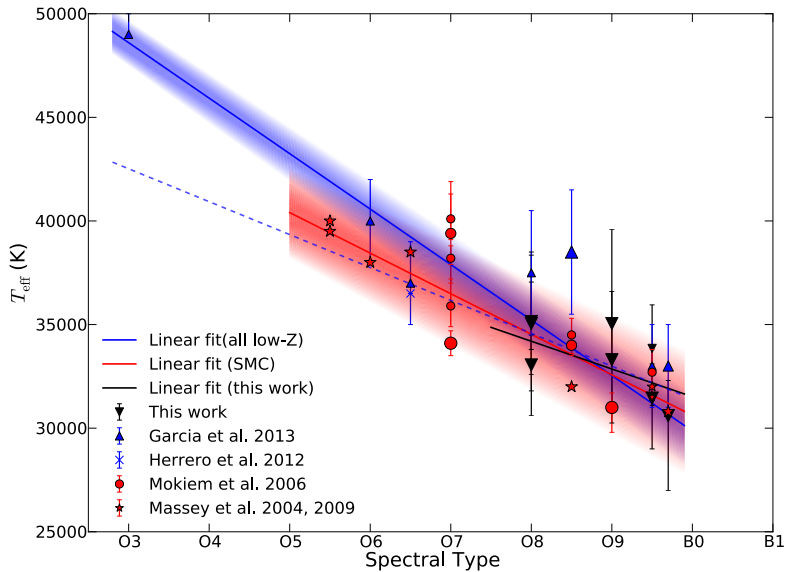


Figure 3.6: Same as Figure 3.5, but with the fitting done including the error bars on T_{eff} . For stars that do not have published error bars, an error of 1 kK was adopted. The shaded areas indicate the uncertainties of the relations found for the SMC and low-metallicity relations.

not constrained. This sensitivity is illustrated by the dotted blue line in Figure 3.5, which is the relation found when the O3 star is excluded from the fit.

As a second step, we included the error bars in our analysis. Figure 3.6 presents the relations that are obtained by weighted least-squares linear fits (i.e. including the error bars on T_{eff}) to the same samples. As the error bars on the temperature presented in Table 3.4 correspond to the 95% confidence interval, we use half these values (roughly corresponding to $\sim 1\sigma$ for normally distributed errors). Because symmetric error bars are easier to handle in a simple approach, we use the average of the upper and lower errors. Massey et al. (2004, 2009) do not provide error bars, and we adopt ± 1000 K for these stars. The coefficients of the relations that we obtain are given in Table 3.7.

The low-metallicity temperature scale obtained from the weighted fits is steeper than the SMC scale, and no longer above it at each point of the spectral range. The error bars on both relations overlap over the entire spectral range covered by the SMC stars. Additionally, the effective temperature at spectral type O8 obtained from our sample, which is well constrained by four stars, is very close to the SMC value regardless of the fitting method.

Thus, with the number of stars that are currently analysed we do not find a significant difference between the effective temperature calibrations for the host galaxies of

the stars studied in this chapter and the SMC. However, a good comparison is hampered by the small sample size, and the absence of early-type giants and supergiants in the SMC sample. Ideally, the low-metallicity effective temperature scale has to be derived from a large number of dwarfs of all subtypes, which are also found in the SMC. However, even if a sufficient number of O-type dwarfs is present in the low-metallicity galaxies, obtaining their spectra will have to await the advent of 30m-class telescopes.

3.5 Mass-loss rates versus metallicity

In Chapter 2, we reported that the wind momenta of the stars in our sample appear to be higher than theoretically predicted for their metallicity. This trend remains after refitting these stars with the updated GA and including the new targets. This is shown in the updated modified wind momentum versus luminosity diagram (WLD; Figure 3.7). This figure also shows a weighted linear fit to our data ($\log D_{\text{mom}} = a + b \times \log L/L_{\odot}$, with $a = 18.4 \pm 1.9$, $b = 1.86 \pm 0.33$). The fit confirms that the stars exhibit LMC strength winds. Only two stars (IC1613-1 and NGC3109-3) have a best-fit value for their modified wind momentum that is close to SMC values, and none have values indicative of a sub-SMC wind strength.

An important aspect to note when using the WLD to compare mass-loss rates, is that inhomogeneities in the wind (clumping) are not taken into account when deriving the empirical mass-loss rate. This neglect of clumping causes mass-loss rates derived from diagnostic lines sensitive to the density-squared, such as He II $\lambda 4686$ and H α , to be over-estimated (e.g., Puls et al. 2008).

This effect can be seen in Figure 3.7 by comparing the results from Mokiem et al. (2007) to the predictions from Vink et al. (2001). The empirical values for the Galaxy, LMC and SMC are clearly higher than the ones predicted by theory. However, the trend of decreasing wind strength at lower metallicities is in excellent agreement with theory. Thus, for an assumed sub-SMC metallicity we would expect our stars to be located below the empirical SMC values in the WLD.

Lucy (2012) argues that the neglect of wind clumping is the most likely explanation for the high mass-loss rates of these stars. However, we do argue that wind clumping would have to be metallicity dependant to explain our results. An other possibility given by Lucy (2012) is the presence of an additional wind-driving mechanism, possibly only operating in winds that have low terminal wind velocities, or in a restricted part of (T_{eff}, g, Z) -space.

However, an explanation for the high mass-loss rates may be found in the assumed metallicity of the host galaxies. Iron (and iron-like elements) remains the dominant element in driving the wind for metallicities down to $0.1Z_{\odot}$, while α ele-

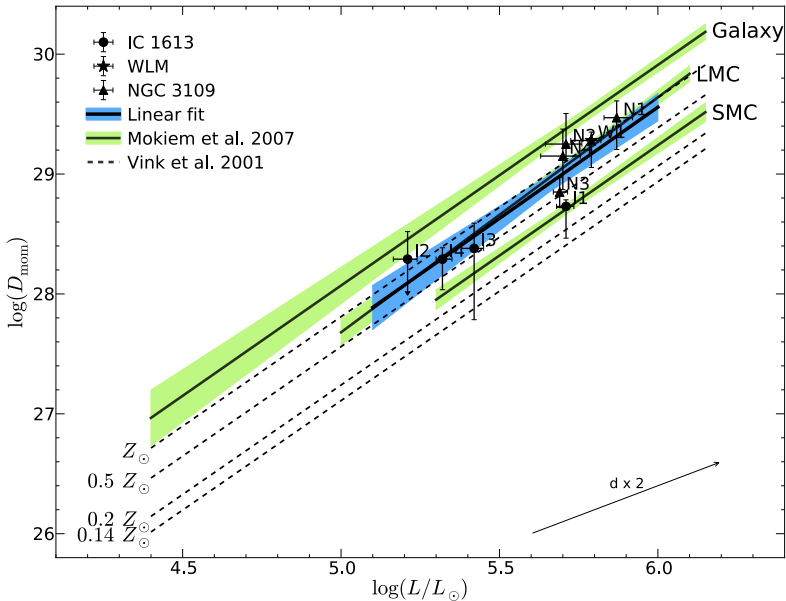


Figure 3.7: Location of the target stars in the modified wind momentum versus luminosity diagram. Also indicated are the theoretical predictions from Vink et al. (2001) and the empirical results from Mokiem et al. (2007). NGC3109-4 is shifted by -0.01 dex in luminosity for clarity. 1σ error bars are indicated. The thick line represents a linear fit to our results, and shows that the wind strengths are comparable to the empirical LMC results.

ments dominate at lower metallicities (Vink et al. 2001). Thus, the iron content of the stars needs to be evaluated to be able to properly compare the wind strengths with theoretical predictions.

While all the host galaxies have very low average stellar iron abundances of $[\text{Fe}/\text{H}] \leq -1.2$ (for an overview, see McConnachie 2012), the metallicity of the young stellar population is likely higher. This metallicity can be constrained indirectly from H II regions and directly from red and blue supergiants. Garcia et al. (2014), Levesque & Massey (2012), and Evans et al. (2007) give overviews of all relevant metallicity measurements of the young stellar population of IC 1613, WLM, and NGC3109, respectively. The metallicity measurements range from $0.05 Z_{\odot}$ to $0.10 Z_{\odot}$ based on the oxygen abundance in H II regions and up to $0.15 Z_{\odot}$ in blue supergiants. However, there are indications that the galaxies have a sub-solar α -to-iron ratio. Below, we give an overview of the stellar iron (or iron-group elements) abundance measurements in the young population of the host galaxies.

Tautvaišienė et al. (2007) derive an iron content of $[\text{Fe}/\text{H}] = -0.67 \pm 0.06$ for three M-type supergiants in IC 1613, or $Z_{\text{IC1613}} = 0.21 Z_{\odot}$ based on iron. Garcia et al. (2014) find qualitative indications that the iron content might be close to the

SMC value.

Venn et al. (2003) report an iron abundance of $[\text{Fe}/\text{H}] = -0.38 \pm 0.29$ for two supergiants in WLM, corresponding to $Z_{\text{WLM}} = 0.42 Z_{\odot}$, but with very large error bars. They derive a stellar oxygen abundance that is five times higher than those found from nebular studies. Conversely, Urbaneja et al. (2008) derive $Z_{\text{WLM}} = 0.13 Z_{\odot}$ based on mainly iron, chromium and titanium in blue supergiants, and find no indication that the α -to-iron ratio is non-solar. In particular, they derive a metallicity of $[Z] = -0.80 \pm 0.20$ for WLM-1 ($0.16 Z_{\odot}$). It therefore seems unlikely that an underestimated iron abundance explains the strong stellar wind of WLM-1.

Hosek et al. (2014) analysed 12 late-B and early-A supergiants in NGC3109, and derive $[Z] = -0.67 + / - 0.13$ based on iron-group elements, or $Z_{\text{NGC3109}} = 0.21 \pm 0.08 Z_{\odot}$. As for IC 1613, this indicates that the iron content is SMC-like. Our results should thus be compared to the SMC predictions.

For our sample of stars, an SMC metallicity would lessen the discrepancy between the observed wind momenta and those predicted from theory. Compared to the SMC predictions, IC1613-1 is in good agreement with the radiation-driven wind theory, while the other three stars in IC1613 have too high best-fit values but agree within error bars. NGC3109-3 has a slightly too high mass-loss rate but is in agreement within errors. For the other three stars in NGC3109 the best-fit wind strengths are comparable to or slightly higher than LMC values, but can just be reconciled with SMC values within errors for two of them. The wind strength of WLM-1 is just in agreement with an SMC metallicity, but as mentioned above, it is unlikely that the metallicity is underestimated for this star.

Considering the sample as a whole, the observed discrepancy with radiation-driven wind theory at low metallicities may be reduced if the metallicity has indeed been underestimated. However, the stars still tend to have too high mass-loss rates, even if their iron content is comparable to SMC stars. For our results to be fully in agreement with the predictions from radiation-driven wind theory, the iron content should be LMC-like, or half solar (see Figure 3.7). A firm determination of the iron content in the host galaxies is needed to be conclusive, and, most importantly, a confirmation of the wind properties from the UV has to be obtained to reduce the uncertainties in the derived wind momenta.

3.6 Evolutionary state

Figure 3.8 shows the position of the full sample of stars in the Hertzsprung-Russell diagram (HRD). Our sample is complete for the O stars listed in Bresolin et al. (2006, 2007), and Evans et al. (2007) above the indicated magnitude cut-off for each galaxy. Garcia & Herrero (2013) identified eight new O-type stars in IC1613, and provided

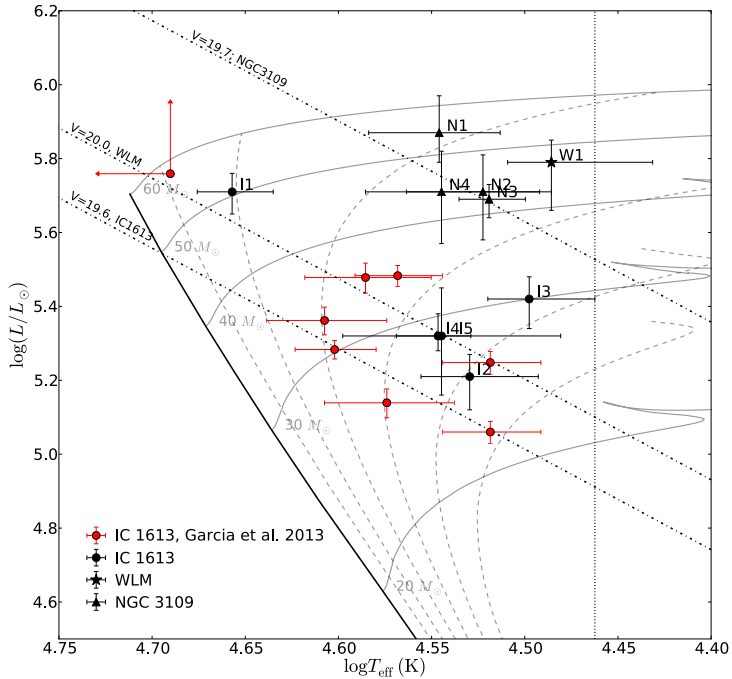


Figure 3.8: Hertzsprung-Russell diagram indicating the location of the target stars. Also plotted are evolutionary tracks from Brott et al. (2011) for SMC metallicity and no initial rotation. The dashed lines indicate isochrones in steps of 1 Myr. The dashed-dotted lines indicate the magnitude cut-offs for the three galaxies, and the dotted vertical line roughly indicates the division between O and B stars. The IC1613 stars from Garcia & Herrero (2013) are plotted in red.

an estimate of their stellar parameters. We also show these stars in Figure 3.8, but note that they are based on observations with a lower resolving power ($R = 1000$). Garcia & Herrero (2013) do not give bolometric luminosities, and the values used in the HRD are based on their temperatures and the bolometric correction from Martins et al. (2005).

The single WLM star in our sample is at the location in the HRD that is expected for its spectral type. It is remarkable that no other O stars are known in WLM that populate the area of the HRD below WLM-1 and above our magnitude cut-off (indicated with the dashed line in Figure 3.8). The only other known O star in WLM is an O7 V((f)) with $V=20.36$ (A15 in Bresolin et al. 2006). This suggests that, while star formation is ongoing in WLM, this mostly happens in low-mass clusters that do not produce many O-type stars.

For NGC 3109, our sample is restricted by the magnitude cut-off. The stars in our sample populate the small area of the HRD that we can observe with X-Shooter, and

thus all have high masses ($M_{\text{ini}} \gtrsim 40M_{\odot}$). They are located in different regions within the host galaxy (see Figure 3.3), suggesting that massive star formation is ongoing in several regions of the galaxy.

The HRD for IC 1613 is well populated by our sample and the stars from Garcia & Herrero (2013). Most of the stars have masses in the range $25M_{\odot} \leq M_{\text{ini}} \leq 35M_{\odot}$, but the two O3 stars indicate that higher mass stars are also being formed. This is further suggested by the presence of the oxygen sequence Wolf-Rayet star in the galaxy (DR1; see, e.g., Kingsburgh & Barlow 1995; Tramper et al. 2013, , Chapter 4). While on large time-scales the star-formation rate has been constant (Skillman et al. 2014), IC 1613 is currently vigorously forming stars, with 164 OB associations identified (Garcia et al. 2009). The location of our sample of stars in IC 1613 follows the main regions of star formation, with the most massive star located in the North-Eastern lobe where star formation is the most prominent.

3.7 Summary

We have presented the results of a quantitative spectroscopic analysis of ten O-type stars located in the Local Group dwarf galaxies IC 1613, WLM and NGC 3109. These galaxies have a sub-SMC metallicity based on their oxygen content.

We derived the wind and atmosphere parameters by adjusting FASTWIND models to the observed line profiles. We derived the fundamental stellar properties (including ages and initial masses) from comparison with evolutionary tracks.

We used our results to investigate the effective temperature versus spectral type calibration at (sub-)SMC metallicity. We presented both weighted and unweighted fits to the giants and supergiants, and find no significant offset between a calibration based on SMC data and one based on the full sample of stars in IC1613, WLM and NGC 3109 within the limits imposed by our data quality.

We discussed the location of the sample stars in the Hertzsprung-Russell diagram. None of our stars have initial masses higher than $\approx 50M_{\odot}$. Two of our stars are helium enriched at their surface, which may be indicative of a binary history.

We presented the modified wind momentum versus luminosity diagram. Instead of (sub-)SMC strengths winds, our results indicate stellar winds reminiscent of an LMC metallicity. We discussed the indications that the iron content of the host galaxies may be higher than initially thought, and is possibly SMC-like. While this would lessen the discrepancy with radiation-driven wind theory, the stellar winds of the stars in our sample remain significantly too strong for their metallicity. UV observations of the stars are needed to firmly constrain the wind properties and investigate the effect of wind clumping and the potential presence of an additional wind driving mechanism.

On the nature of WO stars: a quantitative analysis of the WO3 star DR1 in IC 1613

F. Tramper, G. Gräfener, O.E. Hartoog, H. Sana, A. de Koter, J.S. Vink, L.E.
Ellerbroek, N. Langer, M. Garcia, L. Kaper, S.E. de Mink
Astronomy and Astrophysics, 2013, 559, A72

Abstract

Oxygen sequence Wolf-Rayet (WO) stars are thought to represent the final evolutionary stage of the most massive stars. The characteristic strong O VI emission possibly originates from an enhanced oxygen abundance in the stellar wind. Alternatively, the O VI emission can be caused by the high temperature of these stars, in which case the WO stars are the high-temperature extension of the more common carbon sequence Wolf-Rayet (WC) stars. By constraining the physical properties and evolutionary status of DR1, a WO star in the low-metallicity Local Group dwarf galaxy IC 1613 and one of only two objects of its class known in a SMC-like metallicity environment, we aim to investigate the nature of WO stars and their evolutionary connection with WC stars. We use the non-LTE atmosphere code `CMFGEN` to model the observed spectrum of DR1 and to derive its stellar and wind parameters. We compare our values with other studies of WC and WO stars, as well as with the predictions of evolutionary models. We also model the surrounding nebula using the photo-ionization code `CLOUDY`. The oxygen and carbon abundances that we obtain are comparable to values found for WC stars. The temperature and luminosity are, however, higher than those of WC stars. DR1 is embedded in the hottest known H II region in the Local Group. The nebular properties can be consistently reproduced by `CLOUDY` models adopting DR1 as central ionizing source. Comparison of the abundances and temperature of DR1 with core helium-burning models show that DR1 is currently

well into the second half of helium burning. If the properties of DR1 are representative for the WO class, it would imply that WO stars are the high-temperature and high-luminosity extension of the WC stars, and do not necessarily represent a later evolutionary stage.

4.1 Introduction

The oxygen sequence Wolf-Rayet (WO) stars, introduced by Barlow & Hummer (1982), are extremely rare. Only eight members of this class were known at the time of writing: Sand 4 (WR 102), Sand 5 (WR 142), MS4 (WR 30a) and WR 93b in the Milky Way, Sand 2 (BAT 99-123) and the recently discovered LH41-1042 (Neugent et al. 2012) in the Large Magellanic Cloud (LMC), Sand 1 (Sk 188) in the Small Magellanic Cloud (SMC), and DR1 in IC 1613. Their spectra are characterized by strong emission lines of highly ionized oxygen, in particular the O VI 3811-34 Å line with an equivalent width of up to 1700 Å (Kingsburgh & Barlow 1995).

The origin of the high-excitation oxygen emission is widely attributed to the surfacing of this species during the late stages of core helium (or possibly carbon) burning (Barlow & Hummer 1982; Smith & Maeder 1991). Revealing the core at this late stage of evolution requires the stellar mass-loss rate in prior stages to be relatively low. In this scenario the presence of WO stars is therefore preferred in low-metallicity environments (Smith & Maeder 1991; Georgy et al. 2009), where the radiation-driven winds of their progenitors are relatively weak due to the low metal content (Vink et al. 2001; Vink & de Koter 2005).

Crowther et al. (1998) introduced a quantitative classification scheme for the carbon sequence Wolf-Rayet (WC) and WO stars, in which the WO stars are the high-temperature extension of the WC class. In this classification, the highly ionized oxygen emission is primarily the result of excitation effects, and a significant abundance difference with the WC stars is not necessarily implied.

Wolf-Rayet (WR) stars may be subject to sub-photospheric inflation of their stellar envelopes, resulting in lower stellar temperatures (Gräfener et al. 2012). As this effect is expected to be more pronounced at high metallicity (Ishii et al. 1999), WR stars in low-metallicity environments are expected to have higher stellar temperatures than those in the Galaxy.

WO stars are often thought to represent the final stage in the evolution of stars initially more massive than $25 M_{\odot}$ (Meynet & Maeder 2003), i.e. including very massive stars that may avoid a red supergiant phase. If this is the case, WO stars offer the rare opportunity to study such stars just prior to their supernova (SN) explosions. Moreover, these SNe may be quite exotic, including helium-poor type Ic SNe, hypernovae (e.g., Nomoto et al. 2010), and, if they retain a rapidly rotating core, even gamma-ray bursts (Georgy et al. 2009; Woosley & Bloom 2006; Yoon et al. 2012).

The surface abundances of early WC and WO stars closely reflect the core abundances. Measuring these abundance can thus provide constraints on the controversial $^{12}\text{C}(\alpha, \gamma)^{16}\text{O}$ thermonuclear reaction rate.

In this chapter, we present a quantitative spectroscopic analysis of DR1 that allows us to constrain its physical and wind parameters, to investigate the nature of the

Table 4.1: Journal of observations.

HJD <i>At start of obs.</i>	t_{exp} (s)	R-band Seeing (")
2455857.705	2 x 3600	0.6-0.7
2455858.588	3600	0.8-0.9
2455859.642	1800	0.9

object, and ultimately, its evolutionary stage. Located in the low-metallicity Local Group dwarf galaxy IC 1613, DR1 is one of the two WO stars known in a SMC-like metallicity environment (with $Z_{\text{SMC}} = 1/5 Z_{\odot}$). Metallicity estimates for IC 1613 range from $1/10 Z_{\odot}$ based on oxygen (e.g. Bresolin et al. 2007) to $1/5 Z_{\odot}$ based on iron (Tautvaišienė et al. 2007). DR1 thus offers a unique probe of the final evolutionary stages of massive stars at low metallicity.

The layout of this chapter is as follows. Section 4.2 summarizes previous research on DR1. Section 4.3 describes the observations and data reduction. In Section 4.4 we analyse the stellar and nebular spectra, and in Section 4.5 we discuss DR1’s properties, initial mass, evolutionary history and its eventual fate. Finally, Section 4.6 conveys our conclusions.

4.2 Literature overview

DR1 was discovered in 1982 by D’Odorico & Rosa (1982). Based on spectra in the 4000-7000 Å range, they classified it as a peculiar WC star or a WC + WN binary. In the same year, spectra extending below 3600 Å were obtained by Davidson & Kinman (1982), who suggested that the star could be a member of the WO class because of the presence of strong O VI $\lambda\lambda 3811-34$ emission. Davidson & Kinman (1982) derived a temperature of 100 kK for the star based on the nebular He II $\lambda 4686$ flux and assuming a blackbody distribution for the ionizing radiation. Subsequent studies by Armandroff & Massey (1991) and Garnett et al. (1991) yielded spectral types of WC4-5 and WO4, respectively. The latter authors estimated that the effective temperature T_{eff} should be in the range of 75 kK to 90 kK to reproduce the ionizing flux implied by the nebular H β and He II $\lambda 4686$ lines. Finally, DR1 and its surrounding nebula were intensively studied by Kingsburgh & Barlow (1995), who adopted the spectral type WO3 (Kingsburgh et al. 1995). They derived $T_{\text{eff}} = 75$ kK, a stellar luminosity $L = 10^6 L_{\odot}$, and a terminal wind velocity $v_{\infty} = 2850$ km s $^{-1}$. They reported number abundances of X(C) = 0.47, X(O) = 0.27 and X(He) = 0.25, in agreement with the values that they found for other WO stars (Kingsburgh et al. 1995).

DR1 is the ionizing source of the surrounding H II region S3 (e.g., D’Odorico &

Table 4.2: INT/WFC UBVRI photometry.

Quantity	U	B	V	R	I
m	18.543	19.877	19.857	19.827	19.901
σ_m	0.006	0.006	0.009	0.010	0.015
M	-5.74	-4.41	-4.43	-4.46	-4.38

Notes. Rows one and two provide the apparent magnitude m and its error σ_m . The third row provides the corresponding absolute magnitude M , calculated adopting a distance of 721 kpc.

Rosa 1982), which exhibits unusually strong He II emission. Kingsburgh & Barlow (1995) derived an electron temperature $T_e = 17.1$ kK and an oxygen abundance $12 + \log(\text{O}/\text{H}) = 7.7$, or $Z = 0.1 Z_\odot$ for S3 (with $12 + \log(\text{O}/\text{H})_\odot = 8.69$; Asplund et al. 2009). This makes the surrounding H II region one of the hottest known in the Local Group.

4.3 Observations and data reduction

We have observed DR1 using the X-Shooter spectrograph (Vernet et al. 2011) on ESO's Very Large Telescope (VLT), which covers a wavelength range extending from the near-UV to the near-IR (3 000 - 25 000 Å). The observations were carried out in October 2011 during dark time, as part of the NOVA program for X-Shooter guaranteed time. A total of 3.5 hours of integration on target has been obtained over three consecutive nights (see Table 4.1).

The selected slit widths of 0.8", 0.9" and 0.9" result in a spectral resolving power of 6200, 8800, 5300 in the UVB, VIS and NIR instrument arms, respectively. For the NIR, a K-band blocking filter has been used to avoid reflection of both sky background and object photons from this band into the 10 000 - 20 000 Å region, optimizing the signal-to-noise ratio in the latter wavelength range.

To correct for instrument flexures, calibration frames have been taken before the start of each observation and after one hour of observations at the first night. Spectrophotometric standard stars have been observed at the beginning of each night to allow relative flux calibration.

The data have been reduced using the X-Shooter instrument pipeline version 1.3.7 (Modigliani et al. 2010). The extracted spectra were binned to 0.2 Å in the UVB and VIS arms, and 0.6 Å in the NIR arm. The (relative) flux-calibrated spectra for each observing block were co-added to obtain the final relative flux-calibrated spectrum.

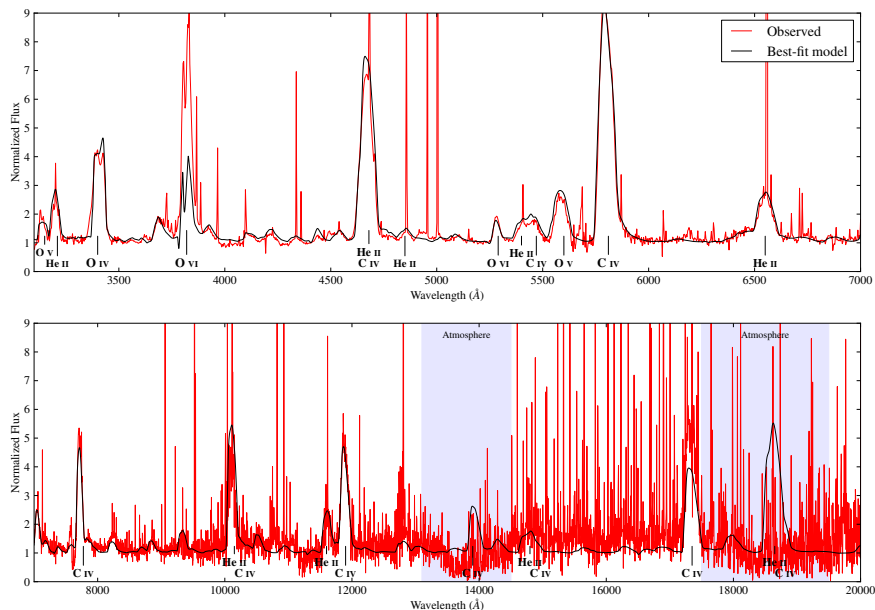


Figure 4.1: Optical/near-infrared spectrum of DR1 (red). The best-fitting model spectrum is shown in black. As discussed in the text, the $O\text{ VI } \lambda\lambda 3811\text{-}34$ emission is underpredicted by the model. The shaded areas indicate the regions where the atmosphere of the Earth is opaque.

4.3.1 Photometry

The UBVRI magnitudes of the target (Table 4.2) were taken from the catalog of IC 1613's stellar population by Garcia et al. (2009). This catalog was built from PSF-photometry on multiple, dithered images of the irregular dwarf galaxy, taken with the Wide-Field Camera (WFC) at the 2.5m Isaac Newton Telescope (INT). The set of broad-band filters used, Harris-BVR and RGO-IU, are similar to the Johnson's UBVRI system. The apparent and absolute magnitudes of DR1 are presented in Table 4.2. The latter were computed adopting a foreground reddening of $E(B - V) = 0.025$ (Schlegel et al. 1998) and a distance of 721 kpc (Pietrzyński et al. 2006).

4.4 Quantitative spectroscopic analysis

4.4.1 Stellar spectrum

We model the stellar spectrum of DR1 using the atmosphere code `CMFGEN` (Hillier & Miller 1998). This code assumes a radial outflow of material from the atmosphere, of which the density and velocity structure is prescribed. The gas is assumed to be

Table 4.3: Mass fractions of the elements in the model.

Element	Mass fraction
Neon	1.74×10^{-3}
Silicon	6.99×10^{-5}
Phosphorus	6.12×10^{-7}
Sulfar	3.82×10^{-5}
Chorine	7.87×10^{-7}
Argon	1.02×10^{-5}
Calcium	6.44×10^{-6}
Chromium	1.70×10^{-6}
Manganese	9.44×10^{-7}
Iron	1.36×10^{-4}
Nickel	7.32×10^{-6}

in a state of non-local thermodynamic equilibrium (non-LTE). The atomic models include both explicit levels and super-levels, and are of such complexity that effects such as back-warming and line-blanketing are self-consistently treated. Convergence to a solution that fulfills radiative equilibrium can not be achieved by starting from a simple (e.g. grey LTE) solution and setting up a grid scanning the appropriate part of parameter space. Instead it requires one to migrate through a series of educated steps in specific parameters, from an existing model with fairly similar parameters to the final model.

This fitting procedure prevents a systematic search of parameter space and complicates an assessment of the uncertainties in the parameters of the final model. Furthermore, no specific diagnostic reacts exclusively to a given parameter, safe for luminosity which is determined from photometry. We therefore only specify error bars for this parameter. For the other parameters we give an indication of the accuracy of the obtained value. The steps taken to arrive at the final model are discussed below.

In our atmosphere models, the abundances of all modeled elements except hydrogen, helium, carbon, oxygen and neon are set to a value of 10% of solar (Table 4.3). The neon abundance is enhanced by the conversion of nitrogen into ^{22}Ne at the beginning of helium burning. The enhancement is predicted to be 1.4 times the initial oxygen mass fraction (Maeder 1983). For an oxygen abundance of 1/10 solar, this results in a neon mass fraction very close to the solar value, which we therefore adopt. The hydrogen abundance is set to zero. The abundances of carbon and oxygen are being fitted and are not listed in Table 4.3. A summary of the ionization stages of each element included in the model is given in Appendix B.3.

Although we set the metallicity of our models to $1/10 Z_{\odot}$, which is the metallicity based on the oxygen abundance (e.g., Kingsburgh & Barlow 1995; Bresolin et al. 2007), there are indications that IC 1613 may have a non-solar abundance pattern.

Table 4.4: Best-fit parameters and ionizing fluxes.

Parameter	Value
v_∞	2750 km s ⁻¹
β	2.0
f_c	0.1
T_*	150 kK
[C/He]	0.35
[O/He]	0.06
$\dot{M}f_c^{-0.5}$	$5.6 \times 10^{-5} M_\odot \text{ yr}^{-1}$
$\log(L/L_\odot)$	5.68 ± 0.10
$\log(Q_0)$	49.5 s^{-1}
$\log(Q_1)$	49.3 s^{-1}
$\log(Q_2)$	48.0 s^{-1}

Notes. Q_0 , Q_1 and Q_2 are the number of ionizing photons per second for hydrogen, He I and He II, respectively. Except for the luminosity, the determination of formal error bars is not possible. Uncertainties on the parameters are discussed in the text.

Tautvaišienė et al. (2007) derived an iron abundance of $\log([\text{Fe}/\text{H}]) \approx -0.7$ from the analysis of three M-type supergiants, i.e. very close to the SMC iron abundance. As iron is an important driver of WR winds, we also ran a model with $Z = 1/5 Z_\odot$ to assess the impact of a higher metallicity on the derived parameters (Section 4.4.1).

We estimate the reddening of the DR1 source to be $E(B - V) = 0.05$ by adopting the extinction law of Fitzpatrick (1999) and dereddening the flux-calibrated spectrum to the slope of our model continuum. We normalize the dereddened spectrum by dividing by the model continuum, and setting the flux equal to unity at 6000 Å. The normalized spectrum does not show a noticeable slope, implying that the adopted value for the reddening is satisfactory. The best-fitting spectrum is presented in Figure 4.1, and its parameters are listed in Table 4.4.

Wind parameters: terminal velocity, β and clumping

In WR spectra, the full-width at half-maximum (FWHM) of the spectral lines represents the terminal velocity of the wind (v_∞), and this parameter can therefore easily be constrained. The best-fitting value is $v_\infty = 2750 \text{ km s}^{-1}$, and is accurate to within 50 km s⁻¹.

The wind acceleration is assumed to be described by a single- β velocity law, i.e.

$$v(r) = v_\infty \left(1 - \frac{R_*}{r}\right)^\beta. \quad (4.1)$$

The value of β influences the strength of the mass-loss sensitive lines (mainly O IV $\lambda 3300$ and C IV $\lambda 5800$), and is therefore degenerate with the wind strength for these

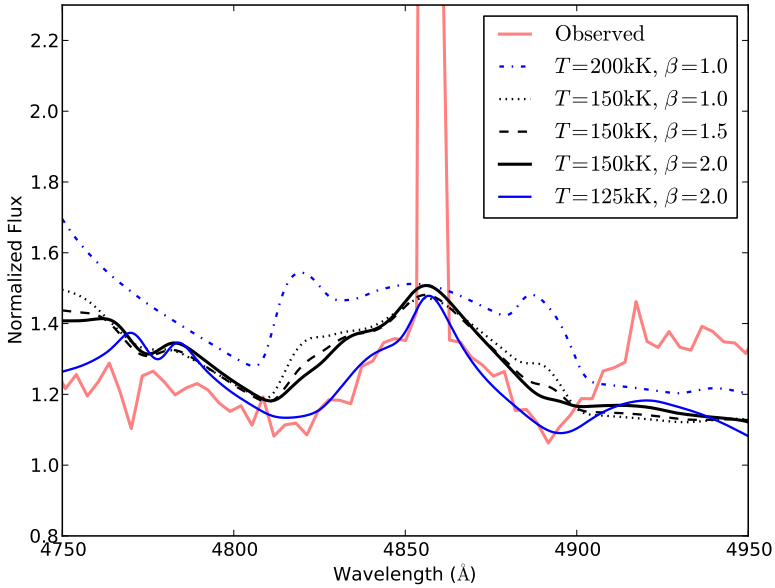


Figure 4.2: Behavior of the He II line at 4859 Å for different values of the temperature and β .

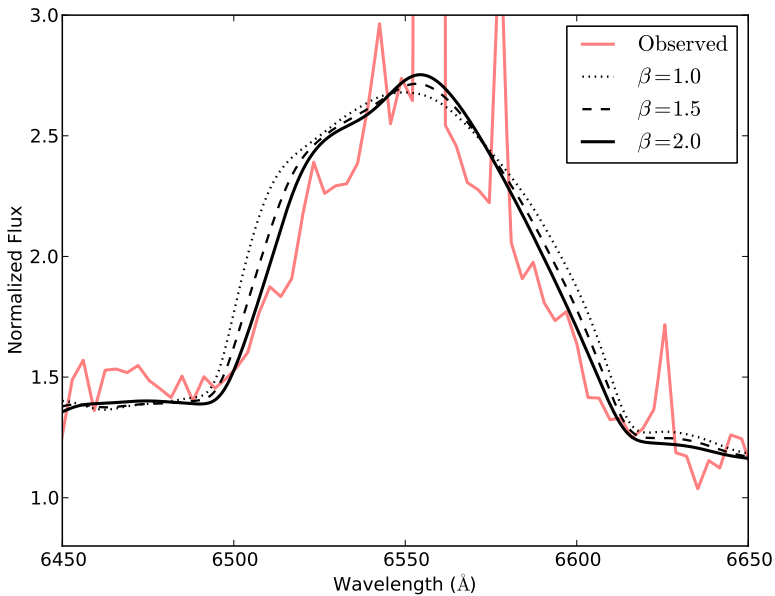


Figure 4.3: Behavior of the He II $\lambda 6560$ line for different values of β .

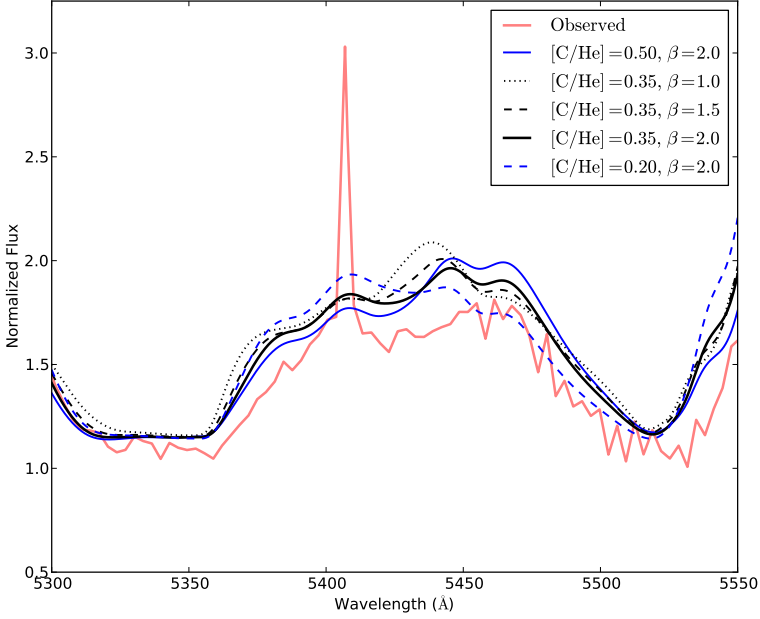


Figure 4.4: Behavior of the He II and C IV line complex around 5400 Å for different values of β and carbon abundance.

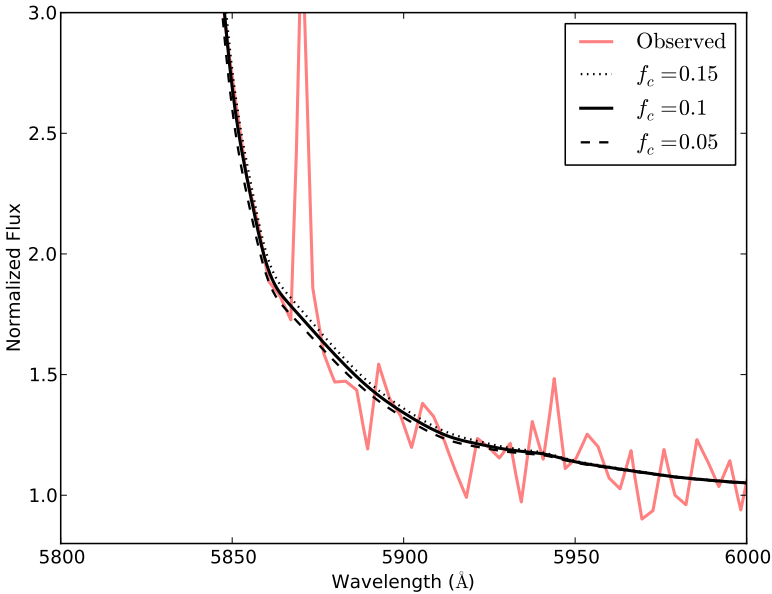


Figure 4.5: Influence of the volume filling factor on the electron scattering wing of C IV $\lambda\lambda$ 5801-12.

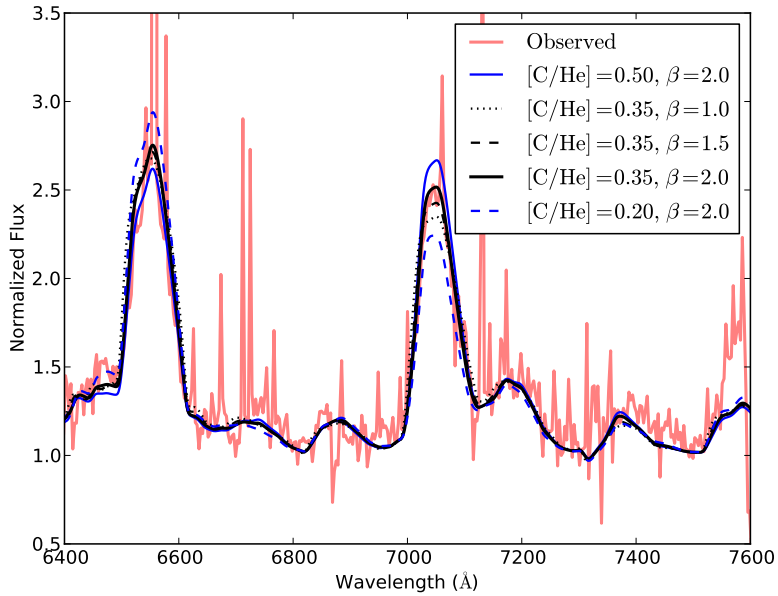


Figure 4.6: Behavior of the He II $\lambda 6560$ and C IV $\lambda 7063$ lines for different values of β and carbon abundance.

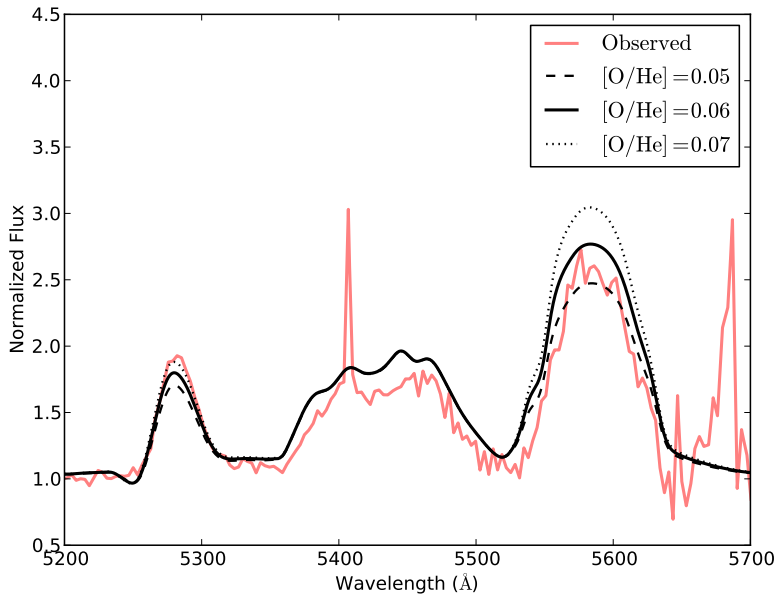


Figure 4.7: Behavior of the O VI $\lambda 5290$ and O V $\lambda 5598$ lines for different values of the oxygen abundance.

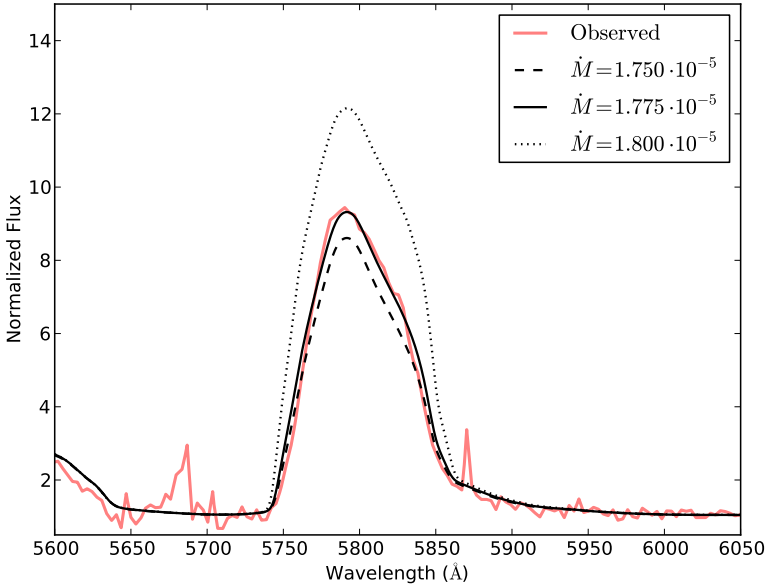


Figure 4.8: Behavior of the C IV line at $\lambda\lambda 5801-12$ for different values of \dot{M} .

lines. However, the value of β also influences the shape of the optically thin He II lines formed at a larger radius. For low values of β (i.e., high wind acceleration), the velocity gradient in the outer parts of the wind where these lines are formed is small, as the wind has already approached v_∞ . This causes flat-topped line profiles. For higher values of β , the wind is still accelerating towards v_∞ , and the velocity gradient at the line-forming region is larger, causing the line profiles to be more triangular-shaped (see Figure 4.2). This diagnostic is somewhat degenerate with temperature (see Section 4.4.1), which affects the region of the wind in which these lines are formed. For higher temperatures the lines are formed further out in the wind where the velocity gradient again is smaller, thus producing flat-topped line profiles.

The shape of the He II and C IV line complex around 5400 \AA is affected by the adopted value of β . This line complex is also used to constrain the carbon abundance (see Section 4.4.1). The model has thus been iterated for different values of β , temperature and carbon abundance.

The shape of the line profiles of He II $\lambda 4859$ and He II $\lambda 6560$, as well as the shape of the He II and C IV complex at 5400 \AA have been used to determine the best-fit value for β . Figures 4.2 to 4.4 show the behavior of these lines for different sets of parameters. The parameters that are not explicitly specified in these plots are conform

to the numbers given in Table 4.4. All diagnostics point toward a high value of $\beta = 2$, i.e. a slowly accelerating wind, but lower values of β are not excluded. A high value of β (1.5 - 2) is consistent with theoretical predictions for optically thick stellar winds (Vink et al. 2011).

The value of the volume filling factor (f_c) influences the shape of the electron-scattering wings of the strong lines (see Figure 4.5), although the effect is weak. The commonly adopted value of $f_c = 0.1$ is in agreement with the observed spectrum, but cannot be well constrained. However, very weak clumping ($f_c \geq 0.5$) can be excluded, as O VI $\lambda 5290$ then gets reabsorbed in the wind and can no longer be fitted. Further constraints on the clumping are discussed in Section 4.5.2.

Temperature

Because the stellar wind is optically thick, we do not define the effective temperature at a Rosseland optical depth of $\tau_R = 2/3$, as the corresponding radius is located far out in the wind. Instead, we define T_* to represent the effective temperature at the base of the wind (approximately $\tau_R = 20$). This allows for a more meaningful comparison to evolutionary tracks, where the adopted effective temperature is not corrected for the presence of a wind.

Models have been calculated for temperatures T_* ranging between 125 kK and 200 kK. The line ratios of the different ionization stages of carbon and oxygen do not change significantly in most of the temperature range, and thus cannot be used to constrain the temperature. The presence of the strong O VI $\lambda\lambda 3811-34$ emission can be seen as an indication of a high temperature, although the full strength of the line cannot be reproduced. However, the line shapes of the optically thin He II lines are inconsistent with a very high temperature (see Figure 4.2), as the model line profiles for these temperatures show a flat-topped shape, while the observed lines are triangular shaped (see Section 4.4.1).

A temperature of 150 kK produces the best-fitting model to all lines except O VI $\lambda\lambda 3811-34$. The underpredicted flux in this line will be further discussed in Section 4.5.1. Although a lower temperature (125 kK) provides an even better fit to the He II lines (see Figure 4.2), the line ratio of O VI $\lambda 5290$ to O V $\lambda 5598$ changes significantly for this temperature, with too much emission in the O V line compared to O VI. We therefore adopt 150 kK as best-fit value. Models with a temperature $T_* > 175$ kK are excluded based on the He II line shapes (see Figure 4.2).

Carbon and oxygen abundances

The carbon abundance (modeled as [C/He] by number), has been determined using the He II $\lambda 5412$ and C IV $\lambda 5471$ line ratio. As can be seen from Figure 4.4, this

diagnostic is not very sensitive to the adopted value of $\beta = 2$. For this β , changes in the C IV peak are minimal for different values of the carbon abundance; a value of $[\text{C}/\text{He}] = 0.35$ agrees best with the overall spectrum (see Figure 4.6 for the typical behavior of the carbon and helium lines for different carbon abundances).

The oxygen abundance ($[\text{O}/\text{He}]$ by number) can be constrained with an accuracy of 0.01 by the strength of the O VI $\lambda 5290$ and O V $\lambda 5598$ lines (see Figure 4.7). We derive a value of $[\text{O}/\text{He}] = 0.06$ as best-fitting abundance.

Mass-loss rate

The strength of the C IV $\lambda\lambda 5801-12$ and O IV $\lambda\lambda 3404-12$ lines are very sensitive to the mass-loss rate, and therefore these lines serve as the prime diagnostic for this parameter. In general, the equivalent width of WR emission lines is found to be invariant if the transformed radius

$$R_t = R_* \left[\frac{v_\infty}{2500 \text{ km s}^{-1}} / \frac{\dot{M}}{\sqrt{f_c} 10^{-4} M_\odot \text{ yr}^{-1}} \right]^{\frac{2}{3}} \quad (4.2)$$

is kept fixed (Schmutz et al. 1989). The derived mass-loss rate is therefore dependent on the adopted v_∞ , f_c , L and T_* (the last two values determining R_*).

For the parameters of our best-fitting model the mass-loss rate is $\dot{M} = 1.8 \times 10^{-5} M_\odot \text{ yr}^{-1}$, and can be constrained to within 0.05 dex (see Figure 4.8). The corresponding transformed radius is $R_t = 1.3 R_\odot$.

Luminosity

To determine the luminosity of DR1, we have computed synthetic UVRI magnitudes of a fitted model spectrum (with $L = 3 \times 10^5 L_\odot$) by integrating the model flux using the transmission functions of the filters as provided by the INT website¹. Zero-point magnitudes were determined by performing spectrophotometry on a Kurucz model spectrum (Castelli & Kurucz 2004) of Vega ($T_{\text{eff}} = 9500 \text{ K}$, $\log g = 4.0$, $d = 7.68 \text{ pc}$, $R = 2.5 R_\odot$). A reddening of $E(B - V) = 0.05$ (Section 4.4.1) is then added to the obtained values. Because the O VI $\lambda\lambda 3811 - 34$ emission is underpredicted by the model, we do not use the B-band magnitude, which is affected by the flux in this line. Scaling the synthetic magnitudes to match the observed values (Table 4.2) yields a luminosity of $\log(L/L_\odot) = 5.68 \pm 0.10$. The error in this value is based on the spread in magnitude differences for each filter. The error induced by the uncertainty in the distance to IC 1613 (3%; Pietrzyński et al. 2006) is in comparison negligible. Note that the luminosity is overpredicted if undetected companion stars are contributing to

¹<http://catserver.ing.iac.es/filter/list.php?instrument=WFC>

the observed flux. After determining the luminosity, the mass-loss rate is adjusted to fit the observed line strengths.

Metallicity

To determine the impact of the uncertainty in the metallicity of DR1, we computed a model with SMC metallicity ($Z = 1/5 Z_{\odot}$). Apart from the mass-loss rate, the derived parameters are not noticeably affected by this change. The mass-loss rate needed to fit the spectrum is slightly lower than the value derived for the low-metallicity model ($\dot{M}f_c^{-1/2} = 5.1 \times 10^{-5} M_{\odot} \text{yr}^{-1}$, corresponding to $\dot{M} = 1.6 \times 10^{-5} M_{\odot} \text{yr}^{-1}$ for $f_c = 0.1$). This is likely the result of more efficient line blanketing in the high-metallicity model.

4.4.2 Nebular spectrum

DR1 is surrounded by the ionized nebula S3. The narrow nebular emission lines are clearly distinguishable from the Wolf-Rayet spectrum (e.g., Figure 4.1). Apart from the lines usually seen in H II regions, S3 exhibits strong He II emission ($\text{He II } \lambda 4686 / \text{H}\beta = 0.51 \pm 0.03$), indicative of a hot ionizing source. The line strengths from a selection of emission lines relative to H β are given in Table 4.5. The errors on the values have been calculated by the method described in Hartoog et al. (2012). Based on the X-Shooter acquisition image (Figure 1.5), we estimate the projected dimensions of the asymmetric nebula to be approximately 30×60 pc.

Following Pagel et al. (1992), we derive an electron temperature $T_e = 17.5 \pm 0.6$ kK based on the nebular [O III] emission. This temperature is higher than measured in other H II regions with He II emission, making S3 the hottest H II region currently known in the Local Group (see Kehrig et al. 2011, for an overview of known He II nebulae). This electron temperature is indicative for both the high temperature of the ionizing source, and the low-metallicity environment.

The oxygen abundance derived from the [O II] and [O III] emission lines is $12 + \log(\text{O}/\text{H}) = 7.56 \pm 0.11$. The electron density in the nebula is in the low density regime ($< 75 \text{ cm}^{-3}$) based on the [O II] $\lambda 3729/3726$ and [S II] $\lambda 6716/6731$ line ratios (Osterbrock & Ferland 2006).

Assuming that DR1 is the dominant ionizing source of S3, we aim to reproduce the observed nebular properties using the photo-ionization code CLOUDY v8.0 (Ferland et al. 2013). To do this, we model the H II region as a spherically symmetric cloud surrounding an ionizing source, for which we use the best-fit model of DR1. We derive nebular line strengths by computing the nebular spectrum in the line of sight towards the central source. In our models, the metal abundances in the cloud are set

to 18 % of the abundance pattern in the Orion nebula², corresponding to $Z = 0.15 Z_{\odot}$ based on oxygen. The Galactic foreground extinction is discussed in Section 4.3.1. There is no indication that the line of sight towards DR1 suffers from extinction in IC 1613. We therefore do not include dust grains in our model. The inner radius of the cloud r_0 is fixed to 0.1 pc, as varying this inner radius for reasonable values ($r_0 \leq 1$ pc) does not change the resulting parameters significantly.

We assume the following density profile, containing both a r^{-2} dependency and a constant component n_c :

$$n(r) = n_0 \left(1 + \frac{r - r_0}{r_{\text{scale}}} \right)^{-2} + n_c, \quad (4.3)$$

where $n(0) + n_c$ is the density at r_0 and r_{scale} is the scale-length. We compute a grid of models varying n_0 , r_{scale} , and n_c . The line ratios of our best model are given in Table 4.5, and agree well with the observed values.

The adopted model has $n_0 = 35 \text{ cm}^{-3}$, $r_{\text{scale}} = 16$ pc, and $n_c = 8 \text{ cm}^{-3}$, although small variations in these parameters also give nebular properties that match the observed values. However, models with a constant density profile (i.e. $n_0 = 0$), as well as models with $r_{\text{scale}} < 5$ pc, cannot reproduce the observed properties.

These line ratios in Table 4.5 correspond to an electron temperature $T_e = 16.1$ kK and an oxygen abundance of $12 + \log(\text{O}/\text{H}) = 7.61$. This abundance is consistent with the observed value, and would correspond to a metallicity of $Z \approx 0.08 Z_{\odot}$ based on [O II] and [O III]. As the oxygen abundance in our model is set to a value of 15% solar, this indicates that approximately half of the oxygen is in an ionization state higher than O III. This is confirmed by the inspection of the relative population of the oxygen ionization stages in our model. Finally, the Strömgren radius of the modeled H II region is 15 pc, in agreement with the size of the observed nebula. The electron temperature is lower than observed, which is the case for all models that reproduce the line ratios well. This is likely caused by the assumed abundance pattern of the metals, which is observed to differ between individual H II regions (e.g., Zaritsky et al. 1994).

We also investigate the sensitivity of the nebular spectrum to changes in the stellar temperature, the parameter that mostly controls the production of ionizing photons. This sensitivity turns out to be very modest. Nebular models where we varied the temperature of the ionizing source by $\Delta T_* = 25$ kK can also reproduce the observed nebular properties. The results of both the nebular and stellar analysis provide a consistent picture, suggesting that DR1 is indeed the main ionizing source of S3.

²The Orion nebula abundances used in CLOUDY are a subjective mean of values derived by Baldwin et al. (1991), Rubin et al. (1991), Osterbrock et al. (1992) and Rubin et al. (1993).

Table 4.5: Nebular line ratios relative to $H\beta$.

Line ID $\lambda(\text{\AA})$	Observed	Cloudy model
He II		
4686	0.51 ± 0.03	0.53
He I		
4471	0.017 ± 0.007	0.022
5876	0.058 ± 0.014	0.058
6678	0.017 ± 0.007	0.016
[O II]		
3726	0.12 ± 0.03	0.11
3729	0.18 ± 0.04	0.16
[O III]		
4363	0.13 ± 0.01	0.10
4959	1.45 ± 0.07	1.39
5007	4.36 ± 0.18	4.20
[Ne III]		
3869	0.63 ± 0.06	0.40
3968	0.19 ± 0.08	0.12
[Ar IV]		
4711	0.061 ± 0.011	0.058
4740	0.053 ± 0.019	0.045
[S II]		
6716	0.052 ± 0.020	0.028
6731	0.038 ± 0.016	0.020
[S III]		
6312	0.024 ± 0.017	0.008

4.5 Discussion

4.5.1 Oxygen abundance and temperature

The prominent $O\text{ VI } \lambda\lambda 3811\text{-}34$ emission is the tell-tale signature of WO stars. However, this line is notoriously difficult to reproduce by models of their atmospheres. Two modeling approaches can be followed. Either the focus is to reproduce the prominent $O\text{ VI } \lambda\lambda 3811\text{-}34$ emission while accepting a poorer fit to the overall spectrum, or the aim is to reproduce the entirety of the spectrum, accepting a relatively poor fit to $O\text{ VI } \lambda\lambda 3811\text{-}34$.

The modeling of the galactic WO stars WR102 and WR142 (both with spectral type WO2) by Sander et al. (2012) focusses on reproducing the $O\text{ VI } \lambda\lambda 3811\text{-}34$ emission. This can be achieved by adopting a high temperature and an oxygen abundance twice as high as they on average find for early-type WC stars. However, the model spectrum underestimates the flux in some of the other lines seen in the observed

Table 4.6: Comparison of carbon and oxygen abundances measured in WC and WO stars.

Reference	Galaxy	Spectral type	Mass fraction		Number abundance	
			C	O	C/He	O/He
This work	IC 1613	WO3	0.46	0.10	0.35	0.06
Gräfener et al. (1998)	LMC	six WC4	0.4	0.1-0.3		
Crowther et al. (2000)	LMC	WO			0.7	0.15
Crowther et al. (2002)	LMC	six WC4	0.2-0.4	0.1	0.1-0.35	≤ 0.06
Hillier & Miller (1999)	MW	WC5			0.4	0.1
De Marco et al. (2000)	MW	WC8			0.15	0.03
Dessart et al. (2000)	MW	four WC			0.08-0.25	0.02-0.1
Gräfener et al. (2002)	MW	WC5	0.45	0.04		
Crowther et al. (2006)	MW	WC9			0.2	0.01
Smartt et al. (2001)	M31	WC6			0.1	

spectrum, such as the O v $\lambda 5598$ emission. This is likely due to the high adopted temperature, which causes the higher ionization states to be preferred.

Crowther et al. (2000) modeled the far-UV and optical spectrum of the LMC WO star Sand 2 taking the alternative approach, and in their model do not reproduce the O vi $\lambda\lambda 3811-34$ emission. Their obtained temperature is 50 kK lower than temperatures obtained by Sander et al. (2012) who primarily modelled O vi $\lambda\lambda 3811-34$, although the difference can also be attributed to the difference in spectral type.

As our data cover a large wavelength range (3000-20000 Å), we focus on obtaining a good overall fit while neglecting the O vi $\lambda\lambda 3811-34$ line. Although the strong O vi $\lambda\lambda 3811-34$ emission is underpredicted by a factor 2-3, the strength of the O vi $\lambda 5290$ line is well represented by our models. This suggests the presence of an additional mechanism not accounted for in the modeling, which significantly contributes to the O vi $\lambda\lambda 3811-34$ emission.

The O vi $\lambda\lambda 3811-34$ emission is particularly sensitive to temperature, oxygen abundance and wind strength. A higher temperature will increase the O vi to O v ionization ratio, producing stronger emission in O vi. A higher oxygen abundance will increase the strength of oxygen lines relative to that of lines of other elements. The dependence of the strength of O vi $\lambda\lambda 3811-34$ on the mass-loss rate is more subtle: as the O vi $\lambda\lambda 3811-34$ emission is formed in deep layers of the stellar wind, part of the emission is absorbed by the outer layers of the wind itself. A higher mass-loss rate, i.e. a denser wind, will therefore result in weaker observed emission of this line.

A physical motivation for the poor modeling of the O vi $\lambda\lambda 3811-34$ line may be found in its susceptibility to soft X-ray emission at the base of the outflow, e.g. due to shocks in the wind-acceleration zone. Such shocks could pump the upper level through the $2p^2p^0 - 3s^2s$ transition at 184 Å. If the X-ray production is quite localized

at the base of the wind, the layers above this zone may shield (part of) this X-ray emission. This prevents the C IV $\lambda\lambda 5801-12$ line, which originates from the same electron configuration transition as O VI $\lambda\lambda 3811-34$ but is formed further out in the wind, to react in a similar way.

Neglecting the O VI $\lambda\lambda 3811-34$ line, the carbon and oxygen abundances that we obtain are comparable to values found for early-type WC stars in a variety of environments (see Table 4.6). We thus conclude that the carbon and oxygen abundance in DR1 present no indication of enhancement compared to WC stars.

4.5.2 Evolutionary state

As most massive stars are formed in close binary systems (Sana et al. 2012, 2013), it is possible that DR1 has or has had a close companion star. If DR1 is part of a close binary, it is likely that mass transfer between the stars occurs at some point during the evolution of the system, influencing their evolution. For instance, if DR1 has transferred mass onto a companion star, less mass loss through a stellar wind is needed to expose the helium-burning products. Vice versa, if DR1 has gained mass or is the product of a merger, this will likely have led to high rotation rates (e.g., de Mink et al. 2013). This may lead to enhanced mass-loss due to rotation and rotational mixing, also making it easier for the helium-burning products to surface. Because we have no indication for binarity of DR1, we limit the discussion of its evolutionary state to a single-star perspective. However, we cannot exclude the possibility that DR1 is the product of binary interaction.

Figures 4.9 and 4.10 show the position of DR1 in the Hertzsprung-Russell diagram (HRD). For comparison, the two Galactic WO stars and the WC stars analyzed by Sander et al. (2012), and the WO star analysed by Crowther et al. (2000) are also plotted. Both DR1 and the two WO2 stars from Sander et al. (2012) are positioned at the high temperature and high luminosity regime of the strip in the HRD occupied by the WC and WO stars. The LMC WO3 star Sand 2 from Crowther et al. (2000, for which the luminosity is much less uncertain than the Galactic cases due to the better constrained distance) is considerably less luminous, while having the same temperature as DR1. Both DR1 and Sand 2 are located very close to the helium ZAMS, indicating that they could be the descendants of stars with a different initial mass. Alternatively, it is possible that the luminosity of DR1 is overestimated if unseen companions contribute significantly to the observed flux.

Figures 4.9 and 4.10 also show the evolutionary tracks from Meynet & Maeder (2005) and Ekström et al. (2012), representing single stars with SMC metallicity initially rotating at 300 km s^{-1} and single stars with Galactic metallicity initially rotating at 40% of critical, respectively. Figure 4.9 shows that DR1 is located at a position in the HRD that is coinciding with the track for the late stages of evolution of a 120

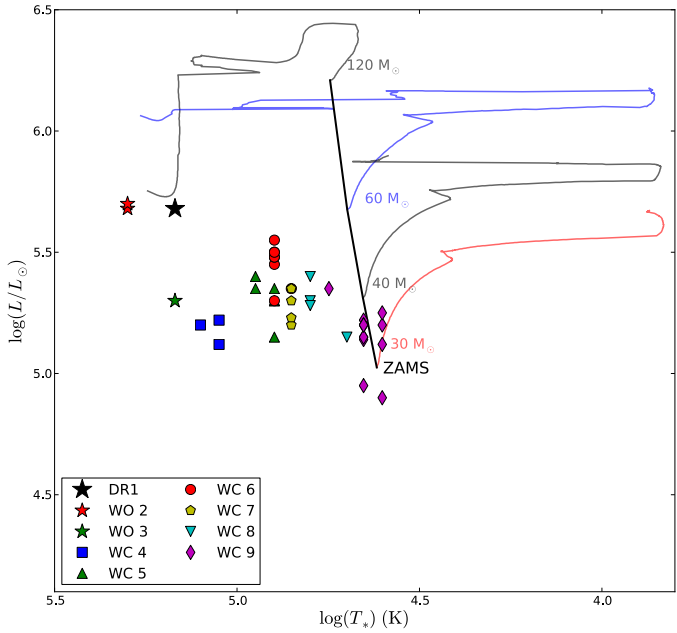


Figure 4.9: Location of DR1 in the Hertzsprung-Russell Diagram. Also plotted are the WO2 and WC stars analyzed by Sander et al. (2012), the LMC WO3 star analysed by Crowther et al. (2000) and evolutionary tracks for SMC metallicity from Meynet & Maeder (2005) for an initial rotation rate of 300 km s^{-1} .

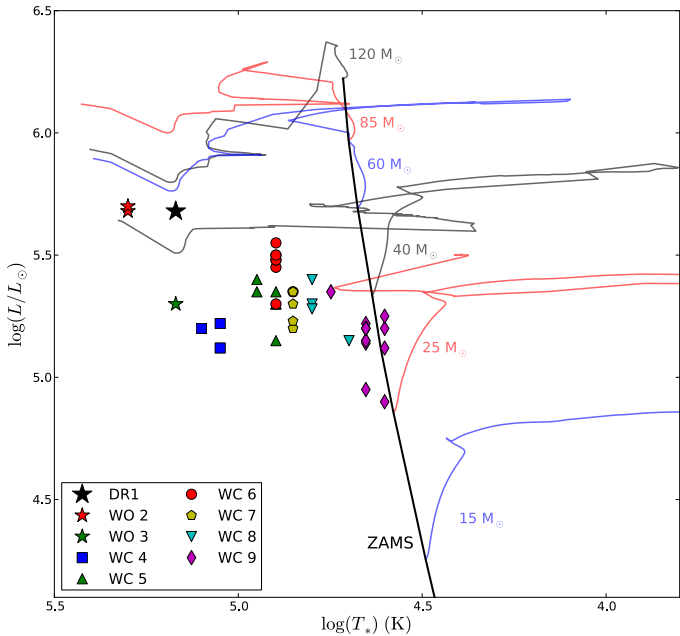


Figure 4.10: Same as Figure 4.9, but with evolutionary tracks for Galactic metallicity from Ekström et al. (2012) for an initial rotation rate of $0.4 v_{\text{crit}}$.

M_{\odot} star at SMC metallicity. The corresponding current-day mass would be $\approx 18 M_{\odot}$. This is consistent with the mass of $20 M_{\odot}$ that is computed from the mass-luminosity relation of Gräfener et al. (2011). A firm determination of the initial mass of DR1 cannot be made, however, as the track for stars with initial masses higher than $60 M_{\odot}$ also reaches the high-temperature domain of the HRD. Uncertainties that may complicate an identification of the evolutionary stage of DR1 from these tracks include the initial rotational velocity, metal content and the mass-loss properties throughout the different evolutionary phases (in particular during the luminous blue variable and red supergiant phases). In general, it is thought that higher rotation rates lead to a higher mass-loss rate, and therefore to lower stellar masses during the WC or WO stage. In specific cases, however, this trend may be broken (see Meynet & Maeder 2003).

For a Galactic environment, Figure 4.10 shows that evolutionary tracks for initial masses higher than $40 M_{\odot}$ reach the high-temperature domain of the HRD where the WO stars are located. Although suffering from the same uncertainties as listed above, it suggests that the occurrence of WO stars is slightly favored at higher metallicities, as the mass range for potential progenitors is larger. This is in contrast with predictions based on the assumption that the oxygen abundance is enhanced in WO stars, in which case their formation is favored in sub-Galactic metallicity environments (see, e.g., Georgy et al. 2009, their Figure 1).

Figure 4.11 compares the carbon and oxygen abundances of DR1 to evolutionary predictions of the change of the helium, carbon and oxygen abundances during core-helium burning. While low-metallicity models have been used for this comparison, the influence of the metallicity is negligible. Higher masses, however, lead to a markedly lower carbon abundance and correspondingly higher oxygen abundance at a given helium mass fraction. Note that only two of the three abundances are independent, as the sum of all three is very close to one.

The $^{12}\text{C}(\alpha, \gamma)^{16}\text{O}$ thermonuclear reaction rate used in these models is still highly uncertain (Tur et al. 2007). For instance, a higher $^{12}\text{C}(\alpha, \gamma)^{16}\text{O}$ cross section would lead to somewhat lower carbon abundances at a given helium mass fraction. The reaction rate employed in the models shown in Figure 4.11 is the one proposed by Weaver & Woosley (1993), which appears to be required for massive stars to reproduce the Solar abundance pattern between oxygen and calcium. If this rate is correct, Figure 4.11 indicates that DR1 is likely not the descendant of a star of initially several $100 M_{\odot}$.

From Figure 4.11, we also see that the surface composition of DR1 corresponds to material that was in the core of the star roughly half-way into core-helium burning. This implies that DR1 must indeed be well advanced in its core-helium burning stage. Assuming a current mass of $20 M_{\odot}$, the radiative envelope is expected to be $\approx 4.7 M_{\odot}$

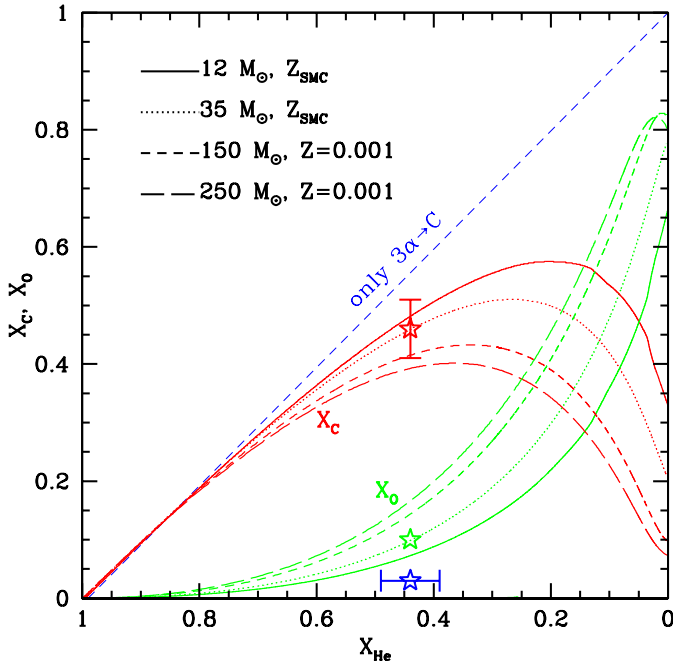


Figure 4.11: Comparison of the helium (blue), carbon (red) and oxygen (green) mass fractions of DR1 with evolutionary predictions of helium-burning stars of various masses ($12 M_{\odot}$ and $35 M_{\odot}$ from Brott et al. (2011), $150 M_{\odot}$ and $250 M_{\odot}$ from Langer et al. (2007)). The uncertainty of the oxygen abundance is comparable to the size of the symbol and therefore not indicated.

(Langer 1989). Based on the mass-loss rate we found for DR1, the envelope is lost at a timescale of at least $\approx 8 - 9 \times 10^4$ years (for an unclumped wind, i.e. $f_c = 1$). For a helium-burning timescale of 4.3×10^5 year (Langer 1989), we find that DR1 is currently at least three-quarters into core-helium burning. Adopting a probable post-core helium burning lifetime of 10^4 year (Langer 1989), this also suggests that the volume filling factor cannot be much lower than $f_c \approx 0.2$, as otherwise the star should have already exploded. The temperature of DR1 is consistent with the temperature predicted for core-helium burning stars, while it is too low to correspond to post-core helium burning (Langer et al. 1988).

Turning the argument around, the mass-loss rate has obviously been large enough to uncover the material which was inside the convective core in the middle of core-helium burning, i.e. *before* core-helium burning finished. Adopting the helium-burning timescale given above, this implies that $\dot{M} > 4.7 M_{\odot} / \frac{1}{2} \times 4.3 \times 10^5 \text{ yr} \approx 2.2 \times 10^{-5} M_{\odot} \text{ yr}^{-1}$.

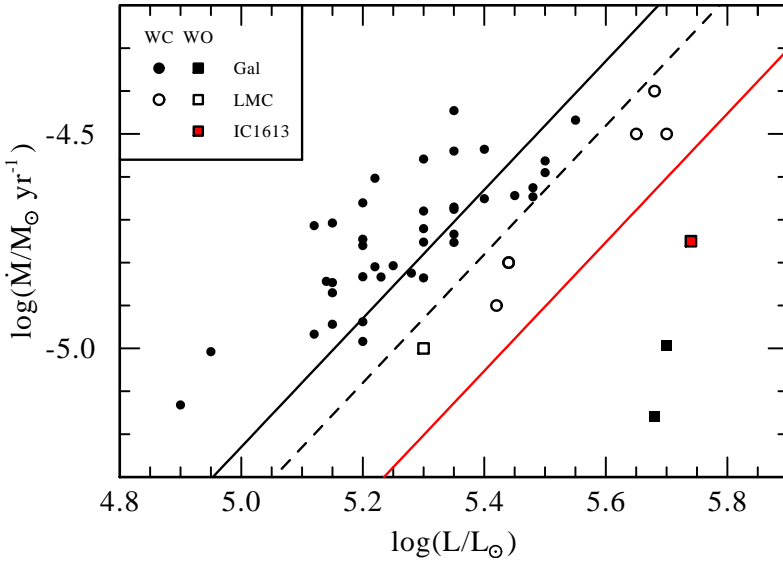


Figure 4.12: Comparison of the mass-loss rates and luminosity of WC and WO stars in different metallicity environments to the mass-loss relation WR1 of Yoon & Langer (2005). The solid black line represents the relation for $Z = Z_{\odot}$, the dashed black line $Z = 1/2 Z_{\odot}$, and the solid red line $Z = 1/7 Z_{\odot}$. The solid symbols represent the results from Sander et al. (2012), the open symbols represent the results from Crowther et al. (2000, 2002), and the red square indicates the location of DR1.

4.5.3 Mass-loss rate

Figure 4.12 shows a comparison of the mass-loss rate and luminosity of DR1 to the observed values for WC and WO stars in the Galaxy (Sander et al. 2012) and the LMC (Crowther et al. 2000, 2002). The plot clearly shows that the mass-loss rate of WC stars depends on stellar luminosity and the metallicity of the environment. This is in line with model predictions by Vink & de Koter (2005) and Gräfener & Hamann (2008), who find that the metallicity dependence of WR mass loss is mainly controlled by the iron abundance.

DR1 fits in this picture, as its mass-loss rate is well below the values found for WC stars of similar luminosity in the LMC. The two Galactic WO stars studied by Sander et al. (2012) have surprisingly low mass-loss rates. This could be caused by the modeling of the $O\text{VI } \lambda\lambda 3811\text{-}34$ line, as this requires a low mass-loss rate to prevent the emission from being re-absorbed in the stellar wind. The mass-loss rate of the LMC WO star analysed by Crowther et al. (2000), who do not fit the $O\text{VI } \lambda\lambda 3811\text{-}34$ emission, is consistent with the metallicity trend.

Alternatively, the low mass-loss rates of the Galactic WO stars may be an indication that these stars do not follow a well-defined dependence on L and Z . One of

the reasons for this could be their high temperature. Temperature effects for WR stars are predicted by Gräfener & Hamann (2008), albeit in a different temperature regime. As pointed out by Gräfener et al. (2012), there may exist a dichotomy between the winds of early WR subtypes which are likely driven by the hot iron opacity peak at 150 kK, and later subtypes which may have radially inflated envelopes and much cooler winds (cf. also Nugis & Lamers 2002; Lamers & Nugis 2002). The existence of such inflated envelopes has been questioned by Petrovic et al. (2006).

Figure 4.12 also shows scaled-down fits to empirical mass-loss rates by Hamann et al. (1995), as provided by Yoon & Langer (2005, their relation WR1). The scaling reduces the empirical rates by a factor of six to correct for the effect of clumping. The mass-loss rate is assumed to scale proportional to $Z^{0.5}$. This prescription reproduces the observed luminosity and metallicity dependence of WR mass loss reasonably well, save for the two Galactic WO stars.

4.5.4 Final fate

The eventual fate of DR1 is mostly determined by its mass prior to supernova explosion. Stars with a final mass $> 10 M_{\odot}$ are likely to form black holes (e.g., Georgy et al. 2009), producing a faint supernova or no supernova at all. If rapidly rotating, however, it is possible that such massive stars produce a bright type Ib/c supernova, possibly with an associated gamma-ray burst (e.g., Woosley & Bloom 2006). This scenario is more likely at low metallicities, as the mass-loss rates are lower during the various stages of evolution, reducing the angular momentum loss. The massive core can therefore more easily retain the angular momentum needed to power the explosion.

Sander et al. (2012) suggest that the two Galactic WO stars in their analysis have high rotational velocities ($\approx 1000 \text{ km s}^{-1}$) based on the shape of the lines. If this is indeed the case, these stars would be potential progenitors of GRBs. Even though the line shapes of DR1 can be well fitted by a non-rotational model, we cannot exclude that the star is fairly rapidly rotating, as convolving with rotational profiles of up to 500 km s^{-1} ($\approx 0.25 v_{\text{crit}}$) has a negligible effect on the line shapes. Larger projected rotational velocities broaden the lines too much to fit our data and can thus be excluded.

Despite the efforts of finding the progenitors of type Ib/c SNe in pre-supernova images, none have been identified so far (e.g., Eldridge et al. 2013). If the progenitors are hot WR stars like DR1, they would be very hard to detect, as despite their high bolometric luminosity, their visual brightness is very low due to their very high temperature (Yoon et al. 2012).

Although there is still a considerable amount of helium present in our DR1 model, this does not exclude a final explosion in the form of a type Ic supernova. In single

stars the helium mass fraction at the surface can be as large as 50 per cent without helium being detected in the spectrum of the supernova (Dessart et al. 2011a). The surface helium mass fraction of DR1 is below that level (44 per cent).

4.6 Conclusions

In this Chapter we have presented a quantitative spectroscopic analysis of DR1, one of only two WO stars known at a SMC-like metallicity. We have modeled the X-Shooter spectrum using `CMFGEN` in order to derive the stellar and wind parameters. Our best-fit model reproduces the strength and shape of all the He, O and C lines in the 320–2000 nm wavelength range covered by our observations, including the O VI $\lambda 5290$ line and the O VI $\lambda 5290$ / O V $\lambda 5592$ ratio. However, our model cannot reproduce the strong O VI $\lambda\lambda 3811$ –34, which is the prime observational diagnostic of the WO spectral type, simultaneously with the rest of the DR1 spectrum.

We discussed the possibility that a significant part of the O VI $\lambda\lambda 3811$ –34 line flux is originating from a mechanism that is not included in the modeling, for instance X-ray emission produced at (or close to) the base of the wind. Compared to early WC stars, the stellar temperature of DR1 is high, but the surface oxygen abundance is *not* enhanced. This suggests that the presence of the highly ionized oxygen emission is caused by excitation effects due to the high temperature.

DR1 is embedded in the hottest known He II emitting nebula in the Local Group. The properties of the nebula are consistent with DR1 being the central ionizing source. In particular the high electron temperature of the nebula is suggestive of a very hot central source and a low ambient metallicity. The capacity of DR1 to fully ionize helium may also be relevant for our understanding of the epoch of He II reionization, believed to have occurred at redshifts $z \approx 4 - 2.7$ (e.g., Syphers & Shull 2013). Although usually attributed to quasars, WO stars like DR1 may also have contributed to the He II ionization.

Our best fit model and the derived oxygen and carbon abundances suggest that DR1 should be seen as a hot (i.e. earlier-type) WC star, and that the presence of strong O VI $\lambda\lambda 3811$ –34 emission in WO spectra does not necessarily imply a larger oxygen abundance, hence a more advanced evolutionary stage. This statement is of importance when comparing with evolutionary computations: WO as a spectral type – i.e. defined by the presence of strong O VI $\lambda\lambda 3811$ –34 emission – is not equivalent to the definition of WO stars usually adopted from a theoretical point of view. The latter is based on an enhanced oxygen content (surface abundances $(C + O)/He > 1$ by number, e.g. Smith & Maeder 1991).

DR1 is located in the high-temperature and high-luminosity domain of the HRD. Compared to evolutionary tracks, its location is compatible with the late stages of

evolution of stars with an initial mass $> 60 M_{\odot}$, although this number is subject to various assumptions in the theoretical tracks. The carbon and oxygen abundances and stellar temperature suggest that DR1 is currently well into its core-helium burning stage. Based on the derived mass-loss rate, the clumping of the stellar wind should be moderate ($f_c \gtrsim 0.2$), as otherwise the star should have already exploded.

Although we find that the WO phase likely does not represent a stage of enhanced oxygen abundance compared to WC stars, we do not exclude the possibility that WO stars are in a more advanced evolutionary stage than WC-type Wolf-Rayet stars. The higher temperatures of WO's may be the result of progressive stripping of the outer layers through the radiation driven wind, exposing consecutively hotter layers.

Alternatively, WO and WC stars may be the end products of stars from different initial mass ranges, in which case the question of evolutionary connection between WO and WC stars does not apply. Detailed spectroscopic analyses of more WO and early-WC stars are needed to decide whether the properties of DR1, in particular its high temperature and WC-like oxygen abundance, are representative of the WO stars as a class and to investigate further the nature of the WO's and their possible evolutionary connection with WC stars.

Acknowledgments

S.d.M. acknowledges support through a Hubble Fellowship grant HST-HF-51270.01-A awarded by the STScI, operated by AURA, Inc., under contract NAS 5-26555 and a Einstein Fellowship grant PF3-140105 awarded by the Chandra X-ray Center, operated SAO under the contract NAS8-03060.

The properties of the single WO stars

F. Tramper, S. Straal, G. Gräfener, L. Kaper, A. de Koter, N. Langer, H. Sana & J.S. Vink

To be submitted to Astronomy and Astrophysics

Abstract

Oxygen sequence Wolf-Rayet (WO) stars represent a very rare stage in the evolution of massive stars. Their spectra show strong emission of helium-burning products, in particular highly ionized carbon and oxygen. The properties of WO stars can be used to provide unique constraints on the (post-)helium burning evolution of massive stars, as well as the remaining lifetime and the expected properties of their supernovae. We aim to homogeneously analyse the currently known presumed-single WO stars to obtain the key stellar and outflow properties and to constrain their evolutionary state. We use the line-blanketed non-local thermal equilibrium atmosphere code `CMFGEN` to model X-Shooter spectra of the WO stars and deduce the atmospheric parameters. We calculate dedicated evolutionary models to determine the evolutionary state of the stars. The WO stars have extremely high temperatures that range from 150 kK to 210 kK, and very low surface helium mass fractions that range from 44% down to 14%. Their properties can be reproduced by evolutionary models with $M_{\text{He,ini}} = 15 - 25 M_{\odot}$ that exhibit a fairly strong (on the order of a few times $10^{-5} M_{\odot} \text{ yr}^{-1}$), homogeneous ($f_c > 0.3$) stellar wind. WO stars represent the final evolutionary stage of stars with estimated initial masses of $M_{\text{ini}} = 40 - 60 M_{\odot}$. They are post core-helium burning and predicted to explode as type Ic supernovae within a few times 10^3 years.

5.1 Introduction

The enigmatic oxygen sequence Wolf-Rayet (WO) stars represent a very rare stage in massive star evolution. Their spectra are characterized by strong emission of highly ionized carbon and oxygen, and in particular O VI $\lambda 3811\text{-}34$ Å. Their emission-line spectra point to dense, outflowing atmospheres. Despite their rarity, the WO stars can provide key information in our understanding of massive star evolution.

Although the progenitors of hydrogen-free type Ib and Ic supernovae (SNe) have not yet been identified, it is very likely that they are evolved Wolf-Rayet stars (e.g., Yoon et al. 2012). WO stars are potential progenitors of the helium-deficient type Ic SNe, as they may have a very low helium abundance. If they are rapidly rotating when they explode, they could produce an associated long-duration gamma-ray burst (GRB, e.g., Woosley & Bloom 2006).

The tell-tale signature of WO stars is their O VI $\lambda 3811\text{-}34$ Å emission. This emission was first found in the spectra of the central stars of planetary nebulae. However, Sanduleak (1971) pointed out that five of the stars showing O VI $\lambda 3811\text{-}34$ Å have broad, Wolf-Rayet like emission lines and do not appear to have an associated nebula. It was therefore suggested they are part of the carbon sequence Wolf-Rayet (WC) class. Barlow & Hummer (1982) argued that these WC O VI stars should be seen as a separate class of Wolf-Rayet stars, and introduced the first WO classification scheme.

Since their discovery, the WO class has been commonly interpreted as a very short stage of evolution of massive stars covering an initial mass range of approximately $45 - 60 M_{\odot}$ after the carbon sequence Wolf-Rayet (WC) phase (e.g., Sander et al. 2012; Langer 2012). In such a scenario the emission lines of highly ionized oxygen reflect the high oxygen abundance that is expected near the end of core-helium burning. The very high stellar temperature that is needed to produce O VI emission is expected if WOs are indeed the descendants of WC stars, as the envelope is being stripped by the stellar wind and consecutively hotter layers are revealed. An alternative scenario is that WO stars originate from higher mass progenitors. In this case the stars are hotter and the O VI emission could purely be an excitation effect, and a high oxygen abundance is not necessarily implied (e.g., Hillier & Miller 1999).

If WO stars represent a later stage of evolution compared to WC stars, the surface abundance of carbon and oxygen is expected to be high. If these can be measured, and a good estimate of the stellar mass can be obtained, the WO stars can provide unique observational constraints on the illusive $^{12}\text{C}(\alpha, \gamma)^{16}\text{O}$ thermonuclear reaction rate. This rate is currently only weakly constrained, with an uncertainty on the order of 30% (e.g., Tur et al. 2006).

At the time of writing, nine members of the WO class are known, two of which are in a binary system. Table 5.1 lists the coordinates, names, and metallicities (Z) of all these stars. Throughout the paper, the IDs listed in this table will be used as

Table 5.1: Overview of the known WO stars.

ID ^a <i>This work</i>	R.A. (J2000)	Dec. (J2000)	Spectral type ^b	Z (Z _⊙)	SIMBAD ID ^c	Other IDs
WO-MW-1	17:45:47.56	-26:10:26.9	WO2	1	V* V3893 Sgr	WR 102 [S71d] 4 (Sand 4) [S71d] 5 (Sand 5)
WO-MW-2	20:21:44.35	+37:22:30.6	WO2	1	WR 142	
WO-MW-3	17:32:03.31	-35:04:32.4	WO3	1	WR 93b	
WO-LMC-1	05:39:34.31	-68:44:09.1	WO3	0.5	Brey 93	BAT99 123 [S71d] 2 (Sand 2)
WO-LMC-2	05:18:11.01	-69:13:11.3	WO4	0.5	[L72] LH 41-1042	
WO-LMC-3	05:18:10.33	-69:13:02.5	WO2	0.5	—	LMC195-1 ^d
WO-IC1613-1	01:05:01.61	+02:04:20.6	WO3	0.15	NAME DR 1 in IC 1613	[BUG2007] B 17
WO-MW-4	10:51:38.93	-60:56:35.2	WO4 + O5((f))	1	V* V574 Car	WR 30a [MS70] 4 (MS4)
WO-SMC-1	01:21:04.13	-73:25:03.8	WO4 + O4	0.2	2MASS J01310412-7325038	SK 188 [S71d] 1 (Sand 1)

Notes. The upper part of the table shows the (apparently) single WO stars, the bottom part the binaries.

^(a) The ID indicates the host galaxy (MW = Milky Way, LMC = Large Magellanic Cloud, SMC = Small Magellanic Cloud). ^(b) See Section 5.2.1 for the spectral classification of the single stars. Binary classifications are from Massey et al. (2000) and Moffat & Seggewiss (1984). ^(c) <http://simbad.u-strasbg.fr/simbad/> ^(d) Not yet listed in Simbad. Designation from Massey et al. (2014).

the designation for the stars. Two WO stars have recently been discovered in the LMC. The first, the WO4 WO-LMC-2, was discovered by Neugent et al. (2012). The second one was reported by Massey et al. (2014), and is, remarkably, located only 9'' away from WO-LMC-2.

As a first step in our effort to investigate the nature of the WO stars, Tramper et al. (2013, Chapter 4) performed a detailed spectroscopic analysis of WO-IC1613-1. Located in the Local Group dwarf galaxy IC 1613, this star is the lowest metallicity WO star known, with a metallicity $Z \sim 0.1 - 0.2Z_{\odot}$ (Chapter 4). The stellar parameters that were derived confirm the expected very high stellar temperature, close to the helium terminal-age main sequence (He-TAMS). However, the derived surface abundances of helium, oxygen, and carbon were comparable to those found in early WC stars. Thus, if WO-IC1613-1 is representative for the WO stars, these stars may be descendants of higher mass progenitors than WC stars.

In this paper, we perform a homogeneous spectroscopic analysis of all the remaining (apparently) single WO stars that are known, with the exception of the recently discovered star in the LMC (WO-LMC-3, Massey et al. 2014). The stellar parameters, together with the results from Chapter 4, are used to determine the nature of WO stars. We use dedicated helium-burning models to constrain their evolutionary stage as well as to predict their remaining lifetime.

In the next section, the observations and data reduction are described. Section 5.3 outlines the modeling of the observed spectra, and the resulting properties are discussed in Section 5.4. These are used to determine the remaining lifetime in Section 5.5. Finally, we conclude on the nature of the WO stars in Section 5.6.

5.2 Observations and data reduction

All observations presented in this work have been obtained at the European Southern Observatory using the X-Shooter instrument (Vernet et al. 2011) on the *Very Large Telescope*. WO-MW-2 and WO-MW-4 were observed under program ID 093.D-0591, and all the other stars as part of the NOVA program for guaranteed time observations under program ID 091.C-0934. X-Shooter covers a wavelength range from 3 000 Å to 25 000 Å by directing the light in three separate arms: the UVB (3 000-5 500 Å), VIS (5 500-10 000 Å), and NIR (10 000-25 000 Å).

To prevent detector saturation by the strong emission lines, the observations were split up into several shorter exposures. An overview of the exposure times and slit widths used is given in Table 5.2. All observations were done in nodding mode with a nod throw of 5''.

The data of all stars have been reduced using the X-Shooter pipeline v2.2.0, which produces flux-calibrated 1D spectra. The flux calibration is performed using

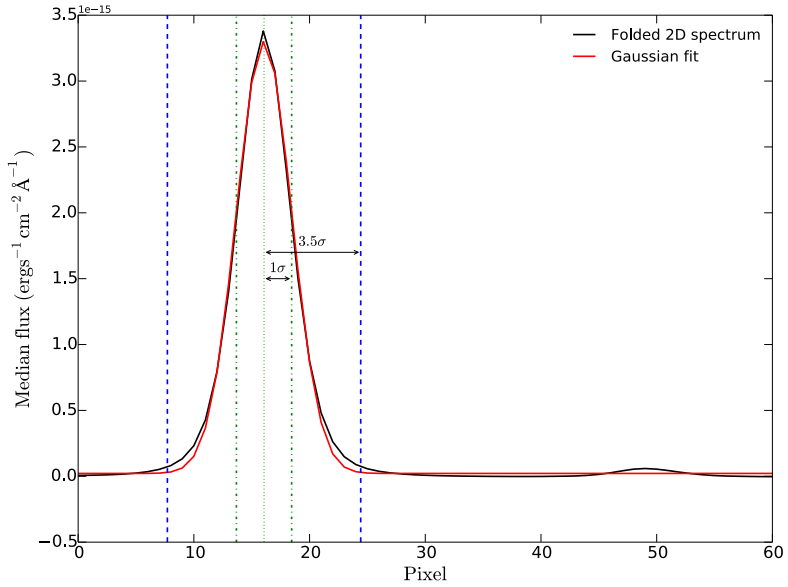


Figure 5.1: Example of the extraction of the 1D spectrum of WO-MW-4 for one of the nodding positions. The cross-dispersed profile is shown in black, the Gaussian fit in red. The blue dashed lines indicate the region that is extracted (corresponding to $\pm 3.5\sigma$, with σ the standard deviation of the fitted Gaussian profile).

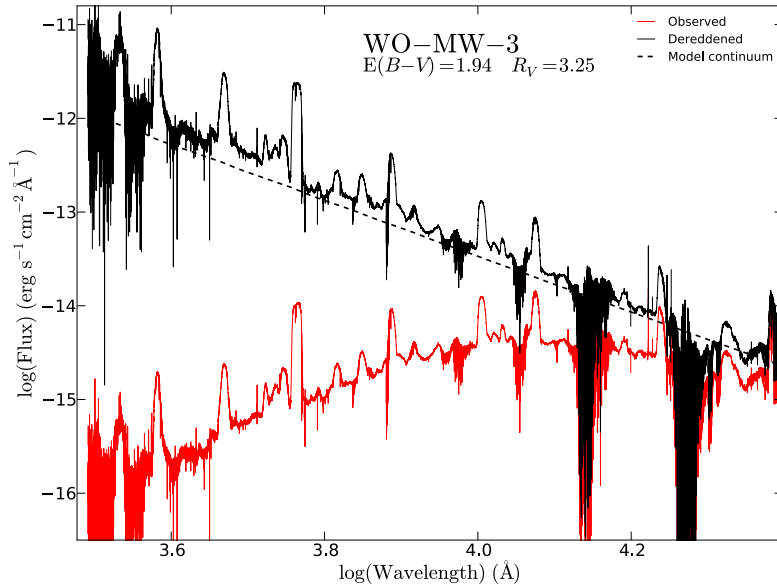


Figure 5.2: Example of the extinction correction procedure for the highly reddened WO-MW-3. The flux-calibrated spectrum before and after the extinction correction is displayed in red and black, respectively. The scaled continuum of a model spectrum is indicated by the dashed black line.

Table 5.2: Overview of observations.

ID	MJD <i>At start exp.</i>	T_{exp}^a (s)	Slit width ^a (")	Spec. Standard
WO-MW-1	56490.069	4 × 120	0.8, 0.9, 0.9	GD153
WO-MW-2	56783.371	8 × 200/260/260	0.8, 0.9, 0.9	LTT7987
WO-MW-3	56489.138	4 × 600	0.8, 0.9, 0.9	EG274
WO-LMC-1	56409.978	10 × 180	0.8, 0.9, 0.9	LTT3218
WO-LMC-2	56522.351	10 × 180	0.8, 0.9, 0.9	FEIGE-110
WO-MW-4	56771.212	8 × 200/260/260	0.8, 0.9, 0.9	LTT7987
WO-SMC-1	56522.388	8 × 40	0.5, 0.7, 0.4	EG274

Notes. ^(a) If a single value is given it is the same for all three X-Shooter arms; if three values are given it is for the UVB, VIS and NIR arms, respectively.

observations of the spectro-photometric standard stars listed in Table 5.2 taken during the same night. Two of the stars (WO-MW-4 and WO-LMC-2) had another bright object in the slit, and the standard reduction was not sufficient. For these stars, we first obtained reduced the 2D spectrum for each nodding position separately, without sky subtraction. We then subtracted the sky background using a clean part of the slit.

Because the atmospheric dispersion corrector was unavailable at the time of observations, the traces of the two stars mentioned above were not at a constant position on the slit as a function of wavelength in the UVB spectra. We therefore extracted the 1D spectra by integrating the flux at each wavelength over a sufficiently large part of the slit. While this introduces additional noise, the quality of the data is high enough for this to be negligible. In the VIS arm the traces of both stars were at a constant position on the slit. Here, we folded the spectra in the wavelength direction, and fitted a Gaussian to the stellar signal. The 1D spectra were then subtracted using the parts of the slit corresponding to $\pm 3.5\sigma$ covered by the average cross-dispersed point-spread function. Figure 5.1 shows an example, in which the second object in the slit is located around pixel 50. While the median flux of this object over the full wavelength range is very low, it has a noticeable effect on the extracted spectrum if not taken into account, in particular at the shorter wavelengths. For both stars, the flux of the contaminating object was negligible in the NIR, and the 1D spectra were obtained using the nodding reduction, as this facilitates a better correction for the copious telluric lines. The resulting fluxes connect well with the VIS spectra which indicates that the contribution of the second object can indeed be ignored.

The flux-calibrated spectra of the stars were extinction corrected using the CCM

Table 5.3: Reddening and total-to-selective extinction.

ID	$E(B - V)$	R_V
WO-MW-1	1.26	3.10
WO-MW-2	1.72	2.85
WO-MW-3	1.94	3.25
WO-LMC-1	0.19	3.10
WO-LMC-2	—	—

extinction laws (Cardelli et al. 1989; O’Donnell 1994). A `CMFGEN` model (see Section 5.3.2) of the corresponding metallicity was used as a template for the slope of the spectrum (see Figure 5.2 for an example). The value of the total-to-selective extinction R_V was only adjusted if a proper dereddening could not be achieved using the average value of $R_V = 3.1$. The derived values for $E(B - V)$ and R_V are listed in Table 5.3.

The spectrum of one of the single WO stars, WO-LMC-2, also shows a steeper slope, but does not display spectral features from a companion. Although a faint star is detected in a UV image at a small projected distance from WO-LMC-2 (see Figure B.1), the spectrum could not be corrected by assuming a Rayleigh-Jeans contribution from this object. Instead, we have artificially corrected the flux to match the model WO slope for LMC metallicity. The drawback of this approach is that the reddening cannot be determined for this object, implying a larger uncertainty in the derived luminosity. The flux correction for WO-LMC-2 is described in detail in Appendix B.1. The extinction-corrected, flux-calibrated spectra of all WO stars are presented in Figures 5.3 and 5.4.

5.2.1 Spectral classification

Two quantitative classification schemes exist for the WO subclasses. The first divides the WO class in five subclasses, ranging from WO1 to WO5 (Kingsburgh et al. 1995). This classification scheme is based on the equivalent width (EW) ratio of O VI λ 3811-34 to C IV λ 5801-12 and O VI λ 3811-34 to O V λ 5590.

Crowther et al. (1998) introduced a classification scheme for WC and WO stars in which the WO class is divided into four subtypes, from WO1 to WO4, and connects to the WC class at WC4. This classification is based on the same EW ratios as the scheme from Kingsburgh et al. (1995), but also includes the full width at half maximum (FWHM) of C IV λ 5801-12 and the EW ratio of O VII λ 5670 to O V λ 5590.

We adopt the classification scheme of Crowther et al. (1998) in this paper. The spectral types we derive are given in Table 5.1 (see also Appendix B.4).

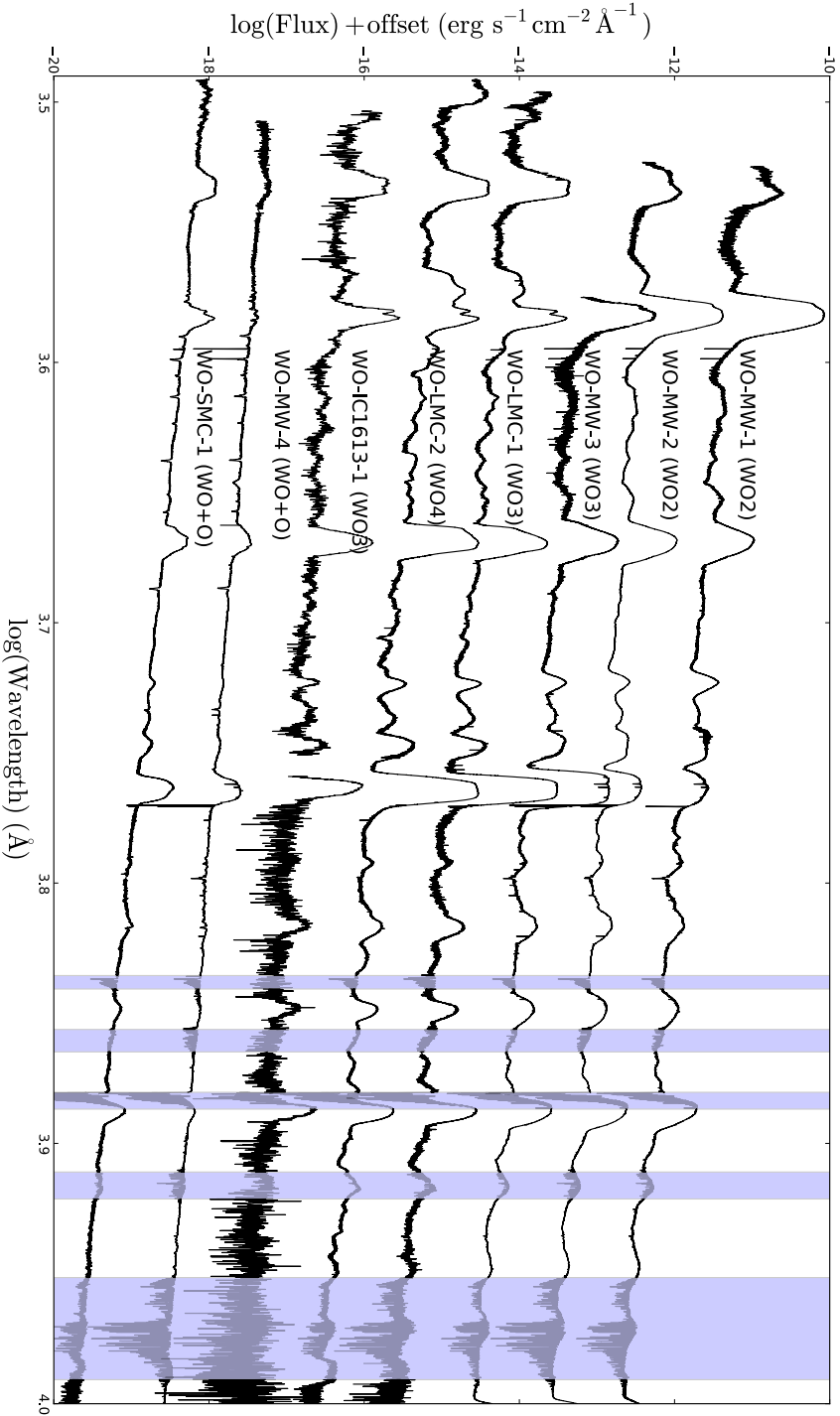


Figure 5.3: Dereddened, flux-calibrated X-Shooter spectra in the UVB and VIS range (3 000-10 000 Å). The flux has been multiplied by an arbitrary factor for plotting purposes. Nebular emission and residuals from the sky subtraction have been clipped, and wavelength ranges affected by strong atmospheric features are displayed within the shaded areas. The spectrum of WO-IC1613-1 has been rebinned to 1 Å.

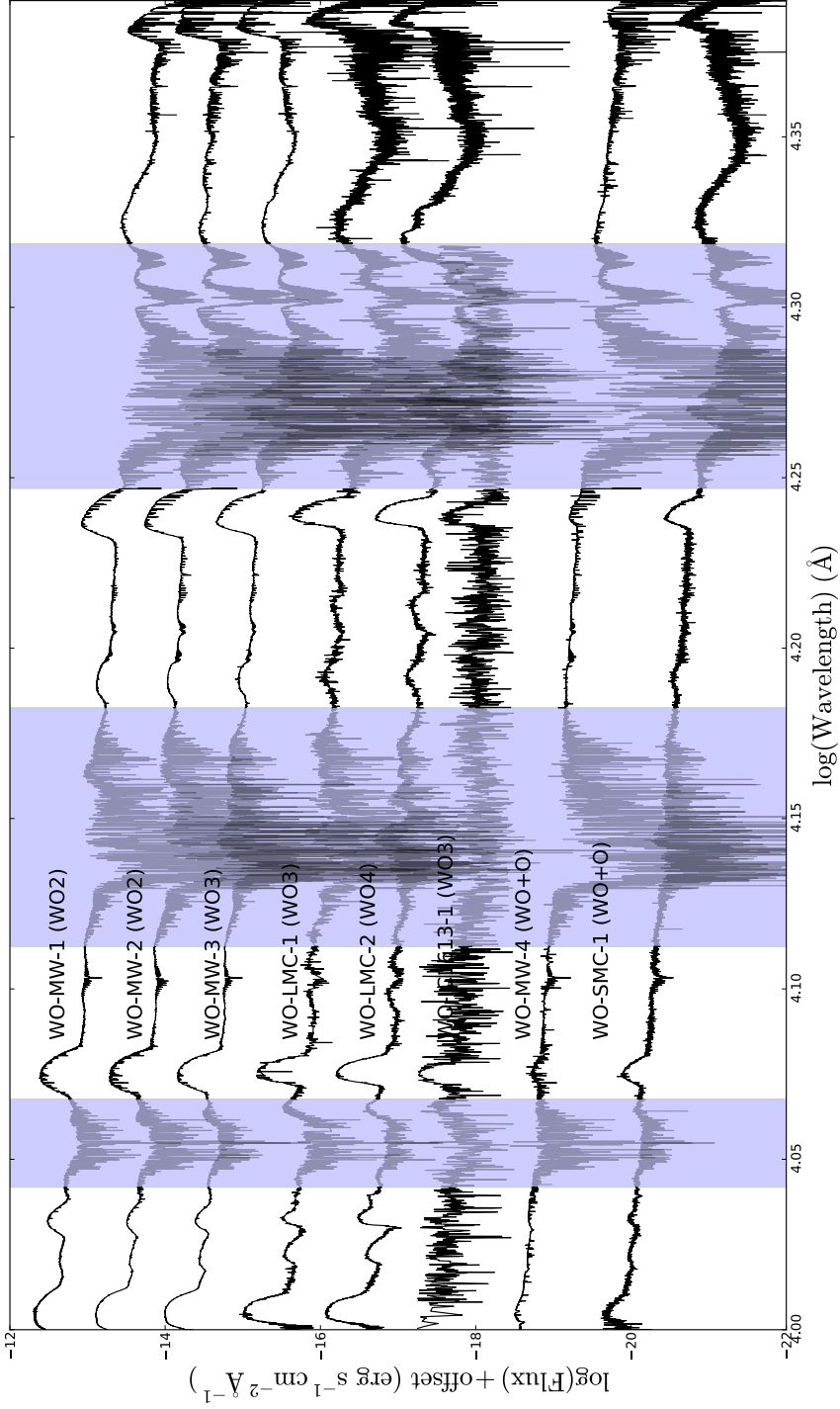


Figure 5.4: As Figure 5.3, but for the NIR range (10 000-25 000 Å). The spectra of WO-LMC-1, WO-LMC-2 and WO-SMC-1 have been binned to 1 Å. The spectrum of WO-IC1613-1 has been binned to 2 Å, and only extends to 20 000 Å due to the use of the X-Shooter K-band blocking filter.

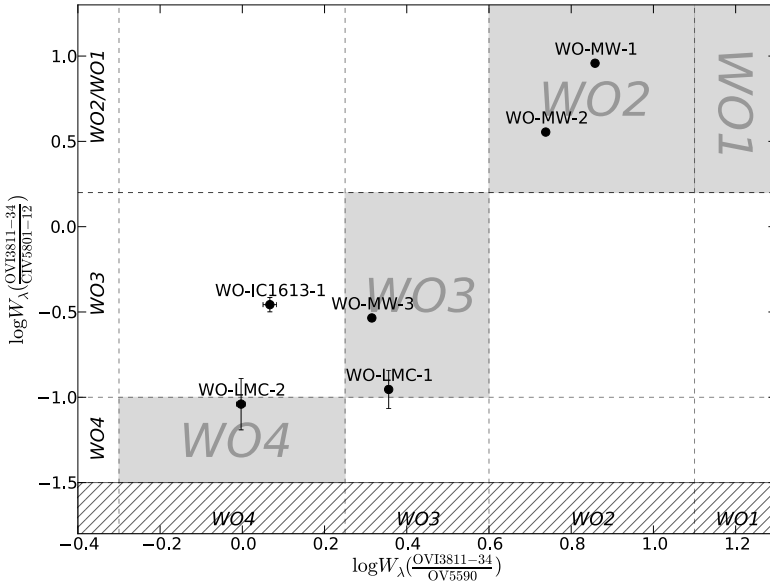


Figure 5.5: Comparison of the primary and secondary spectral classification criteria (x and y axis, respectively). The shaded areas indicate the regions where the two criteria agree on the spectral type. If these are not in agreement, the classification depends on the FWHM of C IV λ 5801-12. This is only the case for WO-IC1613-1, which we assign the spectral type WO3, in agreement with previous classifications. The dashed region indicates where the WC sequence begins.

5.3 Spectroscopic analysis

First, we briefly discuss the morphological properties of the flux-calibrated spectra. After that we perform a detailed quantitative spectroscopic analysis.

5.3.1 Morphological properties

The WO spectra in Figures 5.3 and 5.4 show clear trends with spectral type and metallicity. These trends reflect changes in the physical properties of the star and in the region in the wind where the lines are formed, and provide information for the subsequent modeling (Section 5.3.2).

Most notable is the increase in line width at higher metallicity. This is visible to a varying degree in all the spectral lines, and can be seen particularly well in the C IV and He II lines in the NIR. The broader lines at higher metallicity reflect an increase in the terminal velocity of the outflows from the stars.

The morphology of the characterizing O VI λ 3811-34 Å emission also changes with metallicity. At low metallicities (IC 1613 and LMC, but also for the binary in the

SMC) this doublet is clearly double-peaked, while it is fully blended in the spectra of the galactic stars. The O v λ 5590 Å line profiles change from a roughly parabolic shape in the stars with a sub-galactic metallicity to a broad flat-topped shape in the MW stars. This reflects a change in the optical depth of the line-forming region: the line is formed in the optically thick region of the outflow for the lower metallicities, while for the galactic stars it is formed in optically thin regions.

5.3.2 Modeling

To perform a homogeneous quantitative spectroscopic analysis of the WO stars we employ the CMFGEN code of Hillier & Miller (1998). This code iteratively solves the transfer equation in the co-moving frame, and accounts for effects such as clumping and line blanketing. Our fitting strategy has been described in detail in Chapter 4. Here we only describe relevant assumptions and changes in the applied diagnostics. Our modeling approach aims to reproduce all the observed trends in the sample, as well as to provide a good fit to each of the individual spectra.

In Chapter 4, the weak optically thin He II line at 4859 Å was used as a diagnostic for the stellar temperature. This line is not recognizably present in the spectra of the LMC and MW stars that are analyzed here. Instead, we use the shape of the He II λ 6560 Å as a temperature probe. The blue wing of this line has contributions from O v and C IV, and the shape of the line profile can only be fitted by models with the correct combination of temperature and carbon and oxygen abundances. Together with the other abundance diagnostics, this allows us to constrain the temperature with an accuracy of about 20 kK (see Figure 5.6).

To determine the luminosities of the stars, we adopt a distance of 50.12 kpc to the LMC (Gibson 2000), and distances of 4.6, 1.75, and 3.4 kpc for WO-MW-1, 2, and 3, respectively (Drew et al. 2004). We derive spectrophotometric V-band magnitudes for the observed spectrum and compare these to the Simbad values. This gives an estimate of the flux loss and error in the flux calibration of the observations. We model the luminosity by matching the distance-corrected model flux to the magnitude-corrected, dereddened observed flux in the V-band wavelength region. The model flux is not only determined by the luminosity, but is also affected by the mass-loss rate and stellar temperature. Therefore, like the determination of all other parameters, the luminosity determination is an iterative process.

Table 5.4 presents an overview of the best-fit parameters for all the single WO stars in our sample. Figures showing the best-fit model for each star are given in Appendix B.2. Table 5.4 also gives values for the transformed radius R_t , the wind efficiency η , and the ionizing fluxes $Q_{0,1,2}$. The ionizing fluxes indicate the number of photons per second that are available to ionize hydrogen (Q_0), and singly (Q_1) and doubly (Q_2) ionize helium.

Table 5.4: Properties of the single WO stars.

ID	$\log L$ (L_{\odot})	T_* (K)	R_* (R_{\odot})	$\frac{N_C}{N_{He}}$	$\frac{N_O}{N_{He}}$	v_{∞} (km s^{-1})	$\log \dot{M}$ ($M_{\odot} \text{ yr}^{-1}$)	$\log R_t$ (R_{\odot})	η	$\log \dot{Q}_0$ (s^{-1})	$\log \dot{Q}_1$ (s^{-1})	$\log \dot{Q}_2$ (s^{-1})
WO-MW-1	5.45	210	0.39	1.50	0.45	5000	-4.92	0.67	10.3	49.0	48.9	48.4
WO-MW-2	5.39	200	0.40	1.00	0.16	4900	-4.94	0.79	11.3	49.0	48.8	48.3
WO-MW-3	5.30	160	0.58	0.60	0.15	5000	-5.00	0.97	12.3	48.9	48.8	47.3
WO-LMC-1	5.20	170	0.47	0.63	0.13	3300	-5.14	0.82	7.3	48.9	48.7	47.6
WO-LMC-2	5.26	150	0.62	0.90	0.20	3500	-5.05	0.83	8.6	48.9	48.7	45.5
WO-IC1613-1	5.68	150	1.06	0.35	0.06	2750	-4.76	0.46	5.0	49.5	49.3	48.0

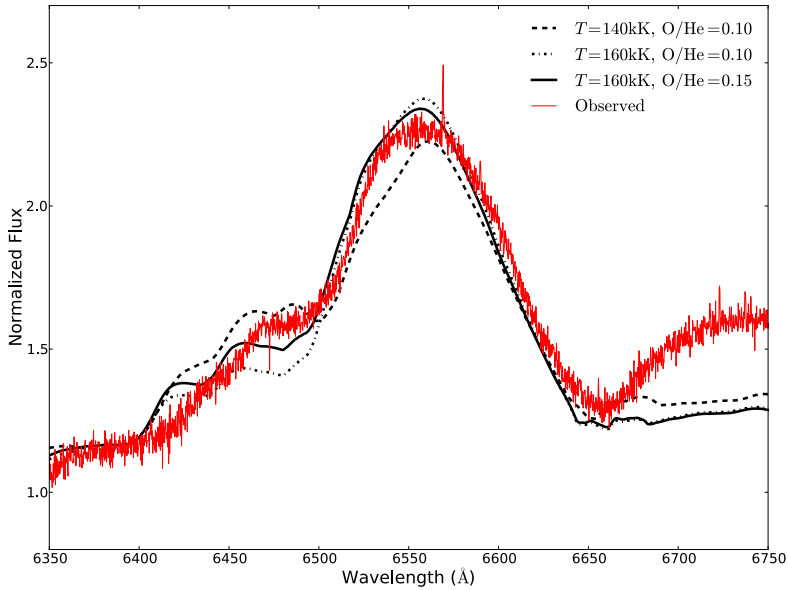


Figure 5.6: Behavior of the He II, O V, and C IV blend at 6560 Å for different values of the temperature and the oxygen abundance. The observed spectrum is from WO-LMC-2.

The transformed radius, introduced by Schmutz et al. (1989), is defined as:

$$R_t = R_* \left[\frac{v_\infty}{2500 \text{ km s}^{-1}} \left/ \frac{\dot{M}}{\sqrt{f_c} 10^{-4} M_\odot \text{ yr}^{-1}} \right. \right]^{2/3}, \quad (5.1)$$

where the volume filling factor (f_c) was first incorporated by Hamann & Koesterke (1998). The temperature (T_*) is the temperature at radius (R_*) at the base of the wind, where the underlying regions can be assumed to be in hydrostatic equilibrium. Combinations of parameters that keep R_t constant produce very similar spectra, making it a very useful quantity. For instance, it implies that when v_∞ and R_* are well constrained, the line flux is determined by the value of $\dot{M}/\sqrt{f_c}$. In Section 5.5 we use this property to constrain f_c .

The wind efficiency parameter gives the ratio of the wind momentum once the flow has reached the terminal velocity ($\dot{M}v_\infty$) and the photon momentum (L/c):

$$\eta = \frac{\dot{M}v_\infty c}{L}. \quad (5.2)$$

Thus, η indicates the average amount of scatterings that photons need to undergo in order to drive the wind. The values of η for the WO stars are in the range of 5 ~ 12, very similar to values found for WC stars (Sander et al. 2012). Multiple

photon scatterings are expected for optically thick winds (de Koter et al. 1997; Vink & Gräfener 2012; Gräfener & Vink 2013).

Overall, the observed spectra are well reproduced by our models, and allow us to constrain the temperature, surface abundances, and wind properties of the WO stars. Nevertheless, some of the observed spectral features are not fully reproduced. The O VI $\lambda 3811$ -34 Å cannot be reproduced while simultaneously fitting the overall spectrum, and the flux in this line is underpredicted by a factor of ~ 3 in our models. The cause of this is likely to be found in the susceptibility of the population of the upper level of the transition to X-ray excitation (see Chapter 4). Still, the strength of this line in our models does follow the observed trend with spectral type.

The observed spectra show some emission lines that are not in the model spectra. These lines belong to transitions of the higher ionization stages of oxygen and carbon (i.e., O VII, O VIII, and C V), for which we do not include atomic models. These ionization stages are treated as auxiliary levels, to ensure that the populations of the levels that are modelled are accurate. While it is possible to include these high ionization stages in our models, their level populations are highly dependent on the soft X-ray radiation field, and thus the presence of, e.g., shocks. This should not affect the derived properties of the stars, but does result in a slightly higher uncertainty in the temperature.

During the modeling we found that for models with very high temperatures ($T_* \gtrsim 190$ kK) the ratios between the O IV $\lambda 3404$ -12 Å, O V $\lambda 5598$ Å, and O VI $\lambda 5290$ Å lines can no longer be reproduced. For the stars that have such high temperatures we determine the oxygen abundance by adopting models where the oxygen line ratios are closest to the observed values. The uncertainty in the obtained abundance is investigated by fitting each of the individual oxygen lines, while adjusting the other parameters to preserve the overall fit to the spectrum. The range in oxygen abundances that results from this approach is small, and thus we expect them to be accurate.

Lastly, all spectra show to some extent a very broad emission feature at $\sim 21\,000$ Å. This feature is a blend of several emission lines of C IV, C III and He II, yet almost none of our models show emission in this region, with the model for WO-LMC-2 being the exception.

5.4 The properties of the single WOs

In this section we discuss the derived properties of the WO stars and we compare our results to previous research. We then place the WO stars in the Hertzsprung-Russell diagram (HRD) and compare their position with the WC stars and evolutionary tracks. Lastly, we discuss the mass-loss properties of the sample.

Table 5.5: Comparison of estimates of the terminal wind velocity.

ID	v_∞ (km s ⁻¹)	Reference
WO-MW-1	5000	This work
	5000	Sander et al. (2012)
	4600	Kingsburgh et al. (1995)
WO-MW-2	4900	This work
	5000	Sander et al. (2012)
	5500	Kingsburgh et al. (1995)
WO-MW-3	5000	This work
	5750	Drew et al. (2004)
WO-LMC-1	3300	This work
	4100	Crowther et al. (2002)
	4300	Kingsburgh et al. (1995)
WO-IC1613-1	2750	Tramper et al. (2013)
	2850	Kingsburgh & Barlow (1995)

5.4.1 Comparison with previous results

Stellar temperatures have been derived for WO-MW-1 and WO-MW-2 by Sander et al. (2012), who found 200 kK for both stars, in agreement with our results. Crowther et al. (2000) report $T_* = 150$ kK for WO-LMC-1 based on their modeling of the far-UV to visible spectrum. This is 20 kK lower than the temperature we obtain from fitting the near-UV to near-IR spectrum.

For all stars except WO-LMC-2 one or more measurements of the terminal wind velocity are reported in the literature (see Table 5.5). In most cases our values are lower than those previously reported and that are based on full-width at zero line emission and blue edge absorption of ultraviolet P-Cygni profiles. Disparities compared to the first method may be related to a calibration issue. Those with the second method may point to a difference in the treatment of the velocity stratification of the outflow. Several studies report evidence for the presence of two acceleration zones in early WC star winds, in line with theoretical considerations (Schmutz 1997). Such a stratification may be modeled using a double- β law (e.g., Crowther et al. 2000, 2002; Gräfener & Hamann 2005) and can explain the higher v_∞ values from P-Cygni profiles that originate further out in the wind than the optical and near-infrared recombination lines used by us.

Kingsburgh et al. (1995) estimated the surface abundance of carbon and oxygen for their sample of stars based on a recombination line theory, and estimate

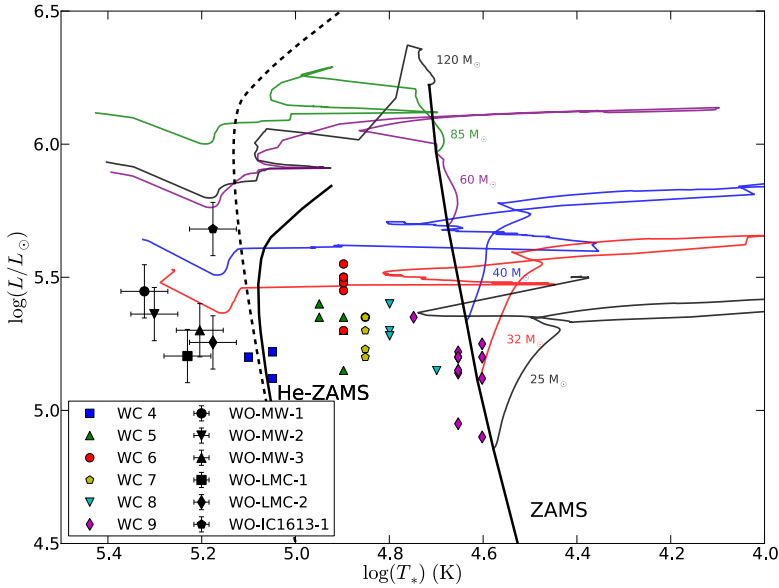


Figure 5.7: Location of the single WO stars in the Hertzsprung-Russel diagram. Also indicated are the WC stars analyzed by Sander et al. (2012) and evolutionary tracks for solar metallicity and an initial rotational velocity of 40% critical from Ekström et al. (2012). The helium zero-age main sequence (He-ZAMS) is indicated for solar metallicity (solid line) and SMC metallicity (dashed line).

$N_C/N_{\text{He}} = 0.51$ and $N_O/N_{\text{He}} = 0.11$ for WO-MW-1, and $N_C/N_{\text{He}} = 0.52$ and $N_O/N_{\text{He}} = 0.10$ for WO-MW-2. Sander et al. (2012) used $N_C/N_{\text{He}} = 0.44$ and $N_O/N_{\text{He}} = 0.25$ for their models for these stars. We find a higher carbon abundance than both these studies, and a similar oxygen abundance as Sander et al. (2012). Crowther et al. (2002) finds $N_C/N_{\text{He}} = 0.7$ and $N_O/N_{\text{He}} = 0.15$ for WO-LMC-1, higher than the values of $N_C/N_{\text{He}} = 0.51$ and $N_O/N_{\text{He}} = 0.11$ reported by Kingsburgh et al. (1995). The values that we find are very similar to the results from Crowther et al. (2002). Finally, Drew et al. (2004) find $N_C/N_{\text{He}} = 0.95$ and $N_O/N_{\text{He}} = 0.13$ from recombination line measurements. Our detailed modeling results in a lower carbon abundance, while the oxygen abundance is very similar.

5.4.2 Hertzsprung-Russell diagram

Helium-burning stars that show the products of helium burning in their spectra are expected to be located very close to the helium zero-age main-sequence (He-ZAMS) for most of the helium-burning lifetime. They only evolve toward hotter regions after exhausting the helium in their core (see, e.g., Figure 5.11).

Figure 5.7 shows the HRD with our results for the WO stars and the results from

Sander et al. (2012) for Galactic WC stars. All WO stars are located on the hot side of the He-ZAMS, which is a first indication that they may be post-helium burning objects. The WC stars are located between the ZAMS and He-ZAMS, and thus appear to be too cold for their core-helium burning state. In the past, this discrepancy has often been attributed to the extended photospheres of WR stars. However, the problem remains in recent studies which fully take this effect into account (e.g., Sander et al. 2012; Hainich et al. 2014).

A possible solution to explain the positions of WC stars in the HRD is stellar envelope inflation near the Eddington limit. In this context, inflation refers to the extended low-density envelopes in stellar models that reach the Eddington luminosity in their outer layers. This effect is predicted to be strongest at high metallicities (compare the solar and SMC metallicity He-ZAMS in Figure 5.7). Gräfener et al. (2012) could bring the predicted WR radii in agreement with the observations if the inflated sub-surface layers are clumped. Gräfener & Vink (2013) discussed the solution topology of inflated envelopes with optically thick winds and concluded that there are two types of possible solutions: cool stars with clumped inflated envelopes, and hot stars without envelope inflation but a lower mass-loss rate. While the former complies with the properties of late-type WC stars, the latter may represent the small group of WO stars and the small group of early-type WC stars.

The evolutionary tracks for solar metallicity from Ekström et al. (2012) are also plotted in Figure 5.7. The tracks do not reach the region of the HRD where most of the WO stars are located, which indicates that single-star models cannot currently explain them. However, if the mass loss of stars lower than $\sim 32M_{\odot}$ is higher than used in the tracks, these stars might reach the WO star region. In this case, the WO stars seem to be the descendants of stars with initial masses in the range $25M_{\odot} \leq M_{\text{ini}} \leq 60M_{\odot}$. The location of the He-ZAMS (for $Z = Z_{\odot}$ and $Z = 0.2Z_{\odot}$) that is plotted in Figure 5.7 corresponds to the helium-burning models used in Section 5.5. Towards higher luminosities, the He-ZAMS bends towards lower temperatures which is caused by inflation (not included in the plotted evolutionary tracks). The location of the WO stars favors them to be post-core helium burning, regardless of any uncertainties in the metallicity.

The evolutionary state of the WO stars is further discussed in Sections 5.5 and 5.6.

5.4.3 Mass-loss properties

Figure 5.8 compares the mass-loss rates found for the WO stars to those of the WC stars from Sander et al. (2012, MW stars) and Crowther et al. (2002, LMC stars). Also plotted are various forms of the empirical mass-loss predictions from Nugis &

Lamers (2000) for hydrogen-free WR stars:

$$\log \dot{M} = -11 + 1.29 \log \frac{L}{L_{\odot}} + 1.7 \log X_{\text{He}} + 0.5 \log Z. \quad (5.3)$$

Here, X_{He} is the helium mass-fraction, and $Z = 1 - X_{\text{He}}$. Z is thus almost equal to the sum of the carbon and oxygen mass fractions. Sander et al. (2012) find that the mass-loss rates for their WC stars are compatible with these predictions when using their average carbon and oxygen mass-fractions ($X_{\text{He}} = 0.55, Z = 0.45$, upper grey line in Figure 5.8). Crowther et al. (2002) finds an offset of approximately -0.2 dex for the mass-loss rates of LMC WC stars, corresponding to a metallicity dependence of $\sim Z_{\text{Fe}}^{0.5}$. Vink & de Koter (2005) predict a scaling of the mass-loss rates with $Z_{\text{Fe}}^{0.66}$ for WC stars with metallicities $0.1Z_{\text{Fe},\odot} \leq Z_{\text{Fe}} \leq 1Z_{\text{Fe},\odot}$, which we implement in Figure 5.8.

The Nugis & Lamers (2000) rates with the Vink & de Koter (2005) metallicity scaling match the observed WC mass loss rates from Sander et al. (2012) and Crowther et al. (2002) well. However, they severely underpredict the mass loss of the WO stars, which have a very low helium abundance. This is most notable for WO-MW-1, for which the predicted mass-loss rate is about 0.5 dex lower than the observed rate. This needs to be taken into account when comparing to evolutionary predictions that use the Nugis & Lamers (2000) mass-loss prescription.

Figure 5.9 shows the same comparison as Figure 5.8, but with the mass-loss relation WR1 from Yoon & Langer (2005), which is a scaled down version of the results of Hamann et al. (1995). We adjust this relation to have the same metallicity dependence as applied in Figure 5.8, yielding:

$$\log \dot{M} = -12.73 + 1.5 \log \frac{L}{L_{\odot}} + 0.66 \log \frac{Z_{\text{Fe}}}{Z_{\text{Fe},\odot}}. \quad (5.4)$$

Again, the mass-loss rates of the WC stars are well represented by this relation. The LMC and IC1613 WO stars also have a mass loss that is close to the predicted value. Only the mass-loss rate of the galactic WO stars is not well reproduced by Equation 5.4.

In line with earlier studies (e.g., Crowther & Hadfield 2006), the terminal wind velocities that we derive scale with metallicity. This behavior is shown in Figure 5.10. The metallicity dependence can be well represented by a linear relation.

5.5 Evolutionary state: remaining lifetime and final fate

The derived properties of the WO stars allow us to estimate the remaining lifetime of these stars, as well as to predict the type of SNe they will form. As helium burns at

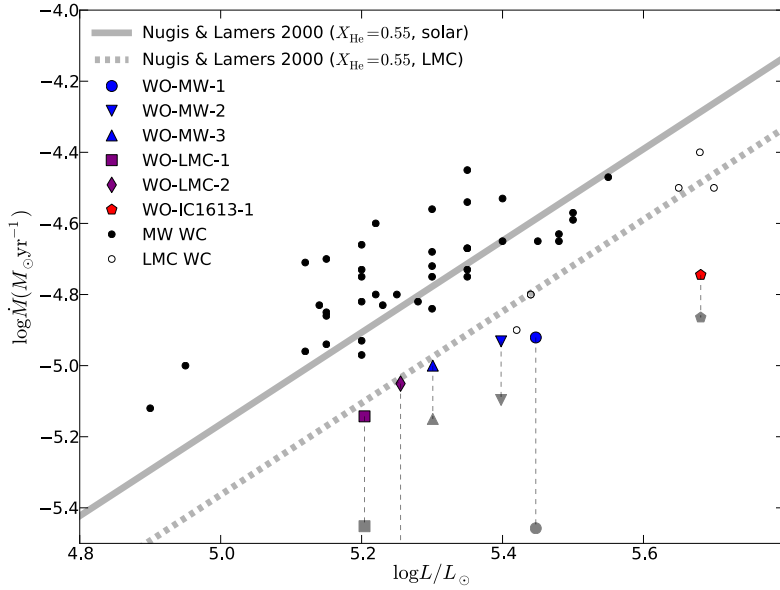


Figure 5.8: Mass loss versus luminosity relation with the location of the WO stars. Results for Galactic WC stars from Sander et al. (2012) and LMC WC stars from Crowther et al. (2002) are also indicated. Also plotted are the prediction for WC abundances of Nugis & Lamers (2000) with an additional $Z_{\text{Fe}}^{0.66}$ metallicity dependence (Vink & de Koter 2005). The grey symbols indicate the Nugis & Lamers (2000) predictions for the WO stars, which underpredict the observed mass-loss rates.

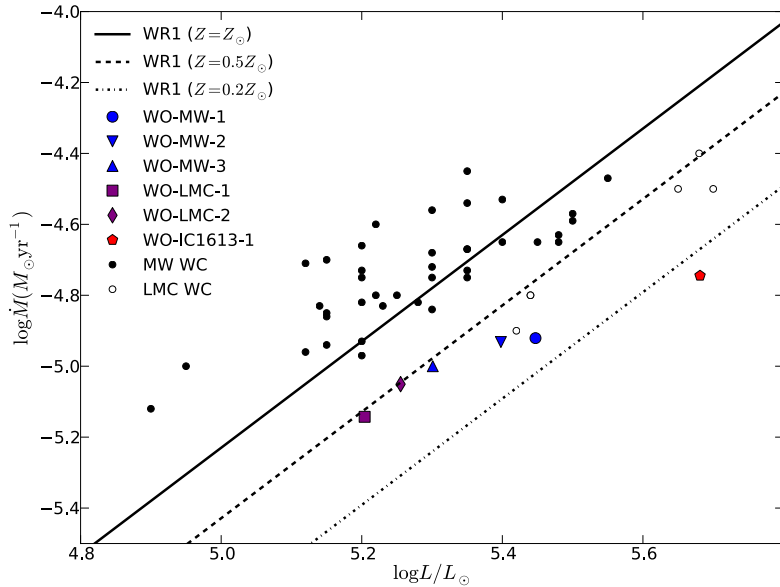


Figure 5.9: Same as Figure 5.8, but with the WR1 relation of Yoon & Langer (2005) adjusted to have a metallicity dependence of $Z_{\text{Fe}}^{0.66}$ (Vink & de Koter 2005).

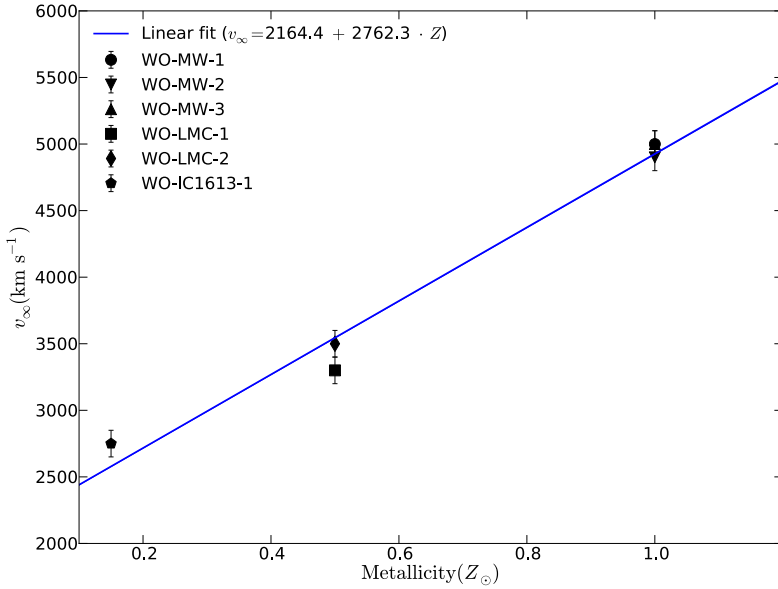


Figure 5.10: Scaling of the terminal wind velocity in WO stars with metallicity.

a more or less constant rate, the currently observed surface composition corresponds to material that was in the (fully mixed) convective core of the star at a time that is roughly proportional to $(1 - X_{\text{He}}) \times \tau_{\text{He}}$, with τ_{He} the duration of core-He burning. In Chapter 4, we used this fact to put a limit on the current stage of helium-burning for WO-IC1613-1.

In this work, we take a more detailed approach. We use the Binary Evolution Code (BEC, Yoon et al. 2006; Yoon & Cantiello 2010; Brott et al. 2011) to model the WR stars as non-rotating hydrogen-free helium stars. BEC is a state-of-the-art, one-dimensional hydrodynamic implicit Lagrangian code, and is well-suited to investigate stars that evolve close to the Eddington limit (Köhler et al. 2014, *in preparation*).

In particular, convection is treated within the framework of the standard Mixing Length Theory (Böhm-Vitense 1958) with the mixing length set to 1.5 times the local pressure scale-height. All the models were set to hydrostatic equilibrium. The models are evolved from the He-ZAMS until at least core-oxygen ignition.

We calculate evolutionary models for each of the WO stars, with the aim to reproduce the stellar temperature and luminosity at the point where the surface helium abundance of the models equals the observed values (see Table 5.6). We use the metallicities listed in Table 5.1. As shown before, the mass-loss rates from Nugis & Lamers (2000) that are normally used in these evolutionary models are not represen-

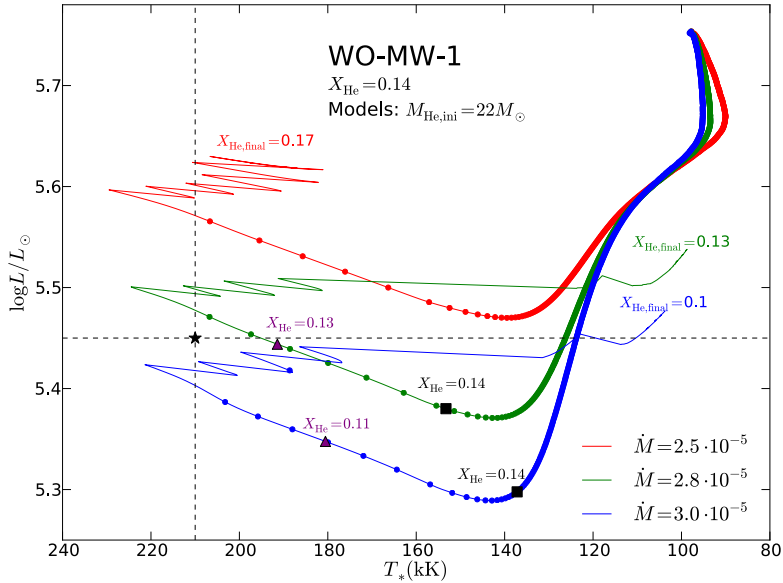


Figure 5.11: Hertzsprung-Russell diagram with evolutionary models for WO-MW-1, which start with a helium star. The best-fit parameters for WO-MW-1 are indicated. The different tracks correspond to different mass-loss rates. The dots indicate 1000 year time steps.

tative for our stars. We mitigate this by adopting a constant mass-loss rate throughout the evolution. We explore combinations of the mass-loss rate and initial helium star mass to reproduce the observed surface helium abundance, temperature and luminosity.

Figure 5.11 shows the stellar evolutionary tracks for WO-MW-1 in the HRD, computed with an initial helium mass of $M_{\text{He,ini}} = 22M_{\odot}$ and three values for the mass-loss rate. These were the best-fit models for the observed helium mass fraction, luminosity and temperature. Other combinations of initial helium-star masses and mass-loss rates were explored but they were not in as good agreement with the observed stellar parameters. The surface mass fractions of helium (normalized to $X_{\text{He}} + X_{\text{C}} + X_{\text{O}} = 1$) during the late evolutionary stages are indicated along the tracks. Models for the other WO stars are shown in Appendix B.5.

The models spend most of their lifetime close to the He-ZAMS. They lose mass as a consequence of the applied mass-loss rate causing the luminosity to drop during the core-helium burning phase. After core-helium exhaustion, the stars contract on their thermal timescale and become hotter and brighter. The models are hardly inflated at this stage of the evolution because the iron opacity peak (at $T \sim 200$ kK) which is responsible for inflation is only partially present in the stars. At some point during the overall contraction phase the helium-shell ignites and the tracks eventually turn

Table 5.6: Surface mass fractions, estimates of helium star mass and remaining lifetime, and constraints on the mass loss parameters.

ID	X_{He}	X_{C}	X_{O}	$M_{\text{He,ini}}$ (M_{\odot})	M_{final} (M_{\odot})	t_{SN} (yr)	\dot{M} ($M_{\odot}\text{yr}^{-1}$)	f_c
WO-MW-1	0.14	0.62	0.24	22.0	9.8	1 500	2.8×10^{-5}	> 0.4
WO-MW-2	0.26	0.54	0.21	17.0	8.8	2 000	1.7×10^{-5}	> 0.4
WO-MW-3	0.29	0.53	0.18	17.0	8.8	8 000	1.7×10^{-5}	> 0.3
WO-LMC-1	0.30	0.55	0.15	15.0	7.7	7 000	1.4×10^{-5}	> 0.3
WO-LMC-2	0.22	0.60	0.18	17.0	8.4	9 000	1.8×10^{-5}	> 0.4
WO-IC1613-1	0.44	0.46	0.10	23.0	15.4	17 000	1.8×10^{-5}	0.1

redwards because of the mirror principle (Kippenhahn & Weigert 1990). When the models become cooler, envelope inflation may again play a role. Since the models were computed until oxygen burning, they will not change their positions in the HRD significantly after the models stop, since the envelope structure does not change any further until the star explodes as a supernova.

The stellar tracks in Figure 5.11 that reproduce the observed stellar parameters do so after the models have exhausted the helium in their core (see also Langer et al. 1988; Langer 1989). In other words, according to our models WO-MW-1 is a post-core helium burning star and has a remaining lifetime of less than 2000 years. Furthermore, tracks with mass-loss rates lower than $\sim 2.7 \times 10^{-5} M_{\odot}\text{yr}^{-1}$ never reveal the layer that corresponds to the observed helium mass-fraction. Combined with the determined value of $\dot{M} / \sqrt{f_c}$, this constrains the volume filling factor to $f_c \geq 0.4$.

Table 5.6 gives the initial helium star mass, predicted remaining lifetime, and constraints on the clumping factor based on the calculated evolutionary models for all the stars. According to our models, all WO stars except for WO-IC1613-1 (which is close to the helium terminal-age main sequence) are in the core-contraction phase after core-helium burning. They are likely to explode in less than 10^4 years. The initial helium star masses are in the range $M_{\text{He,ini}} \sim 15 - 25 M_{\odot}$. This corresponds to the helium-core masses predicted for stars with an initial mass of $M_{\text{ini}} \sim 40 - 60 M_{\odot}$ (Ekström et al. 2012). However, only the models with very rapid rotation (40 % of critical, Figure 5.7) reach the He-ZAMS and hotter, while non-rotating models are still covered by a hydrogen-rich envelope. As most massive stars are only modestly rotating (e.g., Ramírez-Agudelo et al. 2013), this may point to a much higher mass loss in stages prior to the WO phase.

When they end their lives, most of the WO stars have predicted masses below $10 M_{\odot}$. The supernovae will almost certainly be of type Ic, as the current fractions of helium at the surface are already too low to produce type Ib SN e (Dessart et al.

2011b). Although Sander et al. (2012) report on a very high rotational velocity for WO-MW-1 and 2, we do not find any indication of rapid rotation for the WO stars. We can therefore not conclude on the possibility of the production of long-duration GRBs during core-collapse.

5.5.1 Progenitors of WO stars

As shown above, the likely progenitors of WO stars have an initial mass of $M_{\text{ini}} = 40 - 60M_{\odot}$. This is in very good agreement with the current view of massive star evolution, for instance as summarized by Langer (2012). The evolutionary sequence proposed by Sander et al. (2012) also predicts WO stars to be the descendants of stars with $M_{\text{ini}} = 45 - 60M_{\odot}$.

Groh et al. (2014) calculated synthetic spectra at several stages in the evolution of a $60M_{\odot}$ star. Their model exhibits an early-type WO spectrum at the final stages of its life, but is much brighter than the observed WO stars.

As mentioned before, single-star evolutionary tracks that start from the ZAMS cannot reproduce most of the WO stars. However, the evolutionary path of massive stars and the mass-loss rates at each of the various stages of evolution are highly uncertain. In particular, whether a star undergoes an luminous blue variable (LBV) phase, and how much mass is lost during that phase, is currently poorly understood. The question is therefore how the naked helium stars that are needed to explain the WO phenomena are formed. While some may indeed originate from single-star evolution, it may be expected that binary interactions will play a role for most of them (Sana et al. 2012).

Binary interactions can produce a helium star in two ways. First, the star could be the initially most massive star in a binary system. In this case it might strip its envelope by transferring mass to a massive companion. The hydrogen-rich material would rejuvenate the companion star, making it appear younger (e.g., de Mink et al. 2014; Schneider et al. 2014). While this scenario might be appropriate for the two WO stars that are in a binary with an O-star companion, the single WO stars that are discussed in this paper show no signs of a massive companion. However, they might have lost their hydrogen envelope in a common envelope interaction with an intermediate mass companion. In that case, this companion star is expected to still orbit the WO star.

An interesting alternative scenario originates from the spatial distribution of LBV stars, which are predominantly located outside of clusters (Smith & Tombleson 2014). These authors speculate that the LBVs may have been part of a binary system in which they were the mass gainer. Their relative isolation may then be the result of the supernova kick when the primary star explodes. Qualitatively, this is in agreement with the spatial location of the WO stars, which are predominantly (5 out of

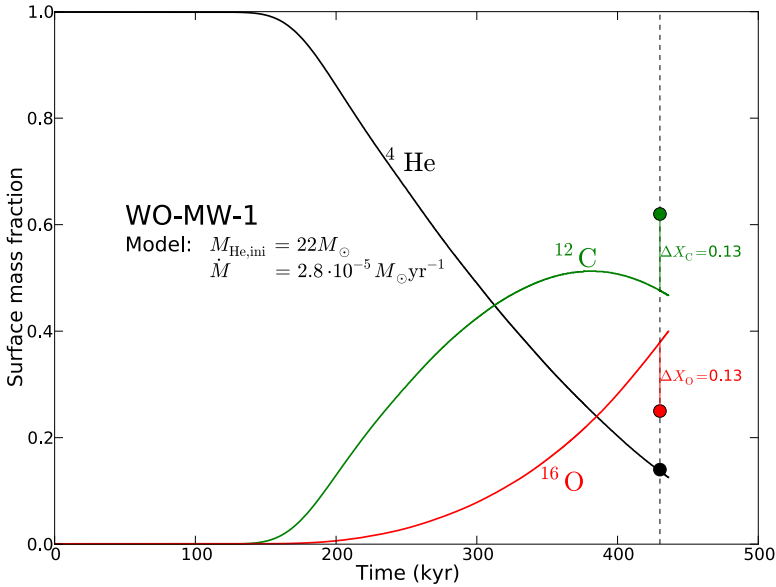


Figure 5.12: Evolution of the surface mass fractions in the helium star model of WO-LMC-1 since the onset of core-helium burning. The observed mass fractions of helium, carbon, and oxygen are indicated. The model overpredicts the $X_{\text{O}}/X_{\text{C}}$ ratio.

9) isolated. Regardless whether it is triggered by binary interactions, the LBV phenomenon could explain the loss of the large amount of mass that is needed to reveal the core at the onset of helium burning (Langer et al. 1994).

5.5.2 The $^{12}\text{C}(\alpha, \gamma)^{16}\text{O}$ thermonuclear cross-section

Apart from constraining the lifetime of the WO stars, the observed surface abundances can be used to constrain the illusive $^{12}\text{C}(\alpha, \gamma)^{16}\text{O}$ thermonuclear reaction rate. The currently used value (0.632 times that of Caughlan et al. 1985) is based on the solar abundance pattern between oxygen and calcium, but has an uncertainty of about 30% (Weaver & Woosley 1993). Deviations of this rate strongly influence the supernova yields as well as the pre-supernova evolution (Tur et al. 2007). With their surface abundances corresponding to the core abundances far into the helium-burning stage, WO stars offer a unique opportunity to provide direct constrains on the nuclear reaction rate. Figure 5.12 shows the helium, carbon, and oxygen surface mass fractions as a function of time for the helium star model of WO-MW-1. When compared to the observed mass fractions, it is clear that the model overpredicts the oxygen-to-carbon ratio. This indicates that the actual $^{12}\text{C}(\alpha, \gamma)^{16}\text{O}$ reaction rate must be lower than the value that is currently being used. Placing more firm constraints on

this reaction rate will be the focus of a separate study.

5.6 Summary and conclusions

In this paper we have presented a detailed spectroscopic analysis of single WO stars. We have constrained the evolutionary status of the sources using tailored evolutionary models. For the stellar properties we find that:

- WO stars are extremely hot, with temperatures ranging from 150 kK up to 210 kK. In the Hertzsprung-Russell diagram they are located at the hot side of the helium zero-age main sequence.
- The helium surface mass fraction is typically 20-30%, but ranges from 44% for the coolest star to as low as 14% for the hottest star. The oxygen mass fractions reach values up to 25%.
- The stars loose mass at a rate of $0.8 - 1.5 \times 10^{-5} M_{\odot} \text{ yr}^{-1}$, which is higher by a factor of about 2-3 than suggested by the predictions by Nugis & Lamers (2000).
- The surface abundances of WO stars correspond to material that was formed very late into the core helium-burning stage, and the stars must have experienced severe mass loss during this stage to reveal the observed layers. This translates to strict constraints on the volume filling factor of the wind medium, requiring $f_c > 0.3$ for most of the stars.

The derived properties of the WO stars can be reproduced for helium stars with $M_{\text{He,ini}} \sim 15 - 25 M_{\odot}$, and suggest initial masses of $M_{\text{ini}} \sim 40 - 60 M_{\odot}$. Their extremely high temperatures are consistent with the contraction of the star after it exhausts the helium in its core. Together with the low surface helium abundances, this firmly establishes that WO stars are post core-helium burning massive stars. They will likely explode as type Ic supernovae in $10^3 - 10^4$ years. Thus, the WO class indeed represents a short, final stage in the evolution of massive stars.

Acknowledgments

We thank Bram Ochsendorf and Bertrand Lemaisle for executing part of the observations. This research has made use of the SIMBAD database, operated at CDS, Strasbourg, France

- Aoki, W., Tominaga, N., Beers, T. C., Honda, S., & Lee, Y. S. 2014, *Science*, 345, 912
- Armandroff, T. E. & Massey, P. 1991, *AJ*, 102, 927
- Asplund, M., Grevesse, N., Sauval, A. J., & Scott, P. 2009, *ARA&A*, 47, 481
- Baldwin, J. A., Ferland, G. J., Martin, P. G., et al. 1991, *ApJ*, 374, 580
- Baraffe, I., Heger, A., & Woosley, S. E. 2001, *ApJ*, 550, 890
- Barlow, M. J. & Hummer, D. G. 1982, in *IAU Symposium*, Vol. 99, *Wolf-Rayet Stars: Observations, Physics, Evolution*, ed. C. W. H. De Loore & A. J. Willis, 387–392
- Böhm-Vitense, E. 1958, *ZAp*, 46, 108
- Bonanos, A. Z. 2013, in *IAU Symposium*, Vol. 289, *IAU Symposium*, ed. R. de Grijs, 173–178
- Bresolin, F., Crowther, P. A., & Puls, J., eds. 2008, *IAU Symposium*, Vol. 250, *Massive Stars as Cosmic Engines*
- Bresolin, F., Gieren, W., Kudritzki, R.-P., et al. 2009, *ApJ*, 700, 309
- Bresolin, F., Pietrzyński, G., Urbaneja, M. A., et al. 2006, *ApJ*, 648, 1007
- Bresolin, F., Urbaneja, M. A., Gieren, W., Pietrzyński, G., & Kudritzki, R.-P. 2007, *ApJ*, 671, 2028
- Brott, I., de Mink, S. E., Cantiello, M., et al. 2011, *A&A*, 530, A115
- Cantiello, M. & Braithwaite, J. 2011, *A&A*, 534, A140
- Cantiello, M., Langer, N., Brott, I., et al. 2009, *A&A*, 499, 279
- Cardelli, J. A., Clayton, G. C., & Mathis, J. S. 1989, *ApJ*, 345, 245
- Castelli, F. & Kurucz, R. L. 2004, *ArXiv Astrophysics e-prints*
- Castor, J. I., Abbott, D. C., & Klein, R. I. 1975, *ApJ*, 195, 157
- Castro, N., Herrero, A., Garcia, M., et al. 2008, *A&A*, 485, 41
- Caughtlan, G. R., Fowler, W. A., Harris, M. J., & Zimmerman, B. A. 1985, *Atomic Data and Nuclear Data Tables*, 32, 197
- Charbonneau, P. 1995, *ApJS*, 101, 309
- Cole, A. A., Tolstoy, E., Gallagher, III, J. S., et al. 1999, *AJ*, 118, 1657
- Crowther, P. A., De Marco, O., & Barlow, M. J. 1998, *MNRAS*, 296, 367

BIBLIOGRAPHY

- Crowther, P. A., Dessart, L., Hillier, D. J., Abbott, J. B., & Fullerton, A. W. 2002, *A&A*, 392, 653
- Crowther, P. A., Fullerton, A. W., Hillier, D. J., et al. 2000, *ApJ*, 538, L51
- Crowther, P. A. & Hadfield, L. J. 2006, *A&A*, 449, 711
- Crowther, P. A., Morris, P. W., & Smith, J. D. 2006, *ApJ*, 636, 1033
- Davidge, T. J. 1993, *AJ*, 105, 1392
- Davidson, K. & Kinman, T. D. 1982, *PASP*, 94, 634
- de Koter, A., Heap, S. R., & Hubeny, I. 1997, *ApJ*, 477, 792
- De Marco, O., Schmutz, W., Crowther, P. A., et al. 2000, *A&A*, 358, 187
- de Mink, S. E., Langer, N., Izzard, R. G., Sana, H., & de Koter, A. 2013, *ApJ*, 764, 166
- de Mink, S. E., Sana, H., Langer, N., Izzard, R. G., & Schneider, F. R. N. 2014, *ApJ*, 782, 7
- Dessart, L., Crowther, P. A., Hillier, D. J., et al. 2000, *MNRAS*, 315, 407
- Dessart, L., Hillier, D. J., Livne, E., et al. 2011a, *MNRAS*, 414, 2985
- Dessart, L., Hillier, D. J., Livne, E., et al. 2011b, *MNRAS*, 414, 2985
- D'Odorico, S. & Rosa, M. 1982, *A&A*, 105, 410
- Donati, J.-F. & Landstreet, J. D. 2009, *ARA&A*, 47, 333
- Drew, J. E., Barlow, M. J., Unruh, Y. C., et al. 2004, *MNRAS*, 351, 206
- Ekström, S., Georgy, C., Eggenberger, P., et al. 2012, *A&A*, 537, A146
- Eldridge, J. J., Fraser, M., Smartt, S. J., Maund, J. R., & Crockett, R. M. 2013, *ArXiv e-prints*
- Evans, C. J., Bresolin, F., Urbaneja, M. A., et al. 2007, *ApJ*, 659, 1198
- Ferland, G. J., Porter, R. L., van Hoof, P. A. M., et al. 2013, *Rev. Mexicana Astron. Astrofis.*, 49, 137
- Fitzpatrick, E. L. 1999, *PASP*, 111, 63
- Gal-Yam, A., Arcavi, I., Ofek, E. O., et al. 2014, *Nature*, 509, 471
- Garcia, M. & Herrero, A. 2013, *A&A*, 551, A74
- Garcia, M., Herrero, A., Najarro, F., Lennon, D. J., & Urbaneja, M. A. 2014, *ArXiv e-prints*
- Garcia, M., Herrero, A., Vicente, B., et al. 2009, *A&A*, 502, 1015
- Garnett, D. R., Kennicutt, Jr., R. C., Chu, Y.-H., & Skillman, E. D. 1991, *ApJ*, 373, 458
- Georgy, C., Meynet, G., Walder, R., Folini, D., & Maeder, A. 2009, *A&A*, 502, 611
- Gibson, B. K. 2000, *Mem. Soc. Astron. Italiana*, 71, 693
- Gräfener, G. & Hamann, W.-R. 2005, *A&A*, 432, 633
- Gräfener, G. & Hamann, W.-R. 2008, *A&A*, 482, 945
- Gräfener, G., Hamann, W.-R., Hillier, D. J., & Koesterke, L. 1998, *A&A*, 329, 190
- Gräfener, G., Koesterke, L., & Hamann, W.-R. 2002, *A&A*, 387, 244

- Gräfener, G., Owocki, S. P., & Vink, J. S. 2012, *A&A*, 538, A40
- Gräfener, G. & Vink, J. S. 2013, *A&A*, 560, A6
- Gräfener, G., Vink, J. S., de Koter, A., & Langer, N. 2011, *A&A*, 535, A56
- Groenewegen, M. A. T., Lamers, H. J. G. L. M., & Pauldrach, A. W. A. 1989, *A&A*, 221, 78
- Groh, J. H., Meynet, G., Ekström, S., & Georgy, C. 2014, *A&A*, 564, A30
- Haiman, Z. & Loeb, A. 1997, *ApJ*, 483, 21
- Hainich, R., Rühling, U., Todt, H., et al. 2014, *A&A*, 565, A27
- Hamann, W.-R. & Koesterke, L. 1998, *A&A*, 335, 1003
- Hamann, W.-R., Koesterke, L., & Wessolowski, U. 1995, *A&A*, 299, 151
- Hartoog, O. E., Sana, H., de Koter, A., & Kaper, L. 2012, *MNRAS*, 422, 367
- Heger, A., Jeannin, L., Langer, N., & Baraffe, I. 1997, *A&A*, 327, 224
- Henrichs, H. F. 1999, in *Lecture Notes in Physics*, Berlin Springer Verlag, Vol. 523, IAU Colloq. 169: Variable and Non-spherical Stellar Winds in Luminous Hot Stars, ed. B. Wolf, O. Stahl, & A. W. Fullerton, 304
- Herrero, A., Garcia, M., Puls, J., et al. 2012, *A&A*, 543, A85
- Herrero, A., Garcia, M., Uytterhoeven, K., et al. 2011, in *IAU Symposium*, Vol. 272, IAU Symposium, ed. C. Neiner, G. Wade, G. Meynet, & G. Peters, 292–293
- Hillier, D. J. & Miller, D. L. 1998, *ApJ*, 496, 407
- Hillier, D. J. & Miller, D. L. 1999, *ApJ*, 519, 354
- Hosek, Jr., M. W., Kudritzki, R.-P., Bresolin, F., et al. 2014, *ApJ*, 785, 151
- Humphreys, R. M. & Davidson, K. 1994, *PASP*, 106, 1025
- Iglesias, C. A., Rogers, F. J., & Wilson, B. G. 1992, *ApJ*, 397, 717
- Ishii, M., Ueno, M., & Kato, M. 1999, *PASJ*, 51, 417
- Kehrig, C., Oey, M. S., Crowther, P. A., et al. 2011, *A&A*, 526, A128
- Kingsburgh, R. L. & Barlow, M. J. 1995, *A&A*, 295, 171
- Kingsburgh, R. L., Barlow, M. J., & Storey, P. J. 1995, *A&A*, 295, 75
- Kippenhahn, R. & Weigert, A. 1990, *Stellar Structure and Evolution*
- Kudritzki, R. P. 2002, *ApJ*, 577, 389
- Kudritzki, R. P., Pauldrach, A., & Puls, J. 1987, *A&A*, 173, 293
- Kudritzki, R.-P. & Puls, J. 2000, *ARA&A*, 38, 613
- Lamers, H. J. G. L. M. & Nugis, T. 2002, *A&A*, 395, L1
- Lamers, H. J. G. L. M., Snow, T. P., & Lindholm, D. M. 1995, *ApJ*, 455, 269
- Langer, N. 1989, *A&A*, 210, 93
- Langer, N. 2012, *ARA&A*, 50, 107
- Langer, N., Hamann, W.-R., Lennon, M., et al. 1994, *A&A*, 290, 819
- Langer, N., Kiriakidis, M., El Eid, M. F., Fricke, K. J., & Weiss, A. 1988, *A&A*, 192, 177
- Langer, N., Norman, C. A., de Koter, A., et al. 2007, *A&A*, 475, L19

BIBLIOGRAPHY

- Larson, R. B. 1998, *MNRAS*, 301, 569
- Leitherer, C., Robert, C., & Drissen, L. 1992, *ApJ*, 401, 596
- Lequeux, J., Peimbert, M., Rayo, J. F., Serrano, A., & Torres-Peimbert, S. 1979, *A&A*, 80, 155
- Levesque, E. M. & Massey, P. 2012, *AJ*, 144, 2
- Lucy, L. B. 2012, *A&A*, 543, A18
- Lucy, L. B. & Solomon, P. M. 1967, *AJ*, 72, 310
- Lucy, L. B. & Solomon, P. M. 1970, *ApJ*, 159, 879
- Madau, P. & Rees, M. J. 2001, *ApJ*, 551, L27
- Maeder, A. 1983, *A&A*, 120, 113
- Maeder, A. & Meynet, G. 2000, *A&A*, 361, 159
- Martins, F., Hillier, D. J., Paumard, T., et al. 2008, *A&A*, 478, 219
- Martins, F., Schaerer, D., & Hillier, D. J. 2005, *A&A*, 436, 1049
- Mason, B. D., Hartkopf, W. I., Gies, D. R., Henry, T. J., & Helsel, J. W. 2009, *AJ*, 137, 3358
- Massey, P., Bresolin, F., Kudritzki, R. P., Puls, J., & Pauldrach, A. W. A. 2004, *ApJ*, 608, 1001
- Massey, P., Neugent, K. F., Morrell, N., & Hillier, D. J. 2014, *ApJ*, 788, 83
- Massey, P., Puls, J., Pauldrach, A. W. A., et al. 2005, *ApJ*, 627, 477
- Massey, P., Waterhouse, E., & DeGioia-Eastwood, K. 2000, *AJ*, 119, 2214
- Massey, P., Zangari, A. M., Morrell, N. I., et al. 2009, *ApJ*, 692, 618
- McConnachie, A. W. 2012, *AJ*, 144, 4
- Meynet, G. & Maeder, A. 2003, *A&A*, 404, 975
- Meynet, G. & Maeder, A. 2005, *A&A*, 429, 581
- Micic, M., Holley-Bockelmann, K., & Sigurdsson, S. 2011, *MNRAS*, 414, 1127
- Minniti, D. & Zijlstra, A. A. 1997, *AJ*, 114, 147
- Minniti, D., Zijlstra, A. A., & Alonso, M. V. 1999, *AJ*, 117, 881
- Modigliani, A., Goldoni, P., Royer, F., et al. 2010, in *Society of Photo-Optical Instrumentation Engineers (SPIE) Conference Series*, Vol. 7737, *Society of Photo-Optical Instrumentation Engineers (SPIE) Conference Series*
- Moffat, A. F. J. & Seggewiss, W. 1984, *A&AS*, 58, 117
- Mokiem, M. R., de Koter, A., Evans, C. J., et al. 2006, *A&A*, 456, 1131
- Mokiem, M. R., de Koter, A., Puls, J., et al. 2005, *A&A*, 441, 711
- Mokiem, M. R., de Koter, A., Vink, J. S., et al. 2007, *A&A*, 473, 603
- Mokiem, M. R., Martín-Hernández, N. L., Lenorzer, A., de Koter, A., & Tielens, A. G. G. M. 2004, *A&A*, 419, 319
- Morton, D. C. 1966, *AJ*, 71, 172
- Mujres, L. E., Vink, J. S., de Koter, A., Müller, P. E., & Langer, N. 2012, *A&A*, 537, A37

- Neugent, K. F., Massey, P., & Morrell, N. 2012, *AJ*, 144, 162
- Nomoto, K., Tanaka, M., Tominaga, N., & Maeda, K. 2010, *New A Rev.*, 54, 191
- Nugis, T. & Lamers, H. J. G. L. M. 2000, *A&A*, 360, 227
- Nugis, T. & Lamers, H. J. G. L. M. 2002, *A&A*, 389, 162
- O'Donnell, J. E. 1994, *ApJ*, 422, 158
- Osterbrock, D. E. & Ferland, G. J. 2006, *Astrophysics of gaseous nebulae and active galactic nuclei*
- Osterbrock, D. E., Tran, H. D., & Veilleux, S. 1992, *ApJ*, 389, 305
- Pagel, B. E. J., Edmunds, M. G., Blackwell, D. E., Chun, M. S., & Smith, G. 1979, *MNRAS*, 189, 95
- Pagel, B. E. J., Simonson, E. A., Terlevich, R. J., & Edmunds, M. G. 1992, *MNRAS*, 255, 325
- Petrovic, J., Pols, O., & Langer, N. 2006, *A&A*, 450, 219
- Pietrzyński, G., Gieren, W., Soszyński, I., et al. 2006, *ApJ*, 642, 216
- Pilyugin, L. S. & Thuan, T. X. 2005, *ApJ*, 631, 231
- Press, W. H., Flannery, B. P., & Teukolsky, S. A. 1986, *Numerical recipes. The art of scientific computing*
- Puls, J., Urbaneja, M. A., Venero, R., et al. 2005, *A&A*, 435, 669
- Puls, J., Vink, J. S., & Najarro, F. 2008, *A&A Rev.*, 16, 209
- Rafelski, M., Wolfe, A. M., Prochaska, J. X., Neeleman, M., & Mendez, A. J. 2012, *ApJ*, 755, 89
- Ramírez-Agudelo, O. H., Simón-Díaz, S., Sana, H., et al. 2013, *A&A*, 560, A29
- Rubin, R. H., Dufour, R. J., & Walter, D. K. 1993, *ApJ*, 413, 242
- Rubin, R. H., Simpson, J. P., Haas, M. R., & Erickson, E. F. 1991, *ApJ*, 374, 564
- Salpeter, E. E. 1955, *ApJ*, 121, 161
- Sana, H., de Koter, A., de Mink, S. E., et al. 2013, *A&A*, 550, A107
- Sana, H., de Mink, S. E., de Koter, A., et al. 2012, *Science*, 337, 444
- Sana, H. & Evans, C. J. 2011, in *IAU Symposium, Vol. 272*, IAU Symposium, ed. C. Neiner, G. Wade, G. Meynet, & G. Peters, 474–485
- Sana, H., Rauw, G., & Gosset, E. 2001, *A&A*, 370, 121
- Sander, A., Hamann, W.-R., & Todt, H. 2012, *A&A*, 540, A144
- Sanduleak, N. 1971, *ApJ*, 164, L71
- Schlegel, D. J., Finkbeiner, D. P., & Davis, M. 1998, *ApJ*, 500, 525
- Schmutz, W. 1997, *A&A*, 321, 268
- Schmutz, W., Hamann, W.-R., & Wessolowski, U. 1989, *A&A*, 210, 236
- Schneider, F. R. N., Izzard, R. G., de Mink, S. E., et al. 2014, *ApJ*, 780, 117
- Skillman, E. D., Hidalgo, S. L., Weisz, D. R., et al. 2014, *ApJ*, 786, 44
- Smartt, S. J., Crowther, P. A., Dufton, P. L., et al. 2001, *MNRAS*, 325, 257
- Smith, L. F. & Maeder, A. 1991, *A&A*, 241, 77

BIBLIOGRAPHY

- Smith, N. & Tombleson, R. 2014, ArXiv e-prints
- Smith, N., Vink, J. S., & de Koter, A. 2004, ApJ, 615, 475
- Soszyński, I., Gieren, W., Pietrzyński, G., et al. 2006, ApJ, 648, 375
- Stevens, I. R., Blondin, J. M., & Pollock, A. M. T. 1992, ApJ, 386, 265
- Syphers, D. & Shull, J. M. 2013, ApJ, 765, 119
- Tautvaišienė, G., Geisler, D., Wallerstein, G., et al. 2007, AJ, 134, 2318
- Tolstoy, E., Hill, V., & Tosi, M. 2009, ARA&A, 47, 371
- Tramper, F., Gräfener, G., Hartoog, O. E., et al. 2013, A&A, 559, A72
- Tramper, F., Sana, H., de Koter, A., & Kaper, L. 2011, ApJ, 741, L8
- Tremonti, C. A., Heckman, T. M., Kauffmann, G., et al. 2004, ApJ, 613, 898
- Tur, C., Heger, A., & Austin, S. M. 2007, ApJ, 671, 821
- Tur, C., Wuosmaa, A., Austin, S. M., et al. 2006, in APS Division of Nuclear Physics Meeting Abstracts, C3
- Urbaneja, M. A., Kudritzki, R.-P., Bresolin, F., et al. 2008, ApJ, 684, 118
- Venn, K. A., Tolstoy, E., Kaufer, A., et al. 2003, AJ, 126, 1326
- Vernet, J., Dekker, H., D'Odorico, S., et al. 2011, A&A, 536, A105
- Vink, J. S. & de Koter, A. 2005, A&A, 442, 587
- Vink, J. S., de Koter, A., & Lamers, H. J. G. L. M. 2000, A&A, 362, 295
- Vink, J. S., de Koter, A., & Lamers, H. J. G. L. M. 2001, A&A, 369, 574
- Vink, J. S. & Gräfener, G. 2012, ApJ, 751, L34
- Vink, J. S., Muijres, L. E., Anthonisse, B., et al. 2011, A&A, 531, A132
- Weaver, T. A. & Woosley, S. E. 1993, Phys. Rep., 227, 65
- Woosley, S. E. & Bloom, J. S. 2006, ARA&A, 44, 507
- Yoon, S.-C. & Cantiello, M. 2010, ApJ, 717, L62
- Yoon, S.-C., Gräfener, G., Vink, J. S., Kozyreva, A., & Izzard, R. G. 2012, A&A, 544, L11
- Yoon, S.-C. & Langer, N. 2005, A&A, 443, 643
- Yoon, S.-C., Langer, N., & Norman, C. 2006, A&A, 460, 199
- Zaritsky, D., Kennicutt, Jr., R. C., & Huchra, J. P. 1994, ApJ, 420, 87

Best-fit O star models

The figures in this appendix show the best-fit line profiles for each of the stars in chapter 5. Each subplot belongs to a spectral line that is used in the fit. The vertical dashed lines indicate the boundary wavelengths of the fit. The observed data is indicated with the black dots, the best-fit line profiles with the red lines.

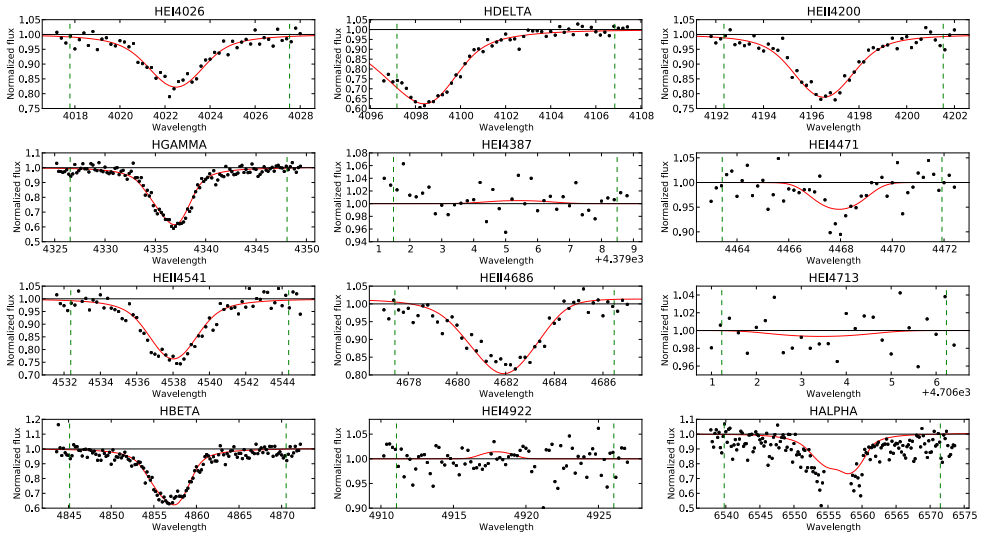


Figure A.1: Best-fit line profiles for IC1613-1.

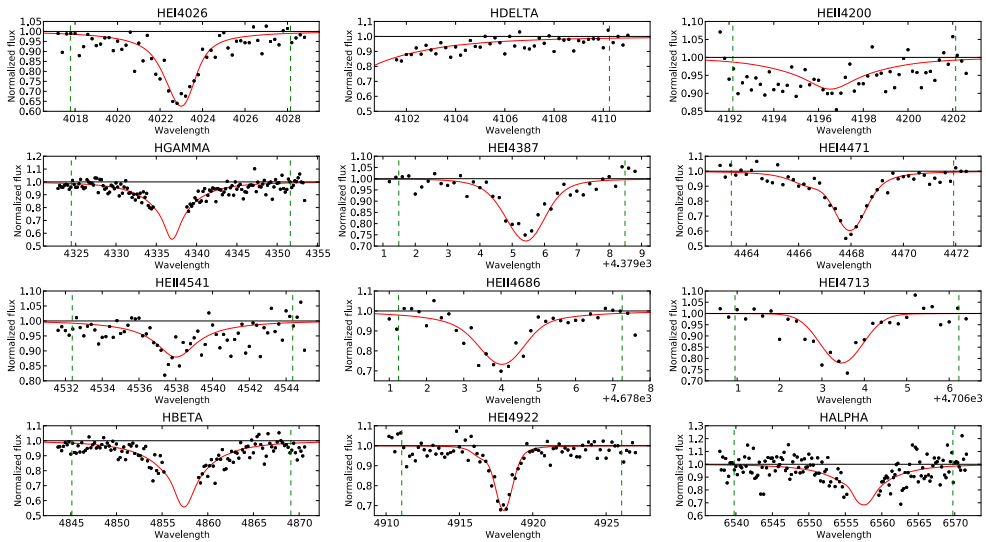


Figure A.2: Best-fit line profiles for IC1613-2.

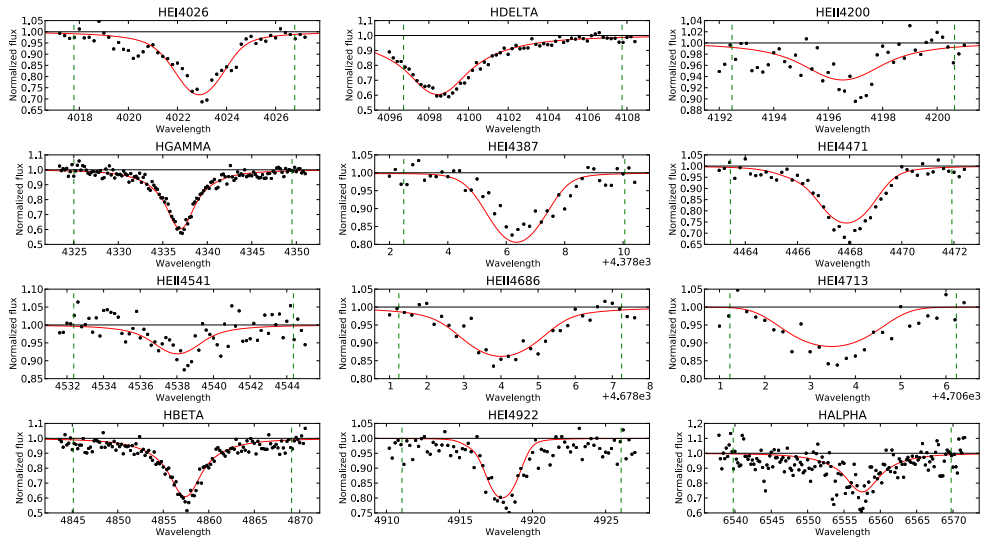


Figure A.3: Best-fit line profiles for IC1613-3.

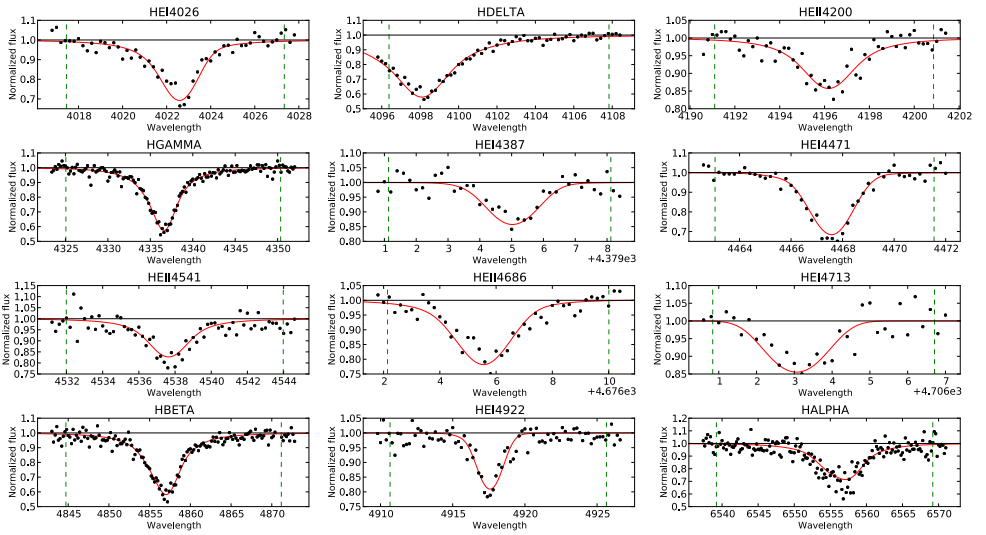


Figure A.4: Best-fit line profiles for IC1613-4.

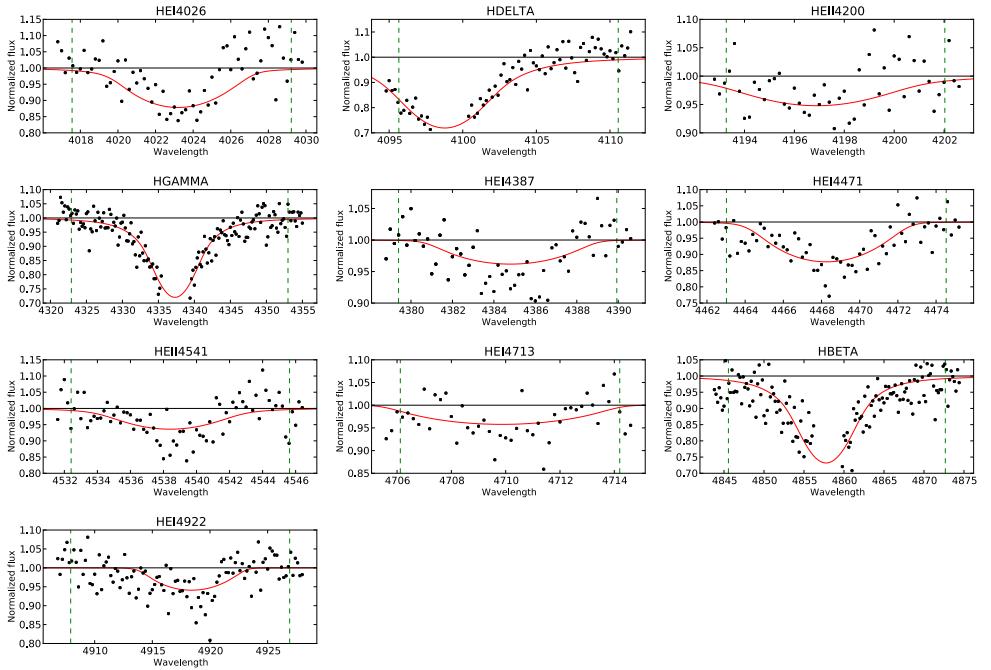


Figure A.5: Best-fit line profiles for IC1613-5.

A Best-fit O star models

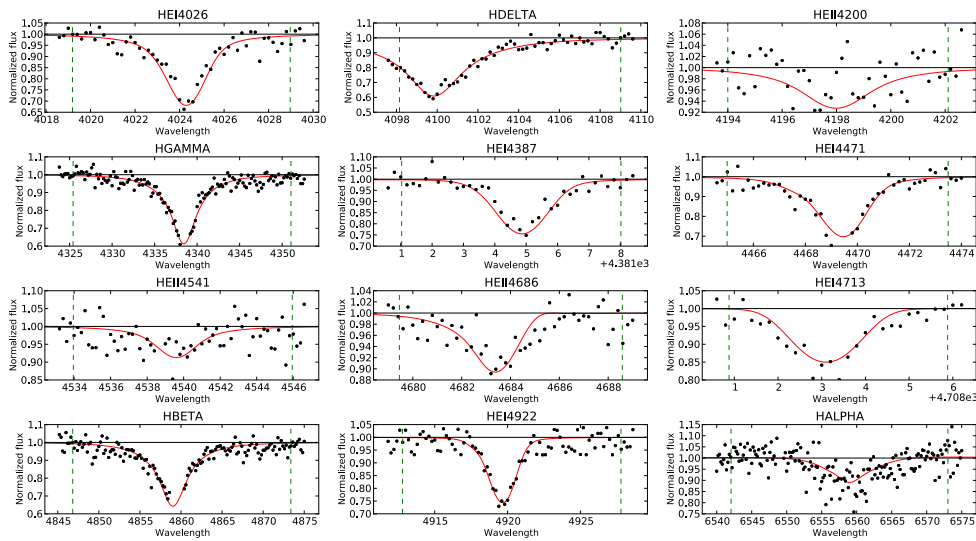


Figure A.6: Best-fit line profiles for WLM-1.

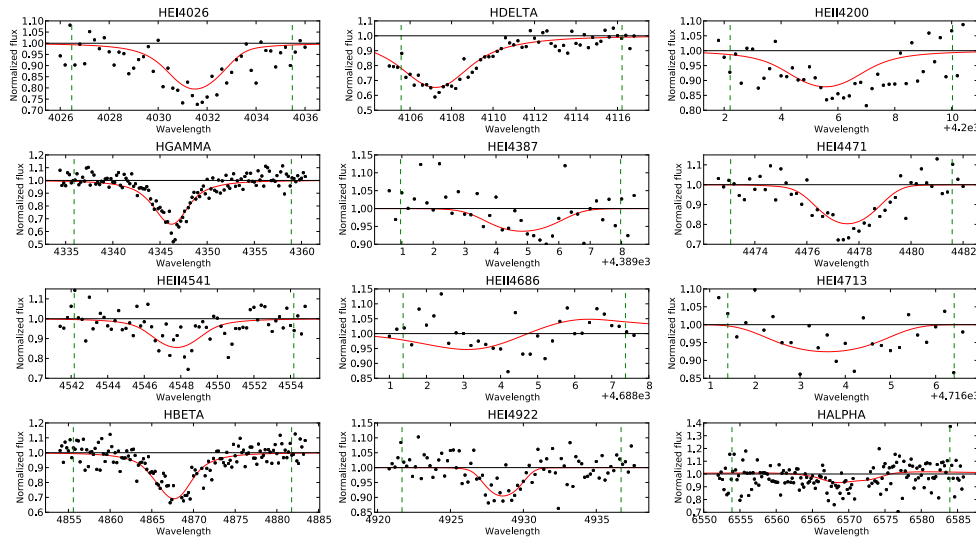


Figure A.7: Best-fit line profiles for NGC3109-1.

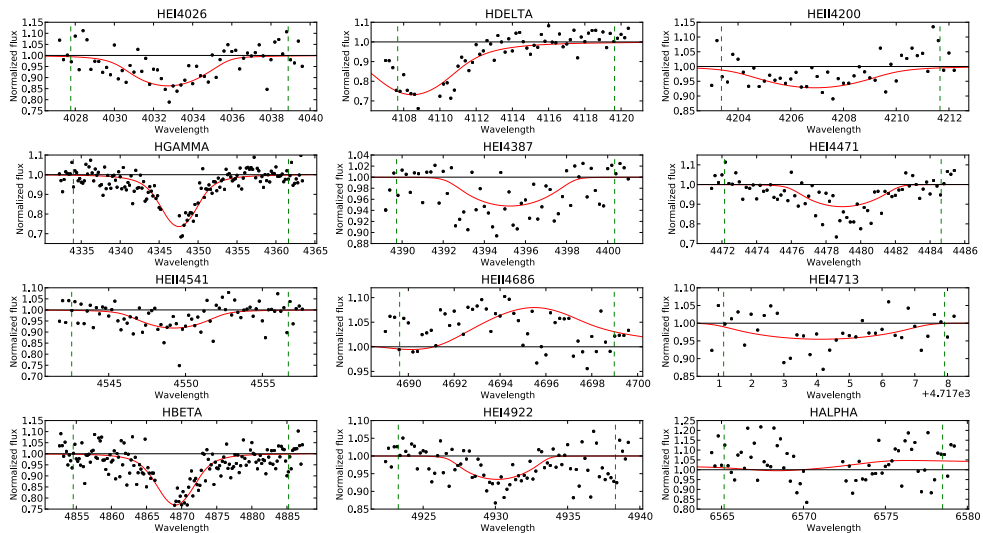


Figure A.8: Best-fit line profiles for NGC3109-2.

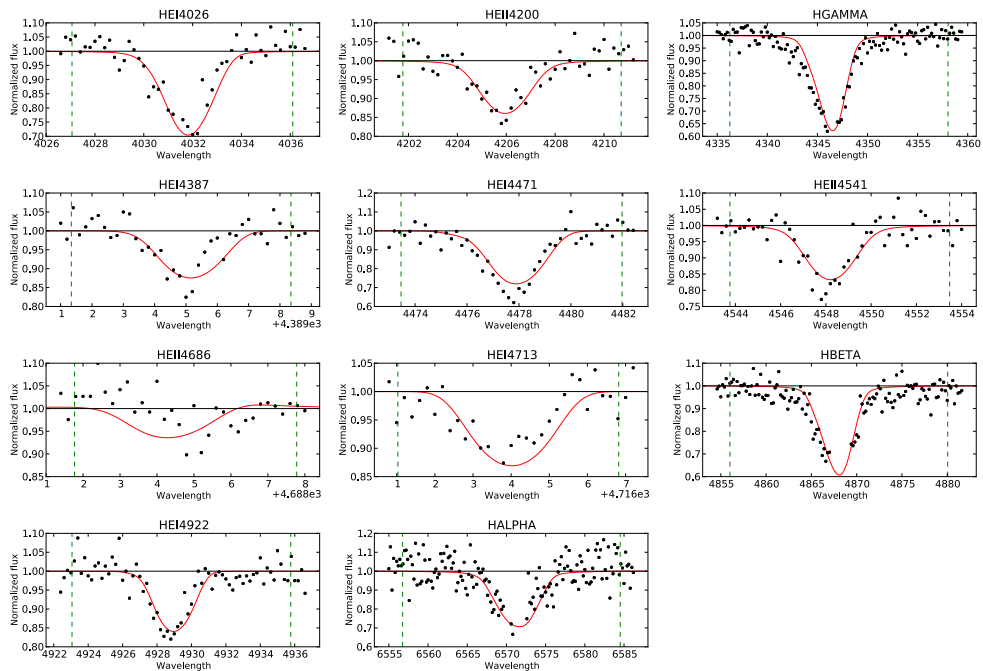


Figure A.9: Best-fit line profiles for NGC3109-3.

A Best-fit O star models

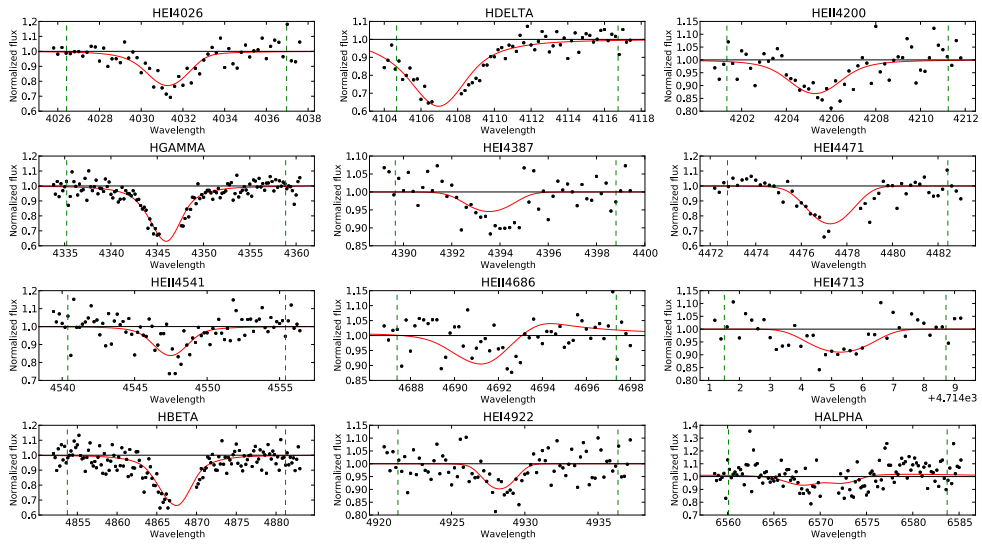


Figure A.10: Best-fit line profiles for NGC3109-4.

B.1 Flux correction WO-LMC-2

As discussed in Section 5.2, the slope of the spectrum of WO-LMC-2 before extinction correction is steeper than that of WO star models for an LMC metallicity. This may either be a result of a bad flux calibration, or a second object may be contaminating the spectrum. Inspection of a *Hubble Space Telescope* (HST) near-UV image shows that there is indeed a faint star very close to WO-LMC-2 (Figure B.1). We therefore first tried to correct the spectrum by assuming this object is responsible for the steep slope.

We assume that the flux contribution of the contaminating object follows the Rayleigh-Jeans approximation ($F \propto \lambda^{-4}$) at the X-Shooter wavelength range. This seems justified, as the slope of the uncorrected spectrum is steeper than the slope of the continuum of an LMC WO-model (which has a free-free emission component and is less-steep than a Rayleigh-Jeans slope) even before dereddening.

As we cannot determine the reddening from our spectrum, we use the average value for the region found by Massey et al. (2005) of $A_V = 0.4$ and a standard total-to-selective extinction of $R_V = 3.1$. We assume a luminosity of 1.8×10^5 for the WO star, equal to that of WO-LMC-1. While there is no a-priori reason for the two stars to have the same luminosity, the resulting model flux is in agreement with the dereddened flux in the near-IR region where the contribution of the contaminator becomes negligible.

The correction is then done by testing different ratios of the flux contributed by the WO and the contaminator. Ideally, the flux ratio measured from photometry should be used. However, the only image where the individual stars are resolved is the HST/WFC3 image shown in Figure B.1, which uses a filter with an effective wavelength in the near-UV. From this image, the flux ratio is $F_{\text{cont}}/F_{\text{WO}} = 0.1$ at 2250Å. As a much higher flux ratio is needed to recover the observed spectrum, this

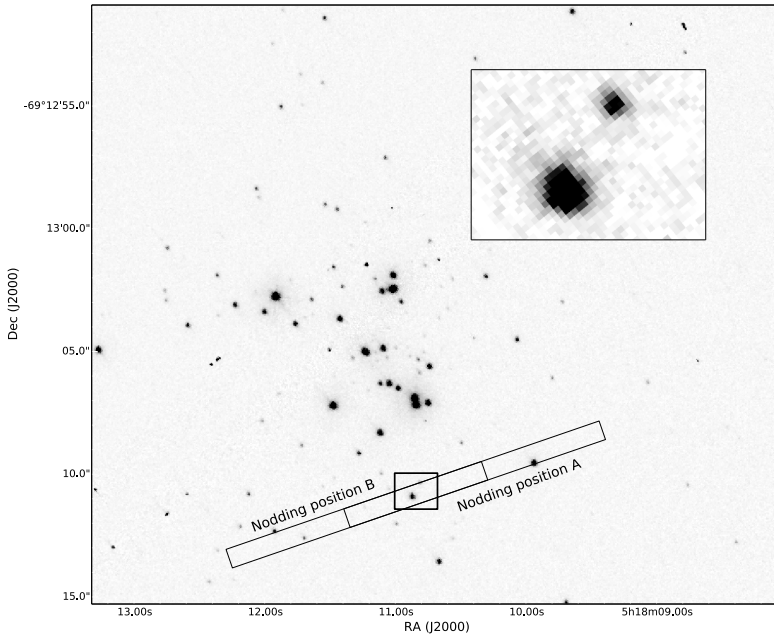


Figure B.1: Archival HST/WFC3 image of WO-LMC-2 (F225W filter, proposal ID 12940, PI Massey). North is up and East to the left. The two X-Shooter slit positions are indicated. The inset shows a zoomed image of the boxed area around WO-LMC-2, and shows the nearby star that may be contaminating the spectrum.

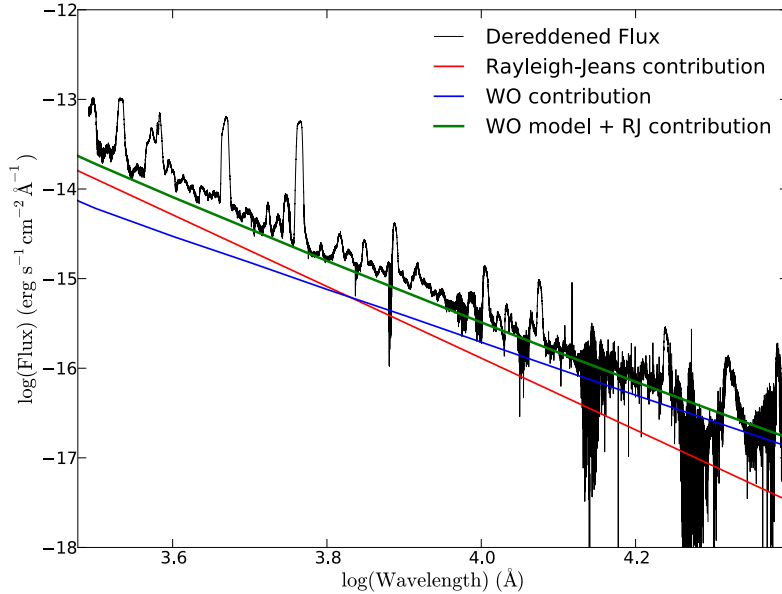


Figure B.2: Determination of the flux contribution of the companion of WO-LMC-2. Plotted are the dereddened flux (black), the assumed LMC WO model continuum (blue), the derived Rayleigh-Jeans contribution (red), and the combined continuum from the WO and Rayleigh-Jeans contributions (green).

indicates that the flux of the contaminating object peaks at a wavelength between 2250 \AA and the X-Shooter wavelengths (between $\sim 2500 - 3000 \text{ \AA}$), and no longer in the Rayleigh-Jeans tail. The contaminating object is therefore likely a B dwarf or giant. This means that the measured flux ratio can not be used to estimate the flux ratio in the X-Shooter wavelength range. Instead, we try out different combinations of flux ratios to obtain a combined spectrum of the WO model and a Rayleigh-Jeans contribution that matches the observed spectrum (Figure B.2.)

Using this strategy, we can get a good representation of the slope of the observed spectrum (Figure B.2). However, when the Rayleigh-Jeans contribution is subtracted from the observed spectrum, the emission lines become roughly twice as strong as in any of the other WO stars. As otherwise the spectrum of WO-LMC-2 does not show unusual features, we conclude that this is unlikely to be physical. We therefore assume that the steep slope is a result of the flux calibration, and not of contamination by the faint nearby object. We correct for this by artificially altering the slope to the correct value. While this results in a much more realistic spectrum, the luminosity and mass-loss rate that is derived from the modeling are much more uncertain than those of the other WO stars.

B.2 Best-fit models

The best-fit models for the WO stars presented in Chapter 5 are shown in Figures B.3 to B.7. In each of these Figures the observed flux is shown in red and the `CMFGEN` model in black. Prominent lines and best-fit parameters are indicated.

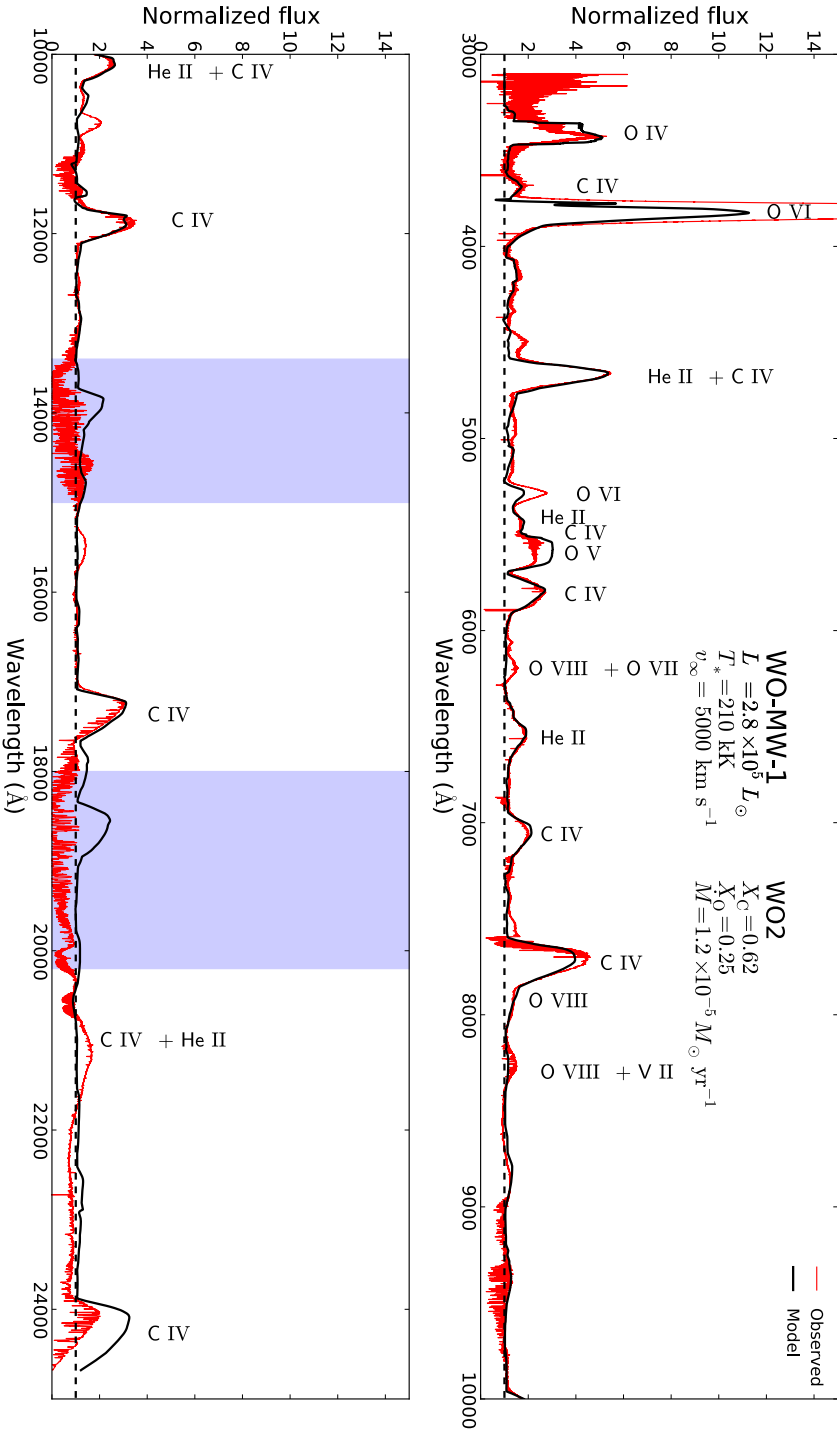


Figure B.3: Best model of WO-MW-1.

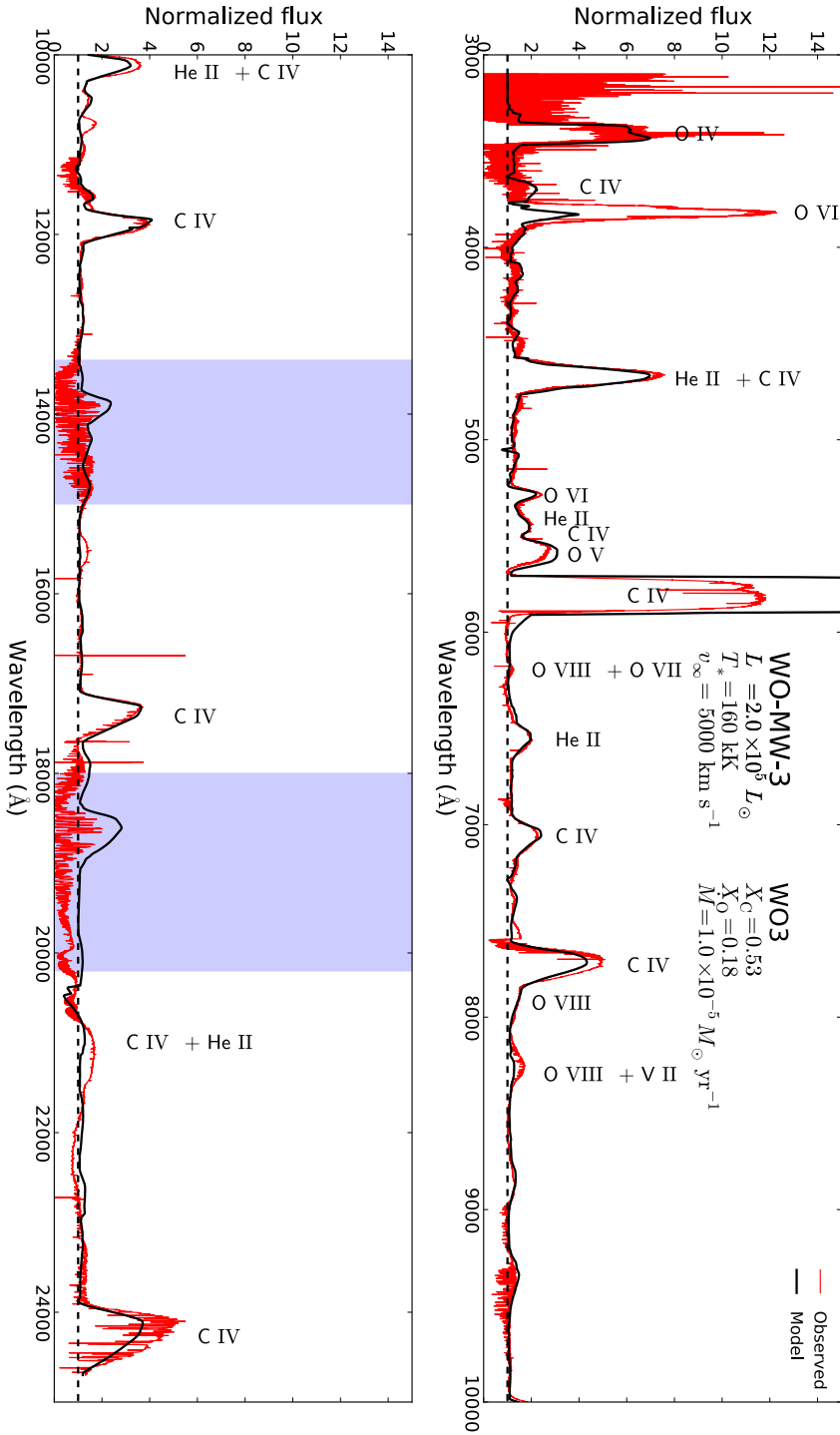


Figure B.5: Best model of WO-MW-3.

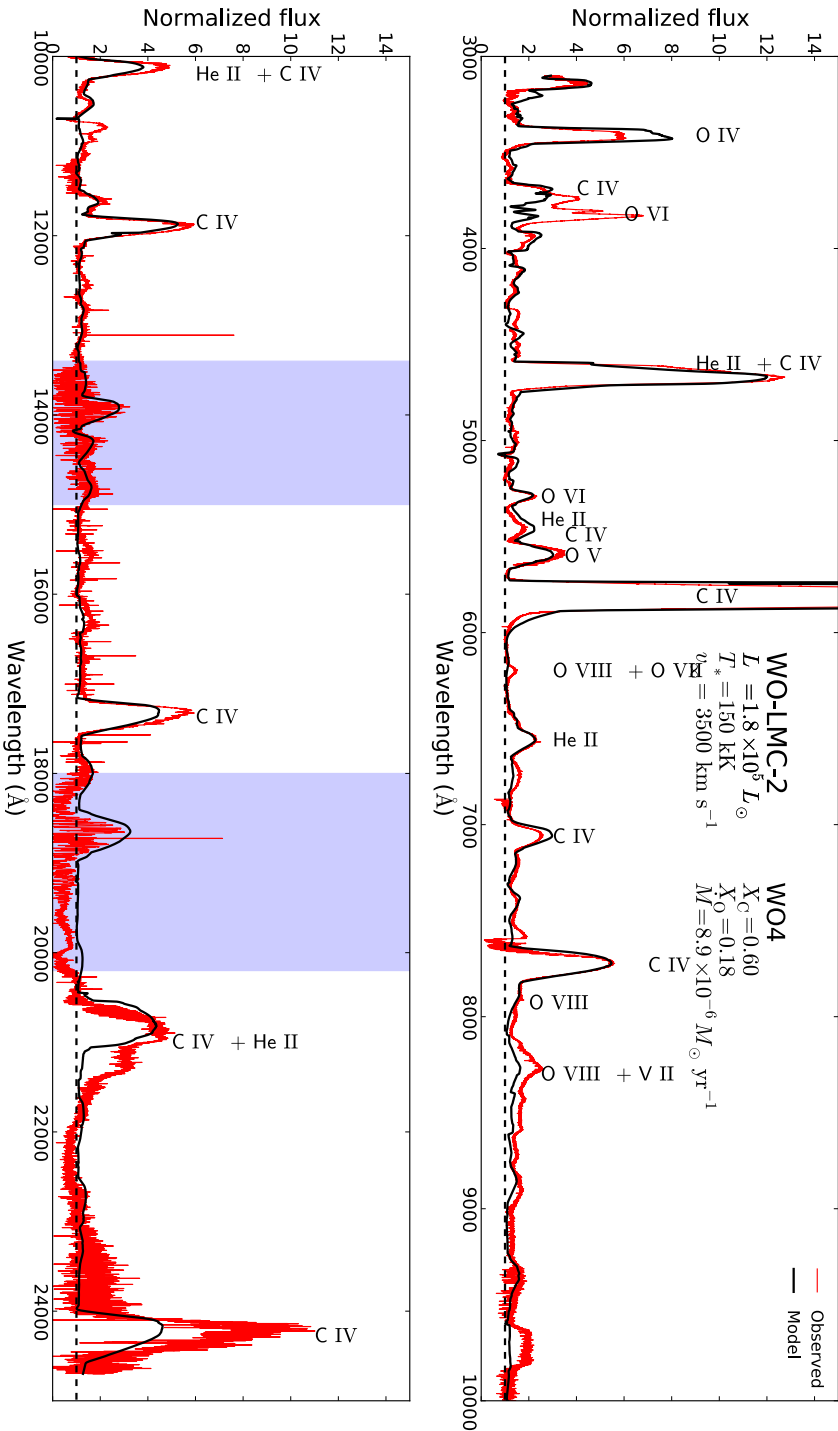


Figure B.7: Best model of WO-LMC-2.

B.3 Overview of used model atoms

This table gives the model atoms used in the CMFGEN analysis.

Table B.1: Overview of the model atoms used.

Species	N_i	N_s	N_t	Species	N_i	N_s	N_t
He I	27	27	27	Ar VI	0	21	81
He II	13	13	30	Ar VII	0	30	72
C II	22	22	22	Ar VIII	0	28	52
C III	44	100	243	Ca III	0	33	110
C IV	59	59	64	Ca III	0	33	110
O II	3	3	3	Ca IV	0	34	193
O III	79	79	115	Ca V	0	45	121
O IV	53	53	72	Ca VI	0	47	108
O V	75	75	152	Ca VII	0	48	288
O VI	25	25	31	Ca VIII	0	45	296
Ne II	0	42	242	Ca IX	0	39	162
Ne III	10	40	182	Ca X	27	27	59
Ne IV	10	45	355	Cr IV	0	29	234
Ne V	10	37	166	Cr V	0	30	223
Ne VI	10	36	202	Cr VI	0	30	215
Ne VII	10	38	182	Mn IV	0	39	464
Ne VIII	24	24	47	Mn V	0	16	80
Si IV	10	37	48	Mn VI	0	23	181
Si V	10	33	71	Mn VII	0	20	203
Si VI	20	42	132	Fe IV	51	51	294
P IV	0	36	178	Fe V	47	47	191
P V	0	16	62	Fe VI	44	44	433
S III	0	13	28	Fe VII	41	41	252
S IV	0	51	142	Fe VIII	53	53	324
S V	0	31	98	Fe IX	52	52	490
S VI	28	28	58	Fe X	43	43	210
Cl IV	0	40	129	Ni IV	0	36	200
Cl V	0	26	80	Ni V	0	46	183
Cl VI	0	18	44	Ni VI	0	37	314
Cl VII	0	17	28	Ni VII	0	37	308
Ar III	0	32	34	Ni VIII	0	34	325
Ar IV	0	50	382	Ni IX	0	34	363
Ar V	0	64	376				

Notes. N_i is the number of levels that are treated with an accelerated lambda iteration. N_s is the number of superlevels, each of which may consist of a single level or multiple levels. N_t the total number of atomic levels in the model atom.

B.4 Equivalent width measurements

Table B.2: Equivalent width (W_λ) measurements of the lines needed for the spectral classification.

ID	SpT	$W_\lambda(\text{O VI } \lambda 3811-34)$ (\AA)	$W_\lambda(\text{O V } \lambda 5590)$ (\AA)	$W_\lambda(\text{C IV } \lambda 5801-12)$ (\AA)
WO-MW-1	WO2	1415 ± 28	196 ± 4	156 ± 1
WO-MW-2	WO2	1087 ± 17	199 ± 2	303 ± 2
WO-MW-3	WO3	475 ± 5	230 ± 4	1627 ± 7
WO-LMC-1	WO3	235 ± 4	104 ± 1	2115 ± 38
WO-LMC-2	WO4	171 ± 4	172 ± 2	1869 ± 28
WO-IC1613-1	WO3	146 ± 28	125 ± 5	417 ± 11

B.5 Helium-burning models

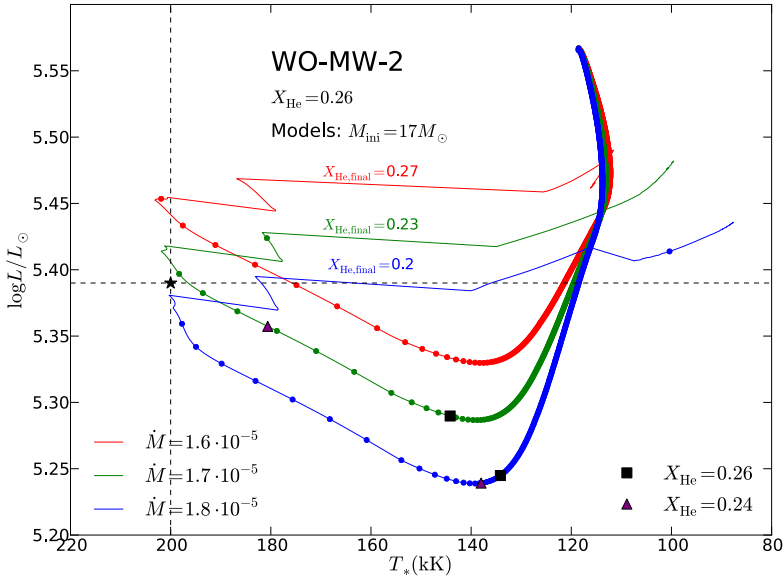


Figure B.8: Same as Figure 5.11, but for WO-MW-2.

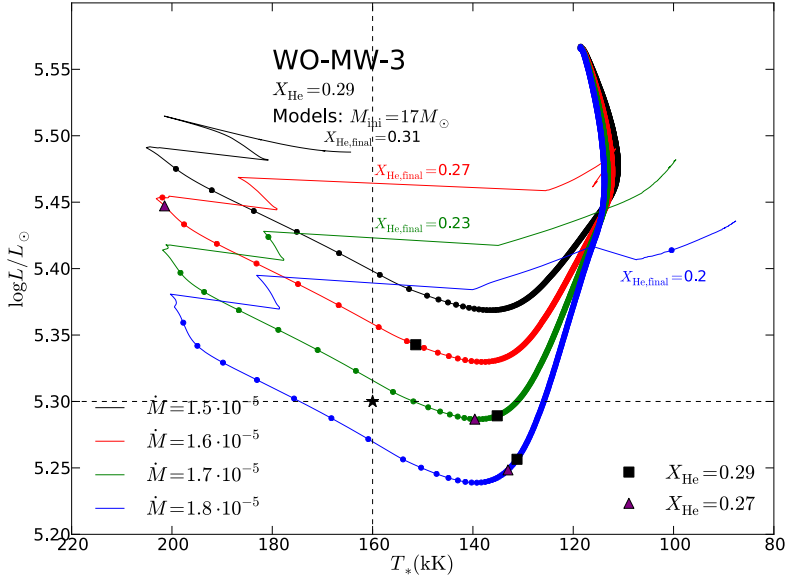


Figure B.9: Same as Figure 5.11, but for WO-MW-3.

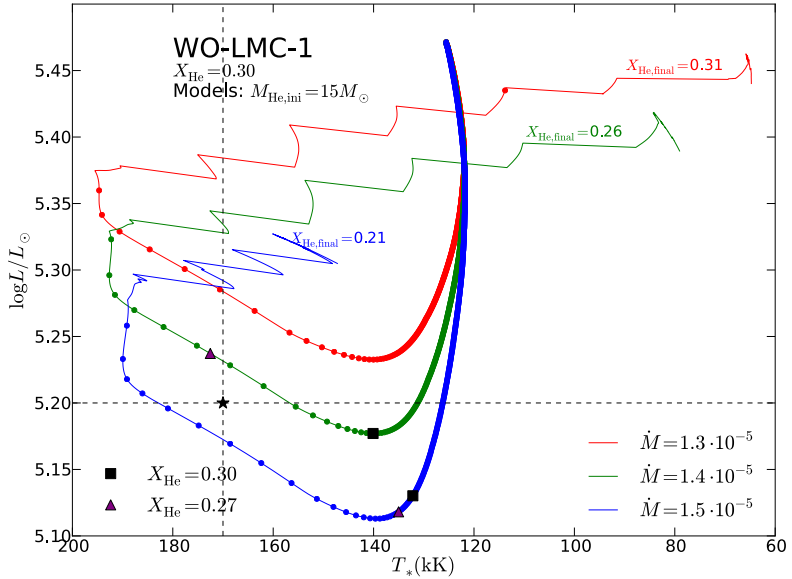


Figure B.10: Same as Figure 5.11, but for WO-LMC-1.

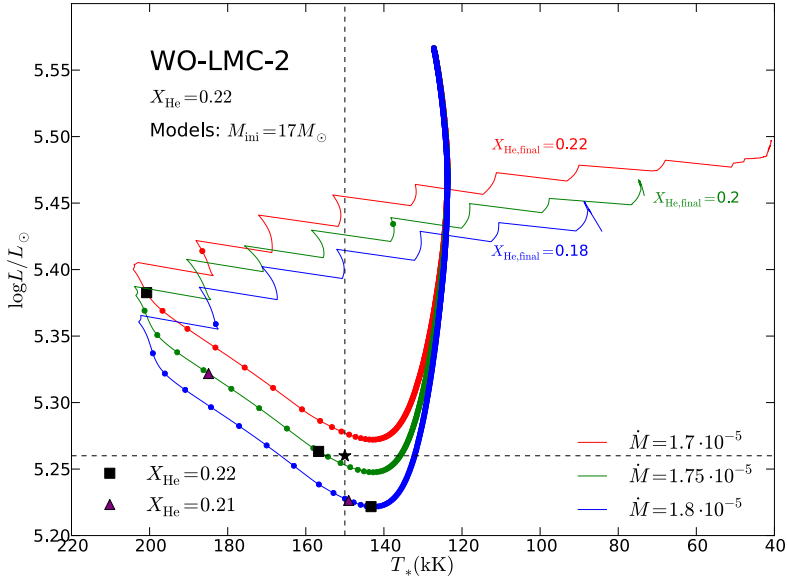


Figure B.11: Same as Figure 5.11, but for WO-LMC-2.

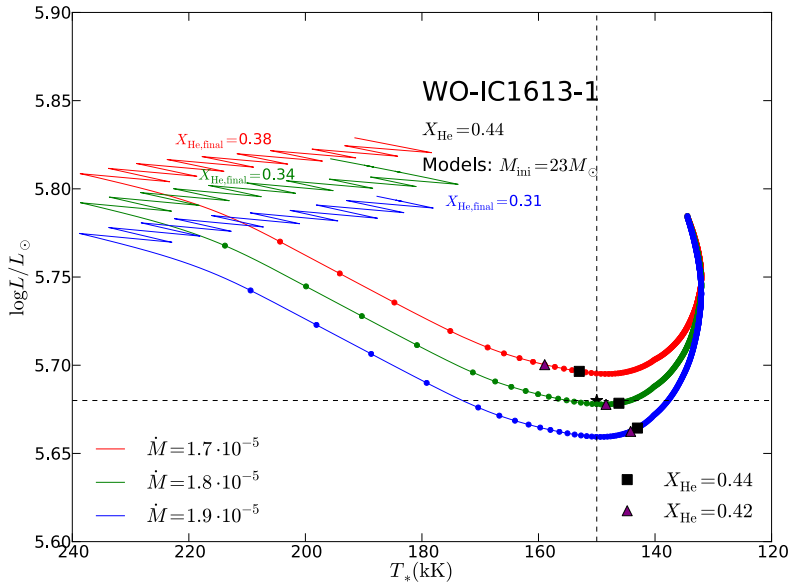


Figure B.12: Same as Figure 5.11, but for WO-IC1613-1.

First-author articles

1. **Tramper, F.**, Sana, H., de Koter, A., Kaper, L., Ramírez-Agudelo, O.H., *A&A, in press (Chapter 3)*
The properties of ten O-type stars in the low-metallicity galaxies IC 1613, WLM, and NGC 3109
2. **Tramper, F.**, Gräfener, G., Hartoog, O.E., Sana, H., de Koter, A., Vink, J.S., Ellerbroek, L.E., Langer, N., Garcia, M., Kaper, L., de Mink, S.E., 2013, *A&A*, 559, 72 (**Chapter 4**)
On the nature of WO stars: a quantitative analysis of the WO3 star DR1 in IC 1613
3. **Tramper, F.**, Sana, H., de Koter, A., Kaper, L., 2011, *ApJL*, 741, L8 (**Chapter 2**)
On the mass-loss rate of massive stars in the low-metallicity galaxies IC 1613, WLM and NGC 3109

Co-authored articles

1. Ellerbroek, L. E., Benisty, M., Kraus, S., Perraut, K., Kluska, J., le Bouquin, J. B., Borges Fernandes, M., Domiciano de Souza, A., Maaskant, K. M., Kaper, L., **Tramper, F.**, Mourard, D., Tallon-Bosc, I., ten Brummelaar, T., Sitko, M. L., Lynch, D. K., Russell, R. W., *A&A, in press*
A resolved, au-scale gas disk around the B[e] star HD 50138
2. Ellerbroek, L.E., Bik, A., Kaper, L., Maaskant, K.M., Paalvast, M., **Tramper, F.**, Sana, H., Water, L.F.B.M., Balog, Z., 2013, *A&A*, 558, 102
RCW36: characterizing the outcome of massive star formation
3. Sana, H., van Boeckel, T., **Tramper, F.**, Ellerbroek, L.E., de Koter, A., Kaper, L., Moffat, A.F.J., Schnurr, O., Schneider, F.R.N., Gies, D.R., 2013, *MNRAS*, 432, L26
R144 revealed as a double-lined spectroscopic binary

4. Nowak, M.A., Hanke, M., Trowbridge, S.N., Markoff, S.B., Wilms, J., Pottschmidt, K., Coppi, P., Maitra, D., Davis, J.E., **Tramper, F.**, 2011, *ApJ*, 728, 13
Corona, Jet, and Relativistic Line Models for Suzaku/RXTE/Chandra-HETG Observations of the Cygnus X-1 Hard State

Conference proceedings

1. Ramírez-Agudelo, O. H., Sana, H.; de Koter, A., Simón-Díaz, S., de Mink, S. E., **Tramper, F.**, Dufton, P. L., Evans, C. J., Gräfener, G., Herrero, A., Langer, N., Lennon, D. J., Maíz Apellániz, J., Markova, N., Najarro, F., Puls, J., Taylor, W. D., Vink, J. S., IAUS 307, New windows on massive stars: asteroseismology, interferometry, and spectropolarimetry, arXiv: 1409.1822
Rotational velocities of single and binary O-type stars in the Tarantula Nebula
2. **Tramper, F.**, Straal, S. M., Gräfener, G., Kaper, L., de Koter, A., Langer, N., Sana, H., Vink, J. S., IAUS 307, New windows on massive stars: asteroseismology, interferometry, and spectropolarimetry, arXiv:1407.5897
The properties of single WO stars
3. **Tramper, F.**, 2013, Massive stars: from α to Ω , arXiv:1312.1555
The nature of WO stars: VLT/X-Shooter spectroscopy of DRI
4. Vink, J.S., Heger, A., Krumholz, M.R., Puls, J., Banerjee, S., Castro, N., Chen, K.-J., Chene, A.-N., Crowther, P.A., Daminelli, A., Gräfener, G., Groh, J. H., Hamann, W.-R., Heap, S., Herrero, A., Kaper, L., Najarro, F., Oskinova, L.M., Roman-Lopes, A., Rosen, A., Sander, A., Shirazi, M., Sugawara, Y., **Tramper, F.**, Vanbeveren, D., Voss, R., Wofford, A., Zhang, Y., 2013, IAU General Assembly Joint Discussion 2, arXiv:1302.2021
Very massive stars (VMS) in the local universe
5. **Tramper, F.**, Sana, H., de Koter, A., Kaper, L., 2012, a Scientific Meeting in Honor of Anthony F. J. Moffat, ASPC, 45, 176
The mass-loss rate of massive stars in low-metallicity galaxies IC 1613, WLM, and NGC 3109

Below is an overview of the acronyms that are used in this thesis.

AT	<i>Auxiliary Telescope</i>
BSG	<i>Blue Supergiant</i>
ESO	<i>European Southern Observatory</i>
EW	<i>Equivalent Width</i>
FWHM	<i>Full-Width at Half-Maximum</i>
GA	<i>Genetic Algorithm</i>
GRB	<i>Gamma-Ray Burst</i>
GTO	<i>Guaranteed Time Observations</i>
HRD	<i>Hertzsprung-Russell Diagram</i>
HST	<i>Hubble Space Telescope</i>
INT	<i>Isaac Newton Telescope</i>
LBV	<i>Luminous Blue Variable</i>
LMC	<i>Large Magellanic Cloud</i>
(N)LTE	<i>(Non-)Local Thermodynamic Equilibrium</i>
MW	<i>Milky Way</i>
PSF	<i>Point-Spread Function</i>
RSG	<i>Red Supergiant</i>
RV	<i>Radial Velocity</i>
SMC	<i>Small Magellanic Cloud</i>
SN	<i>Supernova</i>
S/R	<i>Signal-to-Noise Ratio</i>
UT	<i>Unit Telescope</i>
VLT	<i>Very Large Telescope</i>
WC	<i>Carbon Sequence Wolf-Rayet</i>
WLD	<i>Wind Momentum versus Luminosity Diagram</i>
WN	<i>Nitrogen Sequence Wolf-Rayet</i>
WO	<i>Oxygen Sequence Wolf-Rayet</i>
WR	<i>Wolf-Rayet</i>
(He-)ZAMS	<i>(Helium) Zero-Age Main Sequence</i>

This thesis presents a study of massive stars in two distinct stages of their lives. The first part of the thesis focusses on main-sequence O-type stars in three low-metallicity dwarf galaxies in the Local Group: IC 1613, WLM, and NGC 3109. The properties of these stars give insight in the evolution of massive stars in the young Universe, when the average metal content was low compared to the current value. In the second part of the thesis the focus shifts to the end stages of massive star evolution. Here, the enigmatic oxygen Wolf-Rayet (WO) stars are studied, presenting the most detailed analysis of this type of stars to date.

Low-metallicity O-type stars

The first part of this thesis investigates the mass-loss properties of O-type stars located in the three galaxies mentioned above. As the evolution of massive stars is greatly influenced by the amount of mass they lose throughout their lives, understanding the mechanism that removes this mass is of paramount importance. The standard theory assumes that the outflow is driven by radiation pressure on electron transitions of metallic ions in the atmosphere of the stars, and as such the wind strength is expected to be metallicity dependent. This metallicity dependence has been empirically observed in stars in the Milky Way and the Magellanic Clouds, spanning a metallicity range from solar to about 20% solar. However, it has so far not been explored for stars located in environments with an even lower metal content.

Chapter 2 presents the first quantitative analysis of O-type stars beyond the Magellanic Clouds. The metallicity of the young stellar population in the host galaxies is estimated to be about 15-20% solar, and thus similar to, or just below that of, the metal content of the Small Magellanic Cloud (SMC). The six stars that are studied have been observed with the X-Shooter spectrograph on the Very Large Telescope (VLT). The intermediate resolving power of X-Shooter allows for a good nebular subtraction, and a detailed quantitative spectroscopic analysis. A genetic algorithm (GA) fitting routine is employed to fit synthetic line profiles generated by *FASTWIND* to the observed spectral lines. This results in a good determination of the key stellar and outflow parameters.

These parameters are then used to investigate the outflow properties of the target stars by means of the modified wind momentum versus luminosity diagram. Surpris-

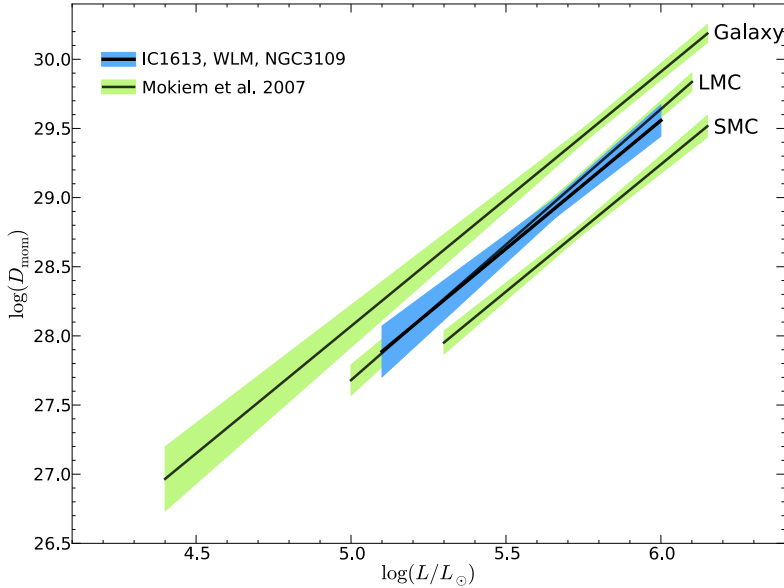


Figure A: Low-metallicity wind strengths in the modified wind momentum versus luminosity diagram. Also indicated are the empirical results from Mokiem et al. (2007) for the Galaxy and the Magellanic Clouds. The wind strengths found in the low-metallicity galaxies are comparable to those found for LMC stars.

ingly, the stars exhibit fairly strong winds, which are reminiscent of a Large Magellanic Cloud (LMC) metallicity instead of a (sub-)SMC one. However, the sample size is too small, and the error bars on the measurements too large, to draw firm conclusions on the origin of the discrepant wind strengths.

In Chapter 3 this problem is further explored. Four more stars in the host galaxies have been observed with X-Shooter. Also, various improvements to the fitting method have been made, resulting in better constraints on the parameters. The full sample, including the six stars from Chapter 2, has been analysed in this way and the modified wind momentum versus luminosity diagram is reevaluated. Including the new stars in the sample, the discrepancy with radiation-driven wind theory is even more pronounced, and a fit to the modified wind momentum shows that their wind strengths are indeed LMC-like (Figure A). Observations in the ultraviolet are needed to further investigate the wind strengths of the target stars.

Chapter 3 also investigates the other stellar parameters of the ten sample stars. A spectral-type versus effective temperature calibration is presented and compared to the relation found for the SMC. There is no significant difference between the two calibrations, which is compatible with the host galaxies having an SMC-like metallicity. The stellar parameters are compared to evolutionary tracks by employing

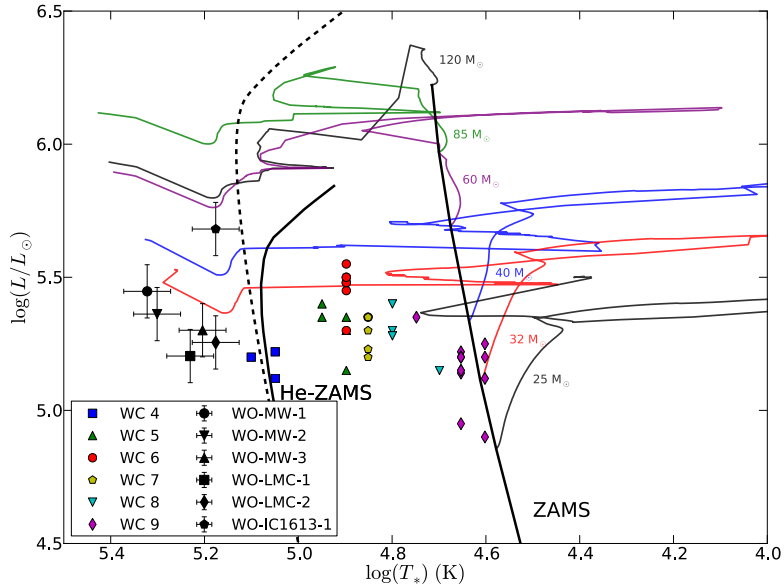


Figure B: Location of the single WO stars in the Hertzsprung-Russell diagram. Also indicated are the WC stars analyzed by Sander et al. (2012) and evolutionary tracks for solar metallicity and an initial rotational velocity of 40% critical from Ekström et al. (2012). The helium zero-age main sequence (He-ZAMS) is indicated for solar metallicity (solid line) and SMC metallicity (dashed line).

the BONNSAI tool, which results in estimates of their masses and ages.

The oxygen sequence Wolf-Rayet stars

In the second part of the thesis the enigmatic WO stars are analyzed. The WO class is usually interpreted as a short evolutionary stage after the more common carbon-sequence Wolf-Rayet (WC) phase, although an alternative option is that these stars originate from higher mass progenitors. In Chapter 4 the WO star DR1 in the galaxy IC 1613 is analyzed. Again, the observations have been obtained using X-Shooter, providing a wavelength coverage from the atmospheric cut-off in the near-ultraviolet up to the near-infrared (2.5 micron). The spectrum of DR1 is analyzed using the state-of-the-art model atmosphere code CMFGEN. As these stars are in a part of parameter space that is hardly explored with models, the methods and diagnostics used to determine the key stellar parameters are described in detail in this chapter.

The analysis of DR1 results in exceptional stellar parameters. With a temperature of 150 kK, the star is extremely hot, and located close to the helium main sequence in the HRD. However, the surface abundances of helium, carbon and oxygen of DR1 are

comparable with those found in WC stars. It therefore seems that DR1 is a descendant of a higher mass progenitor, which results in the high stellar temperature. However, metallicity effects can also play a role, and from the analysis of DR1 alone we cannot conclude on the nature of WO stars as a group.

The final chapter of this thesis further studies the WO stars by analyzing all the single WO stars that were known up to May 2014. All WO stars are exceptionally hot, with temperature ranging from 150-210 kK. More importantly, all stars have low surface helium abundances, with mass fractions typically between 20-30%, but that reach as low as 14% in one star. Their position in the HRD on the hot side of the helium terminal-age main sequence (Figure B) suggests that they are post-core helium burning.

To definitively conclude on the nature of WO stars, we model their properties using dedicated evolutionary tracks for (post-)helium burning stars. These models can reproduce the observed temperature, luminosity and surface helium abundance of all single WO stars. The models indicate that the WO stars are post-helium burning objects, with initial masses of $\approx 40 - 60M_{\odot}$. They are very close to the end of their lives, and will explode in less than 10 000 years, most likely as a type Ic supernova.

Dit proefschrift behandelt de studie van zware sterren in twee verschillende fasen van hun leven. In het eerste gedeelte van de thesis ligt de nadruk op hoofdreeks O-type sterren die zich in drie verschillende dwergmelkwegstelsels in de Lokale Groep bevinden: IC 1613, WLM and NGC 3109. De eigenschappen van deze sterren lijken op die van zware sterren in het jonge heelal, toen het gemiddelde metaalgehalte (metaliciteit) veel lager was dan nu. In het tweede deel van de thesis verschuift de focus naar het eindstadium van de evolutie van zware sterren. In dit deel worden de mysterieuze zuurstof Wolf-Rayet (WO) sterren bestudeerd, in de tot nu toe meest gedetailleerde analyse.

O-type sterren met een laag metaalgehalte

Het eerste deel van de thesis onderzoekt het massaverlies van zware sterren in de drie bovengenoemde melkwegstelsels. De evolutie van zware sterren wordt sterk beïnvloed door de hoeveelheid massa die zij gedurende hun leven verliezen. Het is daarom zeer belangrijk om het mechanisme waarmee deze massa wordt verwijderd te doorgronden. De huidige theorie voorspelt dat dit gebeurt door de stralingsdruk op electronovergangen in metaalachtige ionen in de steratmosfeer. Het wordt daarom verwacht dat de sterkte van de resulterende sterwind afhankelijk is van de metalliciteit. Deze afhankelijkheid is empirisch aangetoond voor sterren in de Melkweg en de Magellaanse Wolken, met andere woorden voor metaalgehalten die variëren van solair tot ongeveer 20% van solair. Voor lagere metaalgehalten is de relatie tot nu toe niet onderzocht.

In Hoofdstuk 2 wordt de eerste kwantitatieve analyse behandeld van O-type sterren die zich in melkwegstelsels verder dan de Magellaanse Wolken bevinden. Deze melkwegstelsels hebben een metalliciteit van ongeveer 15-20% van solair, ongeveer gelijk aan, of iets lager dan, die van de Kleine Magellaanse Wolk. De zes sterren die in Hoofdstuk 2 bestudeerd worden zijn waargenomen met de X-Shooter spectrograaf op de Very Large Telescope. De spectrale resolutie van X-Shooter is hoog genoeg voor een goede correctie voor nevelmissie en maakt een gedetailleerde spectroscopische analyse mogelijk. Om de spectra te onderzoeken wordt gebruik gemaakt van een genetisch algoritme dat synthetische lijnprofielen fit aan de geobserveerde spectraallijnen. Hiermee kunnen de eigenschappen van de ster en sterwind nauwkeurig

bepaald worden.

Deze eigenschappen worden vervolgens gebruikt om de sterwind verder te onderzoeken. Hiervoor wordt gebruik gemaakt van het *modified wind momentum versus luminosity diagram*, waarin een maat voor de impuls van de sterwind uitgezet wordt tegen de lichtkracht van de ster. Hieruit volgt dat de sterren verrassend veel massa verliezen, met een windsterkte die meer lijkt op wat verwacht wordt voor sterren in de Grote Magellaanse Wolk in plaats van de lagere metalliciteit van de Kleine Magellaanse Wolk (of lager). Er zijn echter niet genoeg sterren waargenomen om tot een sterke conclusie te komen over de oorzaak van dit onverwachte resultaat.

In Hoofdstuk 3 wordt het probleem van de sterke sterwinden verder onderzocht. Er zijn nog vier sterren waargenomen met X-Shooter, en er zijn een aantal verbeteringen aangebracht in de fitmethode. Hierdoor kunnen de eigenschappen van de sterren en hun wind nog nauwkeuriger bepaald worden. Het volledige sample, dus inclusief de sterren die in Hoofdstuk 2 zijn geanalyseerd, zijn met deze verbeterde methode onderzocht. Het nieuwe modified wind momentum versus luminosity diagram laat zien dat de sterren inderdaad een windsterkte hebben die hoort bij de metalliciteit van de Grote Magellaanse Wolk. Nieuwe waarnemingen, met name in het ultraviolet, zijn nodig om deze sterwinden verder te onderzoeken.

Naast de sterwinden worden in Hoofdstuk 3 ook de overige eigenschappen van deze sterren onderzocht. De spectraaltype tegen effectieve temperatuur calibratie is gepresenteerd en vergeleken met wat gevonden wordt voor de Kleine Magellaanse Wolk. Er is geen significant verschil tussen de twee calibraties, wat in lijn is met de verwachting als de metaalgehalten van de verschillende melkwegstelsels ongeveer gelijk zijn. Verder worden de stereigenschappen vergeleken met evolutionaire modellen met behulp van BONNSAI. Hiermee wordt een schatting gemaakt van de massa en de leeftijd van de sterren.

De zuurstof Wolf-Rayet sterren

In het tweede gedeelte van de thesis worden de mysterieuze WO sterren geanalyseerd. De groep van WO sterren wordt gebruikelijk gezien als een korte evolutionaire fase na de meer voorkomende koolstof Wolf-Rayet (WC) fase. Een alternatieve verklaring voor het WO fenomeen is dat deze sterren van hogere massa sterren afkomen. In Hoofdstuk 4 wordt de WO ster DR1 geanalyseerd, die zich bevindt in het dwergmelkwegstelsel IC 1613. De observaties zijn wederom gedaan met X-Shooter, die een golflengtebereik heeft van het nabije ultraviolet tot en met het nabije infrarood. Het spectrum van DR1 is geanalyseerd met de geavanceerde modelatmosfeercode CMFGEN. Omdat de eigenschappen van WO sterren in een nauwelijks onderzocht gedeelte van de parameterruimte liggen, worden de methodes en diagnostische lijnen

die gebruikt worden in detail beschreven.

Uit de analyse blijkt dat DR1 extreme eigenschappen heeft: met name de temperatuur van 150 kK is zeer hoog. De temperatuur van DR1 bevindt zich dicht bij het de te verwachten temperatuur die sterren hebben aan het eind van de helium hoofdreeks in het Hertzsprung-Russell diagram. De abundanties van helium, koolstof en zuurstof aan het steroppervlak lijken daarentegen erg op de waarden die gevonden worden voor WC sterren. Het lijkt er daarom op dat DR1 afstamt van een zwaardere ster dan de voorgangers van WC sterren, wat dan de oorzaak zou zijn voor de hoge temperatuur. De metalliciteit kan echter ook een rol spelen, en uit de analyse van DR1 op zichzelf kunnen nog geen conclusies getrokken worden over de aard van de WO sterren.

In het laatste hoofdstuk van deze thesis worden alle andere enkelvoudige WO sterren onderzocht die tot mei 2014 bekend waren. Het blijkt dat alle sterren extreem heet zijn, met temperaturen variërend van 150 kK tot 210 kK. Alle sterren hebben een lage heliumabundantie, met massafracties aan het oppervlak die voor het grootste gedeelte tussen 20 en 30% liggen, en voor één ster zelfs de extreem lage waarde van 14% bereikt. De positie in het Hertzsprung-Russell diagram wijst erop dat deze sterren waarschijnlijk in een post-helium fusie fase zijn.

Om tot een definitieve conclusie te komen over de aard van de WO sterren gebruiken we evolutionaire modellen voor (post-)heliumfusie sterren om de eigenschappen van deze sterren te modelleren. Deze modellen kunnen de waargenomen temperatuur, lichtkracht, en helium abundantie van alle enkelvoudige WO sterren reproduceren. Uit de modellen volgt dat de sterren inderdaad in een post-helium fusie fase zijn, en afstammen van sterren met een initiële massa van $\approx 40 - 60 M_{\odot}$. De sterren zijn bijna aan het eind van hun leven, en zullen in minder dan 10 000 jaar ontploffen als een type Ic supernova.

Acknowledgements

This thesis would not have been possible without the help and support from my supervisors. Alex, it has been a pleasure working with you the past four years. I am very glad with the space I got to define part of my research. Your critical comments and discussions have ensured that I always could get the most out of the results, and I'm sure it will continue to do so in the time to come.

Hugues, you thought me almost all the skills I have obtained during the last four years, from the observations in Chile to working with the GA and FASTWIND. No matter how busy you are, you're always ready to help, which is very much appreciated. I'm looking forward to continue working with you after my PhD.

Finally Lex, we did not work that much together but this thesis would not have been possible without all the observing time you let me have. Thanks for all your input and your enthusiasm, and of course the social group meetings at your place!

Of course, I've had the support of many people besides my supervisors. Those who know me know that I'm not one for writing this down, but that does not make my appreciation any less. Thanks everyone who helped, either with the work or the equally important diversion.